

AN IMPLICIT FINITE DIFFERENCE SOLUTION
TO THE VISCOUS RADIATING SHOCK LAYER
WITH STRONG BLOWING

by

LLOYD BERNARD GARRETT

A thesis submitted to the Graduate Faculty of
North Carolina State University at Raleigh
in partial fulfillment of the
requirements for the Degree of
Doctor of Philosophy

DEPARTMENT OF MECHANICAL AND AEROSPACE ENGINEERING

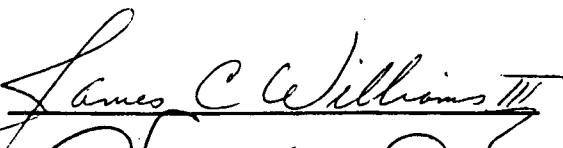
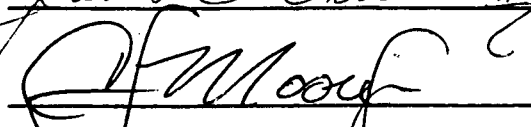

(N (NASA-TM-X-67584) AN IMPLICIT FINITE
LI DIFFERENCE SOLUTION TO THE VISCOUS
RA RADIATING SHOCK LAYER WITH STRONG BLOWING
Ph Ph.D. Thesis L.B. Garrett (NASA) 1971
(NA) CSC 178 p (CATEGORY) 1971

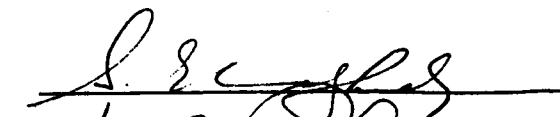

N72-15266

Unclas

CSCL 20D G3/12 12692

APPROVED BY:




Adjunct Professor



Chairman of Advisory Committee

ABSTRACT

GARRETT, LLOYD BERNARD. An Implicit Finite Difference Solution to the Viscous Radiating Shock Layer With Strong Blowing. (Under the direction of GEORGE LOUIS SMITH and JOHN NOBLE PERKINS.)

An implicit finite difference scheme is developed for the fully coupled solution of the viscous radiating stagnation line equations, including strong blowing. Solutions are presented for both air injection and carbon phenolic ablation products injection into air at conditions near the peak radiative heating point in an earth entry trajectory from interplanetary return missions. A detailed radiative transport code that accounts for the important radiative exchange processes for gaseous mixtures in local thermodynamic and chemical equilibrium is utilized in the study.

Starting with minimum number of assumptions for the initially unknown parameters and profile distributions, convergent solutions to the full stagnation line equations are rapidly obtained by a method of successive approximations. Damping of selected profiles is required to aid convergence of the massive blowing cases. It is shown that certain finite difference approximations to the governing differential equations stabilize and improve the solutions.

The present study results indicate lower wall radiative heat fluxes for carbon phenolic ablation than predicted by previous investigators.

BIOGRAPHY

Lloyd Bernard Garrett was born in [REDACTED]

[REDACTED] He was educated in the public school system in Danville and graduated from George Washington High School in 1958.

In June 1962 he received the Bachelor of Science degree in Mechanical Engineering from Virginia Polytechnic Institute, Blacksburg, Virginia. After graduating, he accepted a position with the National Aeronautics and Space Administration at the Langley Research Center. As an employee of the NASA he enrolled in the Graduate Study Program, completed his course requirements at V.P.I. in 1964, and received the Master of Science degree in Mechanical Engineering from that institution in June 1968.

He commenced full-time graduate study at North Carolina State University in September 1968. In June 1969 he returned to the Aero-thermochemistry Branch where he commenced the research for his thesis. He is presently employed in the Viking Project Office at the Langley Research Center.

In 1964 he married Miss Judy Earleen Carpenter of Gastonia, North Carolina. They have three children, Lloyd Bernard, Jr., age five; Kendall Lynn, age four; and Kelly Rebecca, age nine months.

ACKNOWLEDGMENTS

The author wishes to express his appreciation to the National Aeronautics and Space Administration for its continued support of this postgraduate study. In particular, thanks are extended to Mr. Dick Cole and his staff for developing, encouraging, and supporting the NASA Graduate Study Program at the Langley Research Center, to Mr. Charles Pruitt and his staff for the timely preparation of the thesis figures, and to Mrs. Edna Davidson and her staff who "rose to the cause" on many occasions in typing the final manuscript whenever the rough handwritten portions became available from this author.

A special thanks to Miss Eleanor Bridgers of the North Carolina State University for efficiently handling course registrations and scheduling meetings for the author.

Special gratitude is extended to the members of the author's Advisory Committee: Dr. Salah E. Elmaghraby, Dr. Clifford J. Moore, Jr., and Dr. James C. Williams, III, and to the Graduate School Representative, Dr. Don L. Ridgeway. He wishes to take this opportunity to express his appreciation to Dr. G. Louis Smith, Adjunct Professor of his Advisory Committee, for his advice and guidance during the course of this investigation, and to Dr. John N. Perkins, Chairman of his Advisory Committee, for his continuing interest, advice, and support during the past 3 years of postgraduate study and research.

This author is indebted to his former supervisors, Mr. H. A. Wilson, Dr. Wayne Erickson, and Messrs. Charles Rumsey, Edward Sullivan, and Gerald Waldberg, for providing much of the management and technical support for the "50^K Flow Field" effort and also for rendering personal

advice during an indecisive period. He appreciates the understanding and encouragement received from his present supervisors, Messrs. John Graham and William Boyer, while the thesis was being drafted.

He is also indebted to the following personnel at the Langley Research Center: Messrs. John T. Suttles and Elden S. Cornette for their assistance and advice on the radiation model, Mr. Richard Turner for his enlightening advice on stability problems, Mrs. Mary Alice Eastwood for many invaluable consultations on computer programming and its attendant problems, and to Dr. Walter Olstad and Messrs. Ralph Falanga and Randy Graves for their helpful suggestions and assistance during this investigation.

To his wife, Judy, and their children, who made many sacrifices during the course of this postgraduate study, the author extends his thanks for their love, inspiration, and encouragement.

TABLE OF CONTENTS

	Page
LIST OF TABLES	vi
LIST OF FIGURES	vii
LIST OF SYMBOLS	xi
INTRODUCTION	1
REVIEW OF LITERATURE	5
Radiation Transport Models	5
Flow Field Analyses With Radiation	10
ANALYSIS	20
Thin Shock Layer Equations	20
Stagnation Streamline Equations	21
Restrictions and Assumptions	23
Transformed Equations	32
Boundary Conditions	34
Numerical Solution	36
Salient Features of the Implicit Finite Difference Algorithm	48
RESULTS AND DISCUSSION	52
Constant Density Solutions	52
Non-Radiating Air Solutions	55
Radiating Air Solutions	61
Stability Study of the Elemental Diffusion and Energy Equations	71
Radiating Flow Field Solutions With Ablation Products	78
Summary of the Wall Radiative Heat Flux Predictions	83
SUMMARY AND CONCLUSIONS	85
LIST OF REFERENCES	154
APPENDIX	159

LIST OF TABLES

	Page
1. Diffusion coefficient molecular constants	87
2. Summary of radiative heat fluxes at the wall	88

LIST OF FIGURES

	Page
1. Diagram of various assumptions for the analysis of radiating shock layers	89
2. Spectral heat flux distribution for air from SPECS radiation code	90
3. Flow field coordinate system	91
4. Flow field coordinate system for the stagnation line in the transformed coordinates	92
5. Nodal spacings for the finite difference solution	93
6. Flow diagram of the overall solution procedure	94
7. Convergence behavior of a typical constant density solution .	95
(a) Continuity	95
(b) X-momentum	96
8. Constant density solutions for inviscid and viscous flows without blowing	97
(a) Tangential velocity gradient distributions	97
(b) Mass flux distributions	98
9. Influence of blowing rate on velocity gradient for the constant density solutions	99
10. Convergence behavior on the variable density solution - equilibrium air without radiation	100
11. Effect of profile damping on the convergence of the variable density solution - equilibrium air without radiation	101
(a) Total enthalpy	101
(b) Density	102
12. Non-radiating air solutions	103
(a) Continuity equation	103
(b) Y-momentum equation	104
(c) X-momentum equation	105

	Page
(d) Energy equation	106
(e) Equation of state	107
13. Comparisons of the non-radiating air solutions where radiation fluxes are and are not significant	108
(a) X-momentum equation	108
(b) Energy equation	109
14. Radiating air solutions	110
(a) Continuity equation	110
(b) Y-momentum equation	111
(c) X-momentum equation	112
(d) Energy equation	113
(e) Equation of state	114
(f) Radiative heat flux	115
15. Comparison of the enthalpy profile along the stagnation line with solutions from complete subsonic flow field calcula- tions - radiating air (RATRAP code) without blowing	116
16. Comparisons of radiating air solutions including air to air injection with existing stagnation line solutions	117
(a) Tangential velocity gradient	117
(b) Total enthalpy	118
(c) Temperature	119
(d) Radiative heat flux	120
17. Detailed comparisons near the wall of existing radiating air solutions with air to air injection	121
(a) Tangential velocity gradient	121
(b) Temperature	122

	Page
18. Effect of pressure gradient on the tangential velocity gradient solution	123
19. Effect of the constant density viscosity product assumption on the solution	124
(a) Tangential velocity gradient	124
(b) Total enthalpy	125
20. Study of the sensitivity of the radiative heat flux to the density as the solution converges - equilibrium air with radiation	126
(a) Density behavior	126
(b) Radiative heat flux behavior	127
21. Solution to the central difference form of the elemental diffusion equation for a constant density flow	128
(a) $D_{12} = 10^{-6}$	128
(b) $D_{12} = 1.25 \times 10^{-4}$	129
22. Stability of the elemental diffusion equation for central and windward difference approximations	130
23. Comparison of the solutions of the elemental diffusion equation with central and windward difference in a region where the equations are stable	131
24. Effect of windward differencing the energy equation on the non-radiating air solution with massive blowing, (ρv) _w = -0.2	132
(a) X-momentum equation	132
(b) Energy equation	133
25. Comparison of ablator mass fraction profiles assuming binary carbon-nitrogen diffusion and hydrogen-nitrogen diffusion	134
26. Effect of the binary carbon-nitrogen and binary hydrogen- nitrogen diffusion models on the radiative heat fluxes. .	135

	Page
27. Radiating shock layer solutions with ablation products . . .	136
(a) Continuity equation	136
(b) Y-momentum equation	137
(c) X-momentum equation	138
(d) Energy equation	139
(e) Elemental diffusion equation	140
(f) Equation of state	141
(g) Radiative heat flux	142
28. Comparison of stagnation line results for carbon phenolic injection at $(\rho v)_w = -0.076$	143
(a) Enthalpy	143
(b) Temperature	144
(c) Ablator mass fraction	145
(d) Mole fractions	146
(e) Radiative heat flux	147
29. Comparison of stagnation line results for carbon phenolic injection at $(\rho v)_w = -0.2$	148
(a) Mass flux	148
(b) Velocity gradient	149
(c) Temperature	150
(d) Ablator mass fraction	151
(e) Radiative heat flux	152
30. Summary of wall radiative heat flux predictions for air and for ablation product injection	153

LIST OF SYMBOLS

a	tangential velocity gradient
A_n	coefficient of the $n - 1$ unknown quantity for the n th governing equation (see, <u>e.g.</u> , eqs. (56b) and (57))
B_n	coefficient of the n th unknown quantity for the n th governing equation (see, <u>e.g.</u> , eqs. (56b) and (57))
B_ν	Planck function defined by equation (A-4), $\frac{\text{watts-sec}}{\text{cm}^2\text{-sr}}$
c	arbitrary function (see eq. (46))
c_p	specific heat
C_n	coefficient of the $n+1$ th unknown quantity for the n th governing equation (see, <u>e.g.</u> , eqs. (56b) and (57))
D_n	known function appearing on the right-hand side of the n th governing equation (see, <u>e.g.</u> , eqs. (56b) and (57))
\bar{D}_n	modified known function appearing on the right-hand side of the n th governing x-momentum equation (see eq. (64))
D_{ij}	binary diffusion coefficient for the i th and j th chemical species
\bar{e}_i	unit vector in the i th direction
E_2	exponential integral of order 2 (see eq. (A-6))
f	arbitrary function (see eq. (46))
h	static enthalpy
\hbar	Planck's constant, $\hbar = 6.6256 \times 10^{-34}$ J-sec
H	total enthalpy
HDAMP	damping factor for the enthalpy solution
I_ν	specific or monochromatic radiation intensity, $\frac{\text{watts-sec}}{\text{cm}^2\text{-sr}}$
J_i	mass diffusion flux of the i th chemical specie

k	thermal conductivity
k'	Boltzmann constant, $k' = 1.38054 \times 10^{-23} \text{ J/}^{\circ}\text{K}$
K	body curvature, $K = 1/R_b$
M	molecular weight, gm/gm mole
N	total number of nodal points across the shock layer
p	static pressure
Pr	Prandtl number
q	heat flux vector, when primed heat flux is dimensional, watts/cm ²
r	radius measured from axis of symmetry of body (see Fig. 1)
R _b	body radius
Rey	Reynolds number
RODAMP	density damping factor
Sc	Schmidt number
SIGN	parameter dictated by the sign of the convective term $\begin{cases} 0 & \text{if } (\rho v)_n < 0 \\ 1 & \text{if } (\rho v)_n > 0 \end{cases}$
T'	temperature, ^o K
u	tangential velocity component
U	resultant velocity
v	normal velocity component
v _i	diffusion velocity of the ith chemical specie
x	distance measured along the body surface (see Fig. 1)
\bar{X}_i	mole fraction of the ith chemical specie
y	distance measured normal to the body surface (see Fig. 1)
α_i	mass fraction of the ith chemical specie
$\bar{\alpha}_i$	mass fraction of the ith chemical element

$\tilde{\alpha}_F$	mass fraction of the ablation products
α_ν	modified linear absorption coefficient, cm^{-1}
β	pressure gradient term (see eq. (14))
δ	normalizing parameter in the y to η coordination transformation defined by equation (52)
$\Delta\eta$	nodal spacing
ϵ_i/k	molecular constant for the i th chemical specie, $^\circ\text{K}$ (see eq. (29))
ϵ_{ij}/k	molecular constant for the i th and j th chemical species, $^\circ\text{K}$ (see eq. (29))
ϵ_n	error in the i th iteration at the n th nodal point
ζ	dummy variable
η	transformed coordinate defined by equation (34)
θ_b	local body angle
κ	scale factor $= 1 + Ky = 1 + K\delta \int_0^\eta \frac{d\eta}{\rho}$
μ	viscosity (also dummy variable used in equation (A-6))
σ_i'	collision cross section of specie i , \AA^2
σ_{ij}'	mean collision cross section for species i and j , \AA^2
τ	convergence integral
$\dot{\omega}_i$	net volumetric rate of production of specie i
Ω	solid angle, steradians
$\Omega_{ij}^{(1,1)*}$	reduced collision integral used in equation (29)
Subscripts:	
b	refers to the body
c	conduction
D	diffusion

F	foreign or ablation products
inj	refers to injected species (at $\eta = 0$)
n	nth nodal point ($n = 1$ at the body, $\eta = 0$ and $n = N$ at the shock, $\eta = 1$)
R	radiation
s	refers to the shock
w	refers to the wall
∞	refers to free-stream conditions

Superscripts:

i	refers to the ith iteration
---	-----------------------------

Primed quantities are dimensional

INTRODUCTION

A blunt spacecraft entering planetary atmospheres at earth hypersonic speeds encounters intense radiative heating rates, particularly in the frontal or stagnation region. Acceptable interior temperatures are maintained by mass transfer cooling through the use of heat shields constructed of polymeric ablator materials (Walberg and Sullivan). Near peak heating altitudes in many entry trajectories, such as entry into the earth's atmosphere from a direct return manned Mars mission, the mass of gas injected into the flow field is an appreciable fraction of the mass of the oncoming flow (Chin) and is sufficient literally to blow the viscous boundary layer off the surface of the spacecraft.

This condition, which is generally referred to as strong or massive blowing, has a physically destabilizing effect on the flow field that seriously impairs numerical solutions to the governing equations (Libby and Sepri). Libby (1970) describes the physics of the problem to be that of an inner region near the wall which is dominated by pressure and inertia forces where viscous effects are small, and a thin viscous outer region which adjusts to the edge conditions. For small blowing rates the viscous boundary layer is near the wall and the presence of the solid wall has a stabilizing effect on the flow. However, for the massive blowing problem, the gaseous inner layer may not adequately stabilize the flow.

The problem of massive blowing where the outer viscous flow adjusts to the edge conditions has been studied extensively for nonradiating flows (cf., e.g., Kassoy, Libby (1962, 1970), Libby and Sepri, and Kabuta and Fernandez). However, there has been limited attention

directed to the solution when radiation is coupled into the problem. Most previous approaches either required excessive computer time for the numerical solution or were approximate analyses which lead to questionable inputs of the thermodynamic properties required for the radiation computations. Since radiative heat fluxes (in addition to being strong functions of temperature and density) can also be sensitive to the chemical species within the shock layer, some of which are strong radiation emitters and absorbers (Hoshizaki and Lasher), care should be taken in defining these quantities across the entire shock layer. A complete discussion of previous approaches to the viscous radiating shock layer with mass addition is developed in the chapter on Review of the Literature.

The purpose of this investigation is to develop an approach for the numerical solution to the coupled viscous radiating flow field along the stagnation line of a blunt body under both weak and massive blowing conditions. It is required to solve the governing Navier-Stokes equations without making unnecessary simplifying assumptions to the equations and in the numerical solution that could result in inferior inputs for the radiative flux computations. Since the flow equations are coupled, iteration or some multiple pass procedure is required. Thus, the problem becomes one of efficient iteration procedures.

An implicit finite difference method, which has previously been shown to be computationally efficient for chemical nonequilibrium studies without mass addition (Blottner, 1969), is developed for the solution to the proposed problem. The nonlinear governing differential equations are written in finite difference form at all nodal points within the shock layer, with boundary conditions specified at the wall and immediately behind the shock. The formulation results in a tridiagonal matrix system

of algebraic equations which is efficient for machine computation. The governing equations are solved "one at a time" in succession across the entire shock layer. The overall numerical solution technique to the two-point boundary problem is by iteration of the flow variables at each nodal point in the shock layer. Since the governing equations are solved one at a time, rather than concurrently at each nodal point (as in initial value forward integration techniques), then the nodal spacing requirement for the overall solution is not limited by the stability requirement of the most unstable equation.

A section is devoted to the stability of the finite difference solutions to the governing equations. Particular attention is directed to the stability of the species continuity equation with binary diffusion using central differencing and a two-point windward differencing scheme that provides automatic damping of the profiles.

Radiation computations are carried out using an existing radiative transport computer program, RATRAP, developed by Wilson (1967). The program uses the tangent slab approximation (one-dimensional) that accounts for absorption and emission within a layer of arbitrary optical thickness and is for equilibrium gaseous mixtures of hydrogen, carbon, nitrogen, and oxygen. Pressure, enthalpy, and elemental composition profiles are computed by the viscous flow field solution as inputs to the radiation program. Radiation fluxes are evaluated at various nodal points within the shock layer to provide coupling with the flow field. The transport properties for equilibrium air (i.e., viscosity and reactive Prandtl number, see Hansen) are used in the computations to account for the energy transport due to binary diffusion.

Numerical results are presented for both air-to-air injection and for the injection of the ablation products of a carbon phenolic ablator

heat shield into an air stream for a range of blowing rates of interest. Additional computations are presented for constant density flows and for viscous nonradiating flows with air-to-air injection.

The air-to-air injection cases include calculations for a 3.05-meter spherical nose radius body entering the earth's atmosphere at 15.24 kilometers per second velocity at 61 kilometers altitude with a blowing mass rate to free-stream mass flow rate of one-tenth. The results are compared with an initial value forward integration method, integral approaches, and an "exact" numerical solution for identical free-stream and wall boundary conditions. An assessment is made of some approximations contained in these analyses.

REVIEW OF LITERATURE

The scope of the literature survey is restricted primarily to the flow within the shock layer near the stagnation region of a blunt reentry spacecraft. The emphasis is on viscous radiating flows with mass addition which is typical for hypervelocity enters into earth's atmosphere from manned interplanetary missions.

Some of the earliest predictions for the radiative heat flux to a blunt body entering the earth's atmosphere at earth parabolic velocities or greater indicated that the heat flux at the stagnation point was proportional to the velocity raised to the tenth power (Meyerott). In more recent years the predictions of the levels of the radiative fluxes have almost progressively decreased, while the complexity of the computations have systematically increased. An excellent review of the advances in radiating shock layer analyses is given by Anderson in his 1969 paper. Figure 1, which is taken from his paper, is a diagram of the various assumptions used in the analysis of radiating shock layers. The organization of this chapter will follow this diagram, with a section devoted to the radiation transport models and one devoted to coupled and uncoupled flow field analyses including the more recent approaches to the radiation-induced massive blowing problem. Much of the literature review is condensed from Anderson's survey, and interested readers are referred to his paper and his extensive list of references for a more lucid description of contributions to radiation flow field analyses prior to 1969.

Radiation Transport Models

The salient features of radiation models as they are applied for tractable solutions to radiating flow field problems are discussed in

this section. The evolution of the radiation models which are incorporated into high-temperature shock layer analyses is traced.

In general, the radiative energy exchange in a gaseous medium is governed by integral equations which involve temperature, mass density, and the number density of the individual chemical species integrated over both the radiation frequency spectrum and three-dimensional physical space. Hirschfelder, Curtis, and Bird (p. 721) describe the functional dependence of radiation on these properties in the following manner.

In the presence of radiation, a molecule has a certain probability of either absorbing or emitting radiation of a frequency characteristic of some transition from one quantum state to another. Or a molecule in an excited state has a certain probability of spontaneously emitting radiation of a certain frequency. Each substance therefore has an absorption spectrum which can be expressed in terms of the coefficient of absorption which is a function of the frequency. Since the absorption spectrum depends upon the distribution of the molecules in their various quantum states, then the absorption coefficient depends upon the temperature of the substance. The spectral lines for isolated molecules have a natural width (due to spontaneous emission of radiation), and as the molecules are brought together these lines become broader (due to pressure broadening) and become displaced (due to the distortion of the molecules themselves). Thus the coefficient of absorption depends upon the density of the system . . .

Since fluid elements (actually the individual atomic and molecular particles) both emit and absorb radiation, then the radiation exchange for both mechanisms must be considered. At a given point emission is a function primarily of the conditions at the point, whereas absorption is dependent upon not only conditions at the point but also is a function of the thermodynamic properties and the frequency of radiation emission of all the surrounding fluid elements. Radiation at a given frequency travels a "photon or radiation mean free path" before being absorbed, thus absorption of the radiation is dependent upon the physical distance between the

emission source and the absorbing particle. Consequently, radiation exchange within a given volume is a function of three-dimensional physical space.

The problem of the general three-dimensional radiation exchange where there are many different chemical species or particles at various energy levels is indeed formidable, and simplifying assumptions are required in order to obtain tractable solutions to most radiation exchange problems. For stagnation streamline analyses, the enclosure volume is simplified by the "tangent slab approximation," that is, radiation heat fluxes are computed assuming that a one-dimensional planar slab of gas is present within which conditions remain constant except across the slab in the direction normal to the slab. This approach is almost universally applied in radiating shock layer analyses. At the stagnation line the justification for the assumption is that for bodies of large radii surrounded by a relatively thin shock layer, conditions vary slowly in the radial direction, whereas the major gradients are normal to the body. This effect has been investigated by Kennet and Strack, by Koh, and by Hoshizaki and Lasher. The investigations indicate that the error introduced by the approximation should be less than 5 percent.

The tangent slab approximation permits one to evaluate the divergence of the radiative heat flux that appears in the energy equation by evaluation of the gradient of the heat flux in the normal direction only and uncouples the stagnation line solution from the rest of the shock layer as far as radiation is concerned. In the present analysis the tangent slab approximation is used.

For radiation computations the gas is treated either as transparent or self-absorbing. A transparent gas is one which emits radiation but

does not absorb any incident radiation from the surrounding fluid elements. According to Vincenti and Kruger, this approximation is valid only when the gas is optically thin at all wave lengths. An optically thin gas is one in which the characteristic mean free path of a photon is much larger than the thickness of the shock layer. Anderson points out that in practice the transparent gas assumption is reasonable only for reentry conditions where radiation effects first become noticeable, such as 10 km/sec entry velocities. For velocities around 15 km/sec, the transparent assumption can overpredict the radiative flux by factors of 2 or more.

A self-absorbing gas both emits and absorbs radiation; that is, a fluid element locally emits radiative energy as well as absorbs energy from the surrounding fluid elements. The gas is treated either as gray or non-gray. A gray gas includes gray self-absorption which is a function of temperature and pressure, but the absorption coefficient is assumed not to be a function of the wave length or radiation frequency. It was first indicated by Olstad and later demonstrated by Hoshizaki and Wilson (1967) that the non-gray model is by far the more realistic model and is important for most high-velocity entry missions. In this model the absorption coefficient is considered to be a function of wave length as well as temperature and pressure.

An example, given by Anderson, that indicates the reason for including non-gray self-absorption is the phenomenon associated with high-temperature air. Air will absorb radiation in the vacuum ultraviolet (short wave length) region but is relatively transparent in the infrared (long wave length) region. For example, there are five orders of magnitude variation with frequency in the continuum absorption coefficient of air at 14,000° K and one atmosphere pressure. Olstad's

results for the inviscid flow of air and Hosizaki and Wilson's (1967) results for the viscous flow of air showed that substantial reductions in the radiative heat flux to the body were obtained in going from gray to the non-gray self-absorption models.

The non-gray gas model must be applied to obtain realistic estimates for the radiative heat flux to the body and this requires a detailed integration of the absorption coefficient over the frequency spectrum.

For air, significant differences still exist not only in the spectral absorption coefficients for certain chemical species but also in the radiation models that are coded for computer solutions (Suttles, 1971). However, computations dealing strictly with radiative transport in air for typical earth entry conditions are approaching a firm basis and simplified radiation models can be developed for absorption coefficients as functions of wave length, such as Callis' three-step model, to speed up the time-consuming radiative transport computations. When one also considers injection of ablation products into the air stream, radiation transport modeling becomes complicated indeed because of the added dimension due to the presence of foreign radiating chemical species (Anderson). In the interest of quantitative results, it appears better at present to generate spectral absorption coefficients from the spectral details for the individual chemical species than to attempt absorption coefficient modeling on the basis of a specified overall chemical composition.

Existing radiation transport computer programs are available which consider ablation products in addition to air chemical species, such as RATRAP, developed by Hosizaki and Wilson (see Wilson, 1967); SPECS, developed by Thomas; and RADICAL, developed by Nicolet. These programs, which perform radiation computations based on the spectral details of the

individual chemical species, are time consuming for stagnation line analyses. However, usage of these types of programs are required since realistic analyses have indicated that the addition of ablation products to the flow field can reduce the heat fluxes to the body by factors of two below pure air flow (see, for example, Hoshizaki and Lasher, Coleman et al., and Chin). As was the case for air, differences exist in the computer codes due largely to uncertainties in the absorption coefficients and the spectral modeling of certain chemical species. RATRAP, which is used in this analysis, is somewhat time consuming, but it contains the appropriate detail to be compatible with the rigorous flow field competition expected of the present analysis.

It is appropriate at this point to begin the discussion on flow field analyses with radiation. The radiation transport models discussion is terminated upon noting that differences in the heat flux predictions at the body can be a result of not only differences in the radiation transport codes but can also be a result of the inaccuracies in the solutions to the flow equations. In particular, the concentration or number densities of strongly absorbing or emitting ablation chemical species can be strongly affected by computed temperatures and densities within the shock layer.

Flow Field Analyses With Radiation

The appearance of the divergence of the radiative flux as a term in the general energy equation governing the flow of a radiating gas couples the flow field and the radiative transport analysis. For relatively low entry velocities, the radiative heat fluxes are small and consequently do not exert any significant influence on the flow field thermodynamic or flow variables. However, for hyperbolic entry velocities,

typical of manned return missions from Mars, the radiative heat fluxes are large, and thus radiative cooling (energy losses) with the shock layer must be considered. The net effect of radiative cooling is to reduce the radiative heat flux to the body because of a reduction in temperature and a subsequent increase in shock layer density from adiabatic conditions (see, for example, Wick and Hoshizaki and Wilson, 1965). This coupling between radiative transport and gas dynamics for this problem is commonly referred to as the coupled radiating shock layer problem.

Howe and Viegas were the first to investigate the flow of a viscous, radiating, self-absorbing gas in the stagnation region including the effects of mass addition. Since they assumed a gray radiation model, the radiation flux results are not quantitative. However, they showed that similarity considerations could be applied in the stagnation region of the viscous shock layer where radiation is present, thus reducing the governing partial differential equations to ordinary differential equations. Howe and Viegas used a Levy-Lees type of boundary-layer transformation, which involves the integral of the viscosity-density product over physical distance, and similarity considerations to reduce the Navier-Stokes equations to compressible Falkner-Skan boundary-layer equations (see Schlichting, pp. 354) for axisymmetric stagnation region flow. They solved the momentum equation numerically by an initial value forward integration method (Adams-Moulton predictor corrector, see Hildebrand). The energy and species continuity equations were solved by numerical evaluation of the exponential integrals that appear in the exact analytical solutions to the differential equations. The solution to the coupled system of equations was iterated by converging on the

value of the shear stress at the wall. In their fully viscous analysis the mass injection rates were restricted to moderate amounts which did not upset the stability of the boundary layer near the wall. The difficulty with the stronger blowing rates can be traced to numerical instability problems associated with evaluating the exponential integrals in the exact analytical solutions to the governing equation. Wilson (1970), who applied a similar approach as that of Howe and Viegas (with the notable exception being his momentum equation solution), describes the problem for the fully viscous shock layer with massive blowing to be one of numerical precision required to take the differences between the large numbers which appear in the exponential integrals. Further aspects of this problem will be discussed in association with Wilson's 1970 paper and in the Results and Discussion chapter.

In 1965 Hoshizaki and Wilson (1965) developed their integral method for the solution to the coupled viscous radiating shock layer about a blunt body. Fifth and sixth order polynomials were used to express the velocity and total enthalpy profiles, respectively, across the shock layer. In addition to presenting results for the stagnation region, they also presented results around the body using a forward integration technique with a limited number of iterations on the shock shape. The solutions were restricted to no blowing and a transparent radiating gas.

Hoshizaki and Wilson (1967) extended their integral approach to include injection of ablation products into the boundary layer for moderate blowing rates. And, they improved their radiation transport model to include specular (non-gray) self-absorption. In the solution, fifth and second order profiles were assumed for the velocity and elemental mass fraction of the ablation products, respectively. With the specified

velocity and species distribution profiles, they were able to solve the energy equation by using a method similar to that used by Smith and Clutter for boundary layer solutions. In the Smith and Clutter solution, the energy equation is solved across the shock layer by a method of superposition of two independent energy equation solutions. The nonsimilar terms in the energy equations (derivatives in the tangential direction) were included in finite difference form. Hoshizaki and Wilson (1967) assumed a binary diffusion model and assumed that the air and ablation products did not react chemically. Air transport properties were used in the analysis. They observed that, since the entire shock layer was treated as viscous, they did not have to match frequency dependent radiative fluxes at the viscous-inviscid interface.

In 1968 Hoshizaki and Lasher extended the integral approach to the massive blowing problem (up to 10 percent of free-stream mass flow). The integral method was applied to obtain an approximate solution to the momentum equation for a fifth order polynomial representation of the velocity profile. The species continuity and energy equations were solved by means of similarity transformations and numerical integration of the resulting exponential integrals. Their detailed analysis of the spectral absorption coefficients for 20 air and ablation product chemical species showed that the carbon atoms, which diffuse far into the shock layer, act as strong radiation absorbers.

Chin, in 1968, developed a numerical method for solving for the radiation coupled inviscid stagnation flow with mass addition. In this analysis it was assumed that no mixing occurred between the ablation products in the inner inviscid region and the air products in the outer inviscid region which results in a distinct interface (in terms of

chemical species) between the two regions. He integrated the conservation equations for the air layer from the shock wave to the interface and from the body to the interface. He iterated on the wall heat flux, the blowing rate, and the velocity and enthalpy profiles until he converged on the enthalpy distribution and heat flux to the wall. It is interesting to note that the blowing rate is an implicit part of his solution and, for the conditions of interest in this analysis ($U_\infty \sim 15$ km/sec, altitude ~ 65 km), he calculated a blowing rate of 7.6 percent of free-stream mass flow rate. His results were for a spherical body of radius 256 cm, constructed of carbon phenolic ablative material. The solutions to the inviscid governing equations converged very rapidly; however, since the viscous region (which typically occupies about 10 percent of the shock layer for the Reynolds numbers of interest) was neglected, then there was no mechanism provided for the diffusion of the strongly absorbing carbon atoms and ions into the air layer.

The first numerical solution to the exact Navier-Stokes equations for the thin shock layer at the stagnation line, including radiative transport, was presented by Rigdon, Dirling, and Thomas (1968). This analysis included massive blowing (up to 10 percent) for air-to-air injection. In 1969 they extended the solution to massive blowing of ablation products (Rigdon, Dirling, and Thomas, 1970), with blowing rates up to 20 percent. The numerical procedure which they employed is computationally time consuming. They used an initial value forward integration scheme in which they were required to adjust four initial conditions (temperature, tangential velocity gradient, temperature gradient, and the shear), evaluated at the stagnation point. These initial conditions were iterated

until the two boundary conditions for both momentum and energy equations were satisfied at the shock and at the body. In the ablation analysis they were further required to satisfy the binary species continuity equation over the shock layer. If the same initial value forward integration scheme is used, then this requires a guess for the elemental mass fractions of the injected foreign material and its gradient at the stagnation point in order to satisfy the boundary conditions at the shock wave and the body. The net result is the requirement that one guess six coupled initial conditions which are unknown apriori in order to satisfy the boundary conditions.

From the results of their solution to the exact governing equations, Rigdon et al. (1970) were able to make direct comparisons with the integral results of Wilson and Hoshizaki (1969) and concluded that the polynomial approximations which had worked so well for nonblowing were not sufficient to describe the momentum equation solution in the presence of massive blowing. Although differences existed in the radiation models (Rigdon et al. (1970) used the SPECS code (see Thomas), whereas Wilson and Hoshizaki (1969) used an updated version of RATRAP (see Wilson, 1967)), the factors of two to four differences in the ablation layer thicknesses could not be explained on the basis of radiation model differences.

In 1969 Wilson (1970) concluded that the approximate integral solution to the momentum equation was inadequate for large mass injection and/or the Reynolds numbers of interest. As mentioned previously, his treatment of the energy and the species continuity equations was similar to that of Howe and Viegas. He used Dorodnitsyn type of transformations (integral of the density over physical distance) and similarity conditions to obtain exact analytic solutions to the energy and species continuity equations.

He attributes the momentum equation solution (see Wilson, 1969) to a solution technique developed by Chou and Blake for a similar problem. Upon performing an additional coordinate transformation which involves viscosity and assuming that the density viscosity product is a constant across the shock layer, Wilson (1970) developed the second-order differential equation. He subsequently differentiated the equation, which makes it linear (in the second derivative), to obtain an exact analytical solution to the equation in terms of exponential integrals. Rather than solve the momentum equation with an initial value technique as was done by Howe and Viegas, Wilson employed a successive approximation algorithm to all the analytical governing equations. In the successive approximation scheme, which is similar to the technique applied in the present study, the distribution of properties are initially specified across the shock layer and the governing equations are iterated until satisfactory convergence is obtained.

Wilson (1970) observed that with his formulated equations he was unable to obtain a numerical solution to the fully viscous equations for relatively large blowing rates (greater than 5 percent, approximately). As previously mentioned, Wilson traced the problem to one on numerical instability associated with taking the differences between exponentially large numbers (greater than about e^{10}), which were about the same order of magnitude. Since the computer only carries about 8 to 16 significant digits, then the resulting difference between these large numbers becomes meaningless. Apparently, these exponentially large numbers occur in the numerical solution in regions where the viscous effects become small (Wilson observed the effect in the inner region near the wall for large blowing) and part of the problem could be due to the loss in precision

when one uses something like a Simpson's rule (Conte) to numerically integrate under an exponential curve.

Wilson (1970) was able to circumvent the numerical precision problem for massive blowing by solving inviscid equations in the inner region and the fully viscous equations at a somewhat arbitrary distance from the body. The interface criteria was that the power to which e is raised be less than 10.

In 1970, Smith, Suttles, Sullivan, and Graves presented a combined flow field and ablation study of a blunt body entering the earth's atmosphere at interplanetary velocities. The analysis, which was motivated by a study of a flight experiment to examine the radiation and materials response problems at hyperbolic entry velocities, yielded transient ablator mass loss rate histories for a complete entry trajectory. The results indicated that ablation rates from high-density phenolic nylon reached a peak of about $0.055 \text{ g/cm}^2\text{-sec}$ (10 percent of free-stream mass flow rate) at the stagnation point of a 122-cm-diameter ellipsoid body of 4:1 axis ratio. Smith, Suttles et al. examined the entire subsonic flow region surrounding the blunt body by dividing it into three interacting regions: an inviscid outer layer, a boundary layer, and a charring heat shield. The inviscid outer layer flow was determined by a one-strip integral method with radiation developed by Suttles (1969). The inviscid flow field and the ablation solution provided the boundary conditions for the radiating boundary-layer computations. The boundary layer and the ablation calculations were iterated until the heating rates and the ablation rates converged. For the larger blowing rates the numerical method for the solution of the boundary-layer equations was not suitable and they adapted an integral procedure by Libby (1962) for the radiating

boundary-layer solution. The boundary layer and the inviscid outer layer solutions were joined by assuming a cubic variation for the elemental mass fraction distribution within the boundary layer and by adjusting the edge enthalpy condition.

One of the significant conclusions of Smith, Suttles et al. was that the introduction of ablation products into the boundary layer did little to attenuate the radiative flux to the wall. In their analysis they used the RATRAP computer code developed by Wilson (1967), and they compared their results with Chin and with Rigdon et al. (1969), who used different radiative transport computer codes. Whereas Chin's solutions for a 7.6 percent blowing rate and Rigdon et al. (1969) solutions for a 20 percent blowing rate indicated reductions in the wall heat flux of about 45 percent below the nonblowing rates, Smith, Suttles et al. calculated reductions of only about 22 percent. Part of this difference has been traced, particularly in the case of Chin's results to differences in the radiative transport models. However, Wilson and Hoshizaki (1969) in their approximate integral approach were indicating radiative heat flux reductions of 40 percent from nonblowing heat fluxes for 10 percent blowing rates and of 60 percent for 20 percent blowing rates using the RATRAP radiation code. Wilson's more recent results (Wilson, 1970), using his improved momentum equation solution, have indicated much lower heat flux reductions (only 18 percent) at blowing rates of 5 and 10 percent. While there are differences in the free-stream conditions in the Wilson and Hoshizaki (1969) and the Wilson (1970) studies, they do not appear to be sufficient to account for the differences in the radiation blockage effects in the two analyses. Apparently, the answer to these differences must reside in part in the analytical and numerical treatments of the governing flow equations.

One of the questions which the present analysis will attempt to answer is whether the approximate integral treatments of the governing equations and/or "exact" numerical treatments of approximate systems of equations can accurately define the flow properties required for the radiation computations with and without blowing. The numerical technique to be developed for the analysis of the coupled viscous, radiating flow along the stagnation line and including massive blowing is an implicit finite difference scheme. Blottner has shown this approach to be computationally superior to initial value schemes for chemical nonequilibrium stagnation line studies without blowing.

In the implicit method, the problem is treated as a two-point boundary value problem in which boundary conditions are specified at the shock and at the body. The entire shock layer is treated as viscous, which requires no "patching" of two or more solutions. The thin shock layer equations which govern the viscous along the stagnation line (Ho and Probstein) and which are exact through second order are solved at discrete nodal points along the stagnation line by iteration through the application of a method of successive approximations. Singularities do not appear in the formulation since the viscous term takes effect as the convective terms (mass flux) approach zero in the vicinity of the stagnation point.

ANALYSIS

Thin Shock Layer Equations

The governing equations for the steady-state flow of a viscous radiating gas in the stagnation region of a blunt axisymmetric body at moderate-to-high Reynolds numbers are given by Ho and Probstein and Scala. They are:

Continuity:

$$\frac{\partial}{\partial x'}(r'\rho'u') + \frac{\partial}{\partial y'}(\kappa'r'\rho'v') = 0 \quad (1)$$

X-momentum:

$$\rho'u' \frac{\partial u'}{\partial x'} + \kappa'\rho'v' \frac{\partial u'}{\partial y'} + K'\rho'u'v' = - \frac{\partial p'}{\partial x'} + \frac{\partial}{\partial y'}\left(\kappa'\mu' \frac{\partial u'}{\partial y'}\right) \quad (2)$$

Y-momentum:

$$\rho'u' \frac{\partial v'}{\partial x'} + \kappa'\rho'v' \frac{\partial v'}{\partial y'} - K'u'^2 = - \kappa' \frac{\partial p'}{\partial y'} \quad (3)$$

Energy:

$$\begin{aligned} r'\rho'u' \frac{\partial H'}{\partial x'} + \kappa'\rho'v'r' \frac{\partial H'}{\partial y'} = & - \frac{\partial}{\partial y'} \left[\kappa'r'(q'_{C,y} + q'_{D,y} + q'_{R,y}) \right] \\ & + \frac{\partial}{\partial y'} \left(\kappa'r'\mu'u' \frac{\partial u'}{\partial y'} \right) \end{aligned} \quad (4)$$

Species continuity:

$$\begin{aligned} \frac{\partial}{\partial x'}(r'\rho'u'\alpha_i) + \frac{\partial}{\partial y'}(\kappa'r'\rho'v'\alpha_i) = & - \frac{\partial}{\partial y'}(\kappa'r'J'_{i,y}) \\ & + \kappa'r'\dot{\omega}'_i \end{aligned} \quad (5)$$

(i = 1, ..., N species)

Primed symbols are used to denote dimensional quantities, unprimed denote dimensionless quantities.

In the body-oriented coordinate system shown in Figure 3, the quantity κ' , which is the coordinate stretching function, is defined by

$$\kappa' = 1 + K'y' \quad (6a)$$

where

$$K' = K'(x) = \frac{1}{R'_b} \quad (6b)$$

and r satisfies the equation

$$dr' = \kappa' \sin \theta_b dx' + \cos \theta_b dy' \quad (6c)$$

The quantities $q'_{C,y}$, $q'_{D,y}$, and $q'_{R,y}$ are the heat fluxes in the y' -direction due to conduction, diffusion and radiation, respectively.

$J'_{i,y}$ is the mass diffusion flux in the y' -direction and $\dot{\omega}'_i$ is the net rate of production of the i th chemical species.

In comparison to the heat and mass diffusion fluxes in the y' -direction, the corresponding fluxes in the x' -direction are generally considered negligible (see Ho and Probstein) in the stagnation region. These fluxes in the x' -direction are assumed to be negligible in the present analysis also. The thin shock layer equations are the simplified boundary-layer equations (Navier-Stokes) including the curvature terms for the stagnation region. The equations are considered to be accurate to the order $\left(\frac{\rho'_\infty}{\rho'_s} \text{Rey}_s\right)^{-1}$ (see Ho and Probstein), where $\text{Rey}_s = \frac{\rho'_\infty U'_\infty R'_b}{\mu'_s}$, when radiation is not considered.

Stagnation Streamline Equations

At the stagnation line ($x = 0$), the conservation equations for the thin shock layer reduce to ordinary differential equations upon expanding the flow variables in the following power series (based on symmetry considerations)

$$\left. \begin{aligned}
 u &= a(y)x + a_1(y)x^3 + \dots \\
 v &= v(y) + v_1(y)x^2 + \dots \\
 \rho &= \rho(y) + \rho_1(y)x^2 + \dots \\
 H &= H(y) + H_1(y)x^2 + \dots \\
 \alpha_i &= \alpha_i(y) + \alpha_{i1}(y)x^2 + \dots
 \end{aligned} \right\} \quad (7)$$

and applying the geometry relations (eq. (6)), then taking the limit as $x \rightarrow 0$. The limiting forms of the governing equations for the stagnation line flow become:

Continuity:

$$\frac{d(\kappa^2 \rho v)}{dy} = -2\kappa \rho a \quad (8)$$

X-momentum:

$$-\frac{\kappa}{\text{Rey}_s} \frac{d}{dy} \left(\mu \frac{da}{dy} \right) + \kappa \rho v \frac{da}{dy} + \rho a^2 + K \rho a = \beta \quad (9)$$

Y-momentum:

$$\rho v \frac{dv}{dy} = -\frac{dp}{dy} \quad (10)$$

Energy:

$$\kappa^2 \rho v \frac{dH}{dy} = -\frac{d}{dy} \left[\kappa^2 (q_{C,y} + q_{D,y} + q_{R,y}) \right] \quad (11)$$

Species continuity:

$$\kappa^2 \rho v \frac{d\alpha_i}{dy} = -\frac{d}{dy} (\kappa^2 J_{i,y}) + \kappa^2 \dot{\omega}_i \quad (12)$$

where

$$a \equiv \left(\frac{du}{dx} \right)_{x=0} \quad (13)$$

$$\beta = \beta(y) = - \left(\frac{\partial^2 p}{\partial x^2} \right)_{x=0} \quad (14)$$

The foregoing conservation equations have been written in nondimensional form from the following set of dimensionless quantities:

$$\left. \begin{aligned} x, y, r &= \frac{x', y', r'}{R_b}; & K(x) &= K'(x) R_b'; & \kappa' &= \kappa \\ u, v, v_j &= \frac{u', v', v_j'}{U_\infty'}; & \rho &= \frac{\rho'}{\rho_\infty'}; & p &= \frac{p'}{\rho_\infty' U_\infty'^2} \\ h, H &= \frac{h', H'}{U_\infty'^2}; & q &= \frac{q'}{\rho_\infty' U_\infty'}; & \dot{\omega}_i &= \frac{\omega_i' R_b'}{U_\infty'} \\ J_i &= \frac{J_i'}{\rho_\infty' U_\infty'}; & \mu &= \frac{\mu'}{\mu_s'}; & k &= \frac{k'}{k_s'} \\ D_{12} &= \frac{D_{12}'}{U_\infty' R_b'}; & \text{Rey}_s &= \frac{\rho_\infty' U_\infty' R_b'}{\mu_s'}; & P_r &= \frac{c_p' \mu'}{k'} \end{aligned} \right\} \quad (15)$$

where the subscripts ∞ and s refer to free-stream and post-shock conditions, respectively.

Restrictions and Assumptions

The governing stagnation line equations are general equations and are restricted only by the requirements that $\rho_s/\text{Rey}_s \ll 1$ and that the radiative heat flux in the x -direction are comparatively negligible. At this point it is desirable to establish the state of the gas and the diffusion and heat flux models to be used in the study. The following basic restrictions and assumptions are imposed on the governing equations:

- (1) The gas is in local thermodynamic and chemical equilibrium.
- (2) Diffusion of the chemical species is governed by a binary diffusion model.
- (3) Radiative energy transport occurs within a one-dimensional, infinite planar slab (tangent slab).

Anderson indicates velocity and altitude limits for equilibrium and nonequilibrium chemistry, and it is observed that for the conditions of interest in this study, chemical equilibrium is considered to exist. However, to date no detailed calculations which consider the ablation products have been made to firmly establish this assumption.

The binary diffusion model, which assumes that the individual chemical species have the same mobility as the two chemical species which are used to represent the binary diffusion process, has been assumed in all previous radiation studies of this problem.

For the blowing situation, it is assumed that all the numerous chemical species of the ablation products can be represented by a single chemical specie and all the chemical species of air can be represented by the other single chemical specie to form the binary diffusion coefficient. Rigdon et al. (1969) examined atomic carbon-atomic nitrogen diffusion and atomic hydrogen-atomic nitrogen diffusion and concluded that the actual choices of the two chemical species to form the binary diffusion coefficient did not appear to be critical in the solution. A similar analysis of the effect of diffusion coefficient on the radiative heat fluxes will be made in this study.

Wilson (1970) indicated that he was considering a pseudo multi-component diffusion analysis (bifurcation model, see Graves) in which the individual binary diffusion coefficients computed for each combination of two individual chemical species are statistically lumped to

form an effective binary diffusion coefficient; however, the calculations have not been made to date.

The errors expected due to the tangent slab approximation have been previously discussed in the review of the literature and are about 5 percent or less for this problem (see Kennet and Strack, Koh and Hoshizaki, and Lasher). This approximation is made in RATRAP for the computation of the heat flux term that appears in the governing energy equation (eq. (11)).

Although additional assumptions, which are subsequently discussed, are required with regard to boundary conditions and second-order transport effects, the foregoing three assumptions are the most basic and restrictive assumptions which are required in this analysis. There is no way to establish firmly the validity of these basic assumptions for this problem, beyond the studies which have been previously cited, without introducing additional complexity to the calculations. However, it is anticipated that the implicit finite difference scheme should lend itself readily (conceptually) to both chemical nonequilibrium studies as demonstrated by Blottner's (1970) analysis and to multicomponent diffusion studies (Graves). It should be particularly useful for the nonequilibrium studies because stability requirements are not as stringent in this approach as in explicit forward integration schemes.

In order to uncouple the stagnation line solution from the remaining subsonic field, it is necessary to assume the relationship between the shock and the body curvatures at $x = 0$. In this analysis, as in most of the prevalent analyses, it is assumed that the shock and body are concentric. The results of Suttles (1969) inviscid radiating analysis indicates that the assumption is reasonable.

Preheating of the ambient air upstream of the shock wave due to radiation transport (precursor effects) is neglected. Smith, Hoshizaki, and Lasher, and Rigdon et al. indicate that precursor effects begin to become significant at velocities around 17 to 18 km/sec and above. Thus, the present solutions, which employ the Rankine-Hugoniot conditions (see Hayes and Probstein) for the discontinuous jump conditions across the shock, will be restricted to velocities somewhat lower than this.

In the numerical solutions, unless otherwise specified, a Newtonian pressure distribution (see Hayes and Probstein) is used to evaluate β , the $\left(\frac{\partial^2 p}{\partial x^2}\right)_{x=0}$ term in the x-momentum equation, i.e., $\left(\frac{\partial^2 p}{\partial x^2}\right)_{x=0} = -2.0$. It should be noted that Wilson (1970) used a value of -3.0 which can lead to a thinner shock layer in his calculations. This effect will be investigated in the present study.

The radiation transport computer code which is used in the radiation computations is RATRAP, developed by Hoshizaki and Wilson (see Wilson, 1967), which considers most of the primary radiating chemical species associated with carbon, oxygen, nitrogen, and hydrogen mixtures. The detailed thermodynamic and chemical composition calculations for equilibrium chemistry are performed in the computer code FEMP, developed by Brown et al. FEMP is included by Wilson as an integral part of RATRAP.

In the analysis, it is assumed that the transport properties for air developed by Hansen apply for both air-to-air injection and ablation-products-to-air injection. This assumption for the ablation products will be superficially analyzed by perturbations in the pertinent transport property (Prandtl number) to determine its effect. It should be noted that Rigdon et al. (1969) ran two identical cases with the exception of pure

air transport properties in one and the combined ablation products air transport properties in the other, and the resulting differences in the radiative heat fluxes to the wall were less than 1 percent.

The continuity and y-momentum equations (eqs. (8) and (10)) are unchanged when the foregoing assumptions are applied. The only perturbation in the x-momentum equation (eq. (9)) is the $\left(\frac{\partial^2 p}{\partial x^2}\right)_{x=0}$ term arising from the Newtonian (or specified) pressure distribution in which $\left(\frac{\partial^2 p}{\partial x^2}\right)_{x=0}$ will be taken to be a constant in y in this analysis.

The heat flux terms in the energy equation (eq. (11)) can now be defined by applying the binary diffusion and tangent slab approximations. The conductive heat flux term is given by Fourier's law of heat conduction

$$q'_{C,y} = -k'_C \frac{dT'}{dy'} \quad (16)$$

The multicomponent diffusion heat flux is given by Bird, Stewart, and Lightfoot as

$$q'_{D,y} = \sum_i^N h'_i \rho'_i (v'_i - v') = \sum_i^N h'_i J'_i \quad (17)$$

where $i = 1, \dots, N$ species.

For binary diffusion,

$$J'_i = -\rho' D'_{12} \frac{d\alpha_i}{dy'} \quad (18)$$

For constant pressure (pressure varies about 2 percent across the shock layer for this study),

$$\left(\frac{d\alpha_i}{dy'}\right) \approx \left(\frac{\partial \alpha_i}{\partial T'}\right) \frac{dT'}{dy'} \quad (19)$$

Equations (17), (18), and (19) can be combined to yield

$$q'_{D,y} = - \left[\rho' D'_{12} \sum h'_i \frac{\partial \alpha_i}{\partial T'} \right] \frac{dT'}{dy'} \quad (20)$$

The term in brackets of equation (20) has been defined by Hansen to be the "reactive" conductivity, k'_D , which yields a form of Fourier's law of heat conduction that describes the energy transport by binary diffusion. Hansen has computed and tabulated k'_D and the "lumped" or "effective" conductivity $k = k'_C + k'_D$ for air system for temperatures up to 15,000° K and pressures up to 100 atmospheres.

The radiative heat flux equation for the heat flux at a point within a one-dimensional slab is developed in the Appendix. That equation is

$$q'(y') = -2\pi \int_0^\infty \left[\int_0^{y'} \alpha_\nu B_\nu E_2 \left(\int_{\xi'}^{y'} \alpha_\nu d\xi' \right) d\xi' + \int_{y'}^{y''} \alpha_\nu B_\nu E_2 \left(\int_{y'}^{\xi} \alpha_\nu d\xi' \right) d\xi' \right] d\nu \quad (21)$$

where $E_2 \left(\int_{\xi'}^{y'} \alpha_\nu d\xi' \right)$ is the exponential defined by

$$E_2(\xi) = \int_0^1 e^{-\xi/\mu} d\mu$$

and is described by Kourganoff. B_ν is the Planck function and α_ν is the modified linear absorption coefficient which is a function of the temperature, pressure, and the chemical species number densities within the slab. The equation is valid for a non-gray self-absorbing gas. The absorption coefficients and radiative heat fluxes are computed in the radiation computer code RATRAP developed by Hoshizaki and Wilson (see Wilson, 1967). The radiation model takes into account both continuum and atomic line radiation exchange in a slab of non-uniform temperature.

The simplified energy equation can now be written as

$$\kappa^2_{\rho'v'} \frac{dH'}{dy'} = \frac{d}{dy'} \left[\kappa'^2_{k'} \frac{dT'}{dy'} \right] - \frac{d(\kappa'^2_{q'_{R,y'}})}{dy'} \quad (22)$$

where $q'_{R,y'}$ is given by equation (21). The combined conduction-diffusion heat flux term can be written in terms of total enthalpy from the following relations for static, total enthalpy, and "effective" Prandtl number:

$$\left. \begin{aligned} dh' &= c'_p dT' \\ H' &= h' + \frac{v'^2}{2} \end{aligned} \right\} \quad (23)$$

$$Pr = \frac{c'_p \mu'}{k'} \quad (24)$$

to yield

$$\kappa^2_{\rho'v'} \frac{dH'}{dy'} = \frac{d}{dy'} \left[\frac{\kappa'^2_{\mu'}}{Pr} \left(\frac{dH'}{dy'} - v' \frac{dv'}{dy'} \right) \right] - \frac{d}{dy'} (\kappa'^2_{q'_{R,y'}}) \quad (25)$$

Upon applying the nondimensional relations defined in equation (14) and rearranging equation (25), the dimensionless energy equation becomes

$$\frac{1}{Rey_s} \frac{d}{dy} \left(\frac{\kappa^2_{\mu}}{Pr} \frac{dH}{dy} \right) - \kappa^2_{\rho v} \frac{dH}{dy} = \frac{1}{Rey_s} \frac{d}{dy} \left(v \frac{dv}{dy} \right) + \frac{d}{dy} (\kappa^2_{q_{R,y}}) \quad (26)$$

The species continuity equation (12) undergoes considerable modification because of the binary diffusion and equilibrium chemistry assumptions. The species continuity equation was given by

$$\kappa^2_{\rho v} \frac{d\alpha_i}{dy} = - \frac{d}{dy} (\kappa^2_{J_{i,y}}) + \kappa^2_{\dot{\omega}_i} \quad (12)$$

Under the local chemical equilibrium assumption, the volumetric rate of production of species i is indeterminate. However, the fact that

the net rate of production of the mass fractions of the chemical elements is zero can be utilized to yield a tractable solution to the species continuity equation. Assuming that the binary diffusion law holds for the mass fractions, i.e.,

$$\bar{J}_i = -\rho D_{12} \frac{d\bar{\alpha}_i}{dy} \quad (27)$$

where the barred quantities refer to elemental mass fractions, the species continuity and diffusion equations can be combined to yield the elemental diffusion equation

$$\frac{d}{dy} \left(\kappa^2 \rho D_{12} \frac{d\bar{\alpha}_i}{dy} \right) - \kappa^2 \rho v \frac{d\bar{\alpha}_i}{dy} = 0 \quad (28)$$

The dimensional binary diffusion coefficient is given by Hirschfelder et al. as

$$D'_{ij} = 0.002628 \left[\frac{\left(\frac{T'^3 (M_i + M_j)}{2M_i M_j} \right)^{1/2}}{p' (\sigma'_{ij}) \Omega_{ij}^{(1,1)*}} \right] \quad (29)$$

where

$$\sigma'_{ij} = \frac{1}{2} (\sigma'_i + \sigma'_j)$$

$$\Omega_{ij}^{(1,1)*} = f \left(\frac{T'}{\frac{\epsilon'_{ij}}{k'}} \right)$$

and

$$\left(\frac{\epsilon'_{ij}}{k'} \right) = \left[\left(\frac{\epsilon'_1}{k'} \right) \left(\frac{\epsilon'_2}{k'} \right) \right]^{1/2}$$

The molecular constants σ_i and $\frac{\epsilon_i}{k}$ are tabulated by Svehla and are given in Table 1 for the chemical species of interest. The reduced collision integral, $\Omega_{12}^{(1,1)*}$ is based on the Lennard-Jones (12-6) potential and is taken from Hirschfelder et al. as a function of the nondimensional T_{ij}^* which is given by

$$T_{ij}^* = \frac{T'}{\left(\frac{\epsilon_{ij}}{k'}\right)}$$

For the binary diffusion model assumption, the individual elements of the ablation products and of the air which passes through the shock are considered to diffuse in the same respective manner as the two chemical species (one for the ablation products, the other for the air) used to form the binary diffusion coefficient. Thus, a distinction need not be made between the individual elements but only between the total mass fractions which represent the ablation products and the remaining mass fraction which represents the air products. Since the total mass fraction of all the elements (and, for that matter, the chemical species) must equal unity at any point, then one need solve only one elemental diffusion equation which is given by

$$\frac{d}{dy} \left(\kappa^2 \rho D_{12} \frac{d\tilde{\alpha}_F}{dy} \right) - \kappa^2 \rho v \frac{d\tilde{\alpha}_F}{dy} = 0 \quad (30)$$

where $\tilde{\alpha}_F$ is the total mass fraction of the elements of the ablation products. The total mass fraction of the air products, $\tilde{\alpha}_A$, is then computed by

$$\tilde{\alpha}_A = 1 - \tilde{\alpha}_F \quad (31)$$

The mass fractions of the individual elements are then calculated by the equations

$$\bar{\alpha}_i = \tilde{\alpha}_F \bar{\alpha}_{i,\text{inj}} + \tilde{\alpha}_A \bar{\alpha}_{i,\infty} \quad i = 1, N \quad (32)$$

where $\bar{\alpha}_{i,\text{inj}}$ is the specified elemental mass fraction of the i th element of the ablation products that is injected at the wall and $\bar{\alpha}_{i,\infty}$ is the same i th element that passes through the shock layer. The density and the individual chemical species are then calculated from an equation of state by the energy minimization subroutine (FEMP) where

$$\begin{aligned} \rho &= \rho(\bar{\alpha}_j, h, p) \\ \alpha_i &= \alpha_i(\bar{\alpha}_j, h, p) \end{aligned} \quad (33)$$

For viscous radiating stagnation line analyses, the resulting governing equations (8), (9), (10), (26), and (28) are the most general system of equations that are treated in the literature. These are the exact thin shock layer equations (for the tangent slab and binary diffusion assumptions) for the stagnation line which are solved in this analysis. As previously mentioned, Rigdon et al. (1968) and (1969) have applied initial value techniques for the numerical solution to this system of equations (with the exceptions that they assume constant pressure across the shock layer and neglect the curvature terms) for the massive blowing problem.

Transformed Equations

Before proceeding to the development of the solution technique, it is desirable to transform the governing equations by a change in independent variable from y to η , where

$$\eta = \frac{1}{\delta} \int_0^y \rho(y) dy \quad (34)$$

This transformation has the important effect of fixing the shock boundary at $\eta = 1$. The inclusion of density in the transformation gives, for a fixed nodal spacing in η , a finer resolution on a physical scale, y , at points near the body and within the boundary layer where conditions are rapidly changing.

The transformed system of equations become:

Continuity:

$$\frac{d(\kappa^2 \rho v)}{d\eta} = 2\delta \kappa a \quad (35)$$

X-momentum:

$$\frac{\kappa \rho}{\text{Rey}_s \delta} \frac{d}{d\eta} \left(\mu \rho \frac{da}{d\eta} \right) + \frac{\kappa \rho^2 v}{\delta} \frac{da}{d\eta} - \rho a^2 + \kappa \rho v a = -\beta \quad (36)$$

Y-momentum:

$$\frac{dp}{d\eta} = -\rho v \frac{dv}{d\eta} \quad (37)$$

Energy:

$$\frac{d}{d\eta} \left(\frac{\kappa^2 \rho \mu}{\text{Pr}} \frac{dH}{d\eta} \right) + \delta \text{Rey}_s \kappa^2 \rho v \frac{dH}{d\eta} = \frac{d}{d\eta} \left(\frac{\kappa^2 \mu}{\text{Pr}} \rho v \frac{dv}{d\eta} \right) + \delta \text{Rey}_s \frac{d}{d\eta} (\kappa^2 q_{R,\eta}) \quad (38)$$

Elemental diffusion:

$$\frac{d}{d\eta} \left(\kappa^2 \rho^2 D_{12} \frac{d\tilde{\alpha}_F}{d\eta} \right) + \delta \kappa^2 \rho v \frac{d\tilde{\alpha}_F}{d\eta} = 0 \quad (39)$$

Equation of state:

$$\rho = \rho(\bar{\alpha}_i, h, p) \quad (40)$$

The reader is cautioned that the normal velocity, v , has been redefined as negative in the positive y or η direction in the above equations. This change in no way affects the solution to the

equations since the boundary conditions, as will subsequently be discussed, have been appropriately modified to reflect this change. The primary reason for the change in the sign of v is to aid future users of the computer program to understand the signs on the equations as they are programed. In programing the governing equations, the author chose to define velocities in the direction of the free-stream flow (negative y -direction) as positive. The flow field coordinate system for the stagnation line in the transformed coordinates is shown in Figure 4.

Eta is specified as zero at the body and as unity at the shock. The normalizing parameter, δ , is an unknown in the problem which is obtained from the solution of the continuity equation (35) and is given by the relation

$$\delta = \frac{-(\kappa^2 \rho v)_w + (\kappa^2 \rho v)_s}{2 \int_0^1 \kappa a \, d\eta} \quad (41)$$

Boundary Conditions

The subsonic flow field in the nose region is governed by elliptic equations; consequently, the stagnation streamline solution is influenced by the flow within the entire subsonic region. However, this influence only enters in the β term, i.e., $\left(\frac{\partial^2 p}{\partial x^2}\right)_{x=0}$ in the x -momentum equation (36) and in the curvature of the shock wave which provides the boundary condition for the tangential velocity gradient, as at the shock wave. For a shock wave and body which are concentric, the Rankin-Hugoniot relations yield the following relation between $\left(\frac{\partial^2 p}{\partial x^2}\right)_{x=0}$ and the velocity gradient, a_s (see Hayes and Probstein)

$$\beta = -\left(\frac{\partial^2 p}{\partial x^2}\right)_{x=0} = 2\left(1 - \frac{1}{\rho_s}\right)a_s^2 \approx 2a_s^2 \quad (42)$$

Newtonian impact theory predicts (see Hayes and Probstein)

$$\left(\frac{\partial^2 p}{\partial x^2}\right)_{x=0} = -2.0 \quad (43)$$

thus,

$$a_s = \left(-\frac{1}{2} \frac{\partial^2 p}{\partial x^2}\right)^{1/2} = 1.0$$

With β and a_s specified, the stagnation streamline problem becomes a two-point boundary value problem, where conditions are specified at the shock wave and at the body. The boundary conditions necessary to solve the transformed conservation equations for the flow of a viscous radiating gas with foreign species injection, where the chemical species are in local thermodynamic equilibrium are:

At the body surface (wall), $\eta = 0$ ($y = 0$):

$$\left. \begin{aligned} a &= a_w = 0 \\ \rho v &= (\rho v)_w \\ p &= p_w \approx p_s + \frac{1}{2}(\rho v^2)_s \\ H &= H_w \\ \bar{\alpha}_i &= \bar{\alpha}_{i, \text{inj}} \text{ (and } \tilde{\alpha}_F = 1) \quad i = 1, \dots, N \text{ elements} \end{aligned} \right\} \quad (44)$$

where the $\tilde{\alpha}_F = 1$ boundary condition applies for condition of strong blowing.

At the shock wave, $\eta = 1$ ($y = y_s$):

$$\left. \begin{aligned} a &= a_s = 1.0 \\ \rho v &= (\rho v)_s = 1.0 \\ p &= p_s \\ H &= H_s = H_\infty \\ \bar{\alpha}_i &= \bar{\alpha}_{i,\infty} \text{ (and } \tilde{\alpha}_F = 0) \quad i = 1, \dots, M \text{ elements} \end{aligned} \right\} \quad (45)$$

where $\bar{\alpha}_{i,\text{inj}}$ is the mass fraction of element i which is injected at the wall, and $\bar{\alpha}_{i,\infty}$ is the mass fraction of element i which passes through the shock wave from the free stream. Conditions immediately behind the normal shock are computed from Rankine-Hugoniot relations. Heat fluxes across the slab boundaries are assumed to be zero, i.e., there is no precursor heating of the free stream by the shock layer and no radiation from the body into the shock layer.

Numerical Solution

The finite difference approximations to the governing equations (35) to (39) and the procedure for the numerical solution to this system of equations is developed in this section. The equations are written in finite difference form for a network of N equally spaced (in η) nodal points between the body ($n = 1$) and the shock ($n = N$) which are shown in Figure 5. For most of the calculations, 21 nodal points are used. The overall numerical solution technique is iteration. Profiles and parameters are assumed initially for each nodal point across the shock layer. The governing finite difference equations are then solved sequentially, using the most recent values of the profile parameters until satisfactory convergence is obtained at each nodal point.

Finite Difference Approximations

Either two- or three-point finite difference formulas are used to numerically differentiate and integrate the governing differential equations. Where possible, three-point central differences are employed since they are accurate (at a particular nodal point) to order $(\Delta\eta)^2$ where $\Delta\eta$ is the distance between points, whereas two-point differences are accurate only to order $\Delta\eta$ (see, e.g., Conte or Crandall). Two-point windward differences (with the flow) are employed for the convective terms where dictated by stability requirements of particular governing equations. The stability requirements are discussed in the Results and Discussion chapter.

The tabulation of the finite difference formulas that are employed to approximate the derivatives is given below (see, e.g., Conte or Crandall for the development). The formulas are valid for equally spaced increments in $\Delta\eta$.

The central differences formulas are:

$$\left(\frac{df}{d\eta}\right)_n = \frac{-f_{n-1} + f_{n+1}}{2 \Delta\eta} \quad (46a)$$

$$\left(\frac{d^2f}{d\eta^2}\right)_n = \frac{f_{n-1} - 2f_n + f_{n+1}}{(\Delta\eta)^2} \quad (46b)$$

$$\left[\frac{d}{d\eta}(cf)\right]_n = \frac{-c_n f_{n-1} - (c_{n-1} - c_{n+1})f_n + c_n f_{n+1}}{2 \Delta\eta} \quad (46c)$$

$$\left[\frac{d}{d\eta}\left(c \frac{df}{d\eta}\right)\right]_n = \frac{(c_{n-1} + c_n)f_{n-1} - (c_{n-1} + 2c_n + c_{n+1})f_n + (c_n + c_{n+1})f_{n+1}}{2(\Delta\eta)^2} \quad (46d)$$

where c and f are arbitrary functions.

In developing equation (46d), it has been assumed that c varies linearly between nodal points.

The windward difference formulas are either forward or backward differences, depending on the direction of the flow. If the mass flux, ρv , is positive (toward the body), forward differences are taken for the convective terms, and if ρv is negative, backward differences are taken. The formulas are:

If $(\rho v)_n > 0$,

$$\left(\rho v \frac{df}{d\eta} \right)_n = (\rho v)_n \left(\frac{f_{n+1} - f_n}{\Delta\eta} \right) \quad (47)$$

If $(\rho v)_n < 0$,

$$\left(\rho v \frac{df}{d\eta} \right)_n = (\rho v)_n \left(\frac{f_n - f_{n-1}}{\Delta\eta} \right) \quad (48)$$

Numerical integration is performed by the Simpson's rule approximation (Crandall) over parabolic sections of the profiles. The finite differences equations used in performing the quadrature over the interval from η_n to η_{n+1} and over the full interval from η_n to η_{n+2} are:

$$\left. \begin{aligned} \int_{\eta_n}^{\eta_{n+1}} f(\eta) d\eta &= \frac{\Delta\eta}{12} [5f_n + 8f_{n+1} - f_{n+2}] \\ \text{and} \quad \int_{\eta_n}^{\eta_{n+2}} f(\eta) d\eta &= \frac{\Delta\eta}{3} [f_n + 4f_{n+1} + f_{n+2}] \end{aligned} \right\} \quad (49)$$

Initial Profiles

For the general case, the following profiles are initially assumed:

$$\rho v(\eta) = (\rho v)_w + \left[(\rho v)_s - (\rho v)_w \right] \eta^2 \quad (50a)$$

$$p(\eta) = p_s + \frac{1}{2}(\rho v^2)_s(1 - \eta^2) \quad (50b)$$

$$a(\eta) = a_s \eta \quad (50c)$$

$$h(\eta) = h_w + (h_s - h_w)\eta \quad (50d)$$

$$\tilde{\alpha}_F(\eta) = (\tilde{\alpha}_F)_w(1 - \eta) \quad (50e)$$

$$\rho(\eta) = \rho(\tilde{\alpha}_i(\eta), p(\eta), h(\eta)) \quad (50f)$$

The density is computed in FEMP for a gas mixture in chemical equilibrium. All other quantities appearing on the right-hand side of the initial profile equations are available either from the input boundary conditions or they are computed from Rankine-Hugoniot relations for the normal shock.

The scale factor $\kappa = 1 + Ky = 1 + K\delta \int_0^\eta \frac{d\eta}{\rho}$ which, for large Reynolds numbers, typically is taken to be a constant of unity across the shock layer (Ho and Probstein) has been retained in the governing equations for this analysis. While κ exhibits only weak variations across the shock layer (for the typical cases of interest in this analysis κ varies from about 1.0 to 1.02 from the body to the shock for no blowing and from about 1.0 to 1.1 from the body to the shock for strong blowing (20 percent of $(\rho v)_s$), the computational time required to generate κ is insignificant in this problem. However, an initial

value for the transformed shock displacement, δ , is required as a consequence of retaining the κ . The physical shock displacement distance is correlated by Inouye to be

$$\frac{y'_s}{R'_b} \approx 0.78 \frac{\rho'_\infty}{\rho'_s}$$

for no blowing. Since $\frac{y'_s}{R'_b} = \delta \rho'_\infty \int_0^1 \frac{d\eta}{\rho'}$, then for a constant shock layer density of ρ'_s

$$\delta \approx 0.78$$

For moderate blowing,

$$\delta \approx 1 \tag{51}$$

which is the initial value assumed in this analysis.

This completes the statement of the problem of determining the initial profiles for the general case. The appropriate boundary conditions and initial profiles for special cases of interest, such as no blowing or air-to-air injection, are covered in the subsequent discussion of these special cases.

Solution Procedure and Finite Difference Equations

With the assumed initial profiles and parameters (eqs. (50) and (51)), the conservation equations are solved by successive iteration. The coupled system of equations are solved in the following sequence: continuity, y-momentum, elemental continuity, x-momentum, energy, and equation of state. The most recent values of the profile parameters and δ are used in the computations. The density distribution is necessary to solve the governing differential equations. After these equations have been solved, updated values of density are computed from

the equation of state which is compared with the previous density values at each nodal point. The entire sequence through the governing equations is repeated with the new density distribution until two successive passes yield nearly identical (within 1 or 2 percent) density values at corresponding nodal points. The flow diagram which illustrates the solution procedure is shown in Figure 6.

With the distribution for the tangential velocity gradient and the scale factor $\kappa(\eta)$, the continuity equation (35) is numerically integrated by Simpson's rule (eq. (49)) to give the updated shock displacement distance, δ :

$$\delta = \frac{-(\rho v)_w + (\kappa^2 \rho v)_s}{2 \int_0^1 \kappa a \, d\eta} \quad (52)$$

and the mass flux distribution $\rho v(\eta)$:

$$\kappa^2 \rho v(\eta) = 2\delta \int_0^\eta \kappa a \, d\eta + (\rho v)_w \quad (53)$$

The velocity profile, which is required in the solution of the y-momentum equation is computed from the previous density distribution, $\rho(\eta)$, and the updated mass flux distribution, $\rho v(\eta)$, namely

$$v(\eta) = \frac{\rho v(\eta)}{\rho(\eta)} \quad (54)$$

The y-momentum equation (33) is numerically integrated by Simpson's rule (eq. (45)) to give the pressure distribution $p(\eta)$:

$$p(\eta) = \int_{\eta}^1 \rho v \frac{dv}{d\eta} d\eta + p_s \quad (55)$$

The $\rho v(\eta)$ and $v(\eta)$ profiles are tabulated from the continuity equation solution and a central difference numerical differentiation scheme (eq. (46a)) gives $\frac{dv(\eta)}{d\eta}$ at the $N-2$ points within the shock layer. The values of $\frac{dv(\eta)}{dy}$ at the body and the shock boundaries are obtained from two-point forward and backward difference approximations, respectively.

The elemental diffusion equation (39) is cast in finite difference form by using the central difference formula (eq. (46d)) for the second derivative diffusion term and the windward difference equations ((47) and (48)) for the first derivative convective term. The resulting equations are:

For $n = 1$,

$$(\tilde{\alpha}_F)_1 = 1 \quad (56a)$$

For $n = 2, \dots, N-1$,

$$\begin{aligned} & \left[(\kappa^2 \rho^2 D_{12})_{n-1} + (\kappa^2 \rho^2 D_{12})_n - 2\delta(\Delta\eta)(\kappa^2 \rho v)_n (1 - \text{SIGN}) \right] (\tilde{\alpha}_F)_{n-1} \\ & - \left[(\kappa^2 \rho^2 D_{12})_{n-1} + 2(\kappa^2 \rho^2 D_{12})_n + (\kappa^2 \rho^2 D_{12})_{n+1} \right. \\ & \left. + 2\delta(\Delta\eta)(\kappa^2 \rho v)_n (1 - \text{SIGN}) \right] (\tilde{\alpha}_F)_n + \left[(\kappa^2 \rho^2 D_{12})_n + (\kappa^2 \rho^2 D_{12})_{n+1} \right. \\ & \left. + 2\delta(\Delta\eta)(\kappa^2 \rho v)_n (\text{SIGN}) \right] (\tilde{\alpha}_F)_{n+1} = 0 \end{aligned} \quad (56b)$$

For $n = N$,

$$(\tilde{\alpha}_F)_N = 0 \quad (56c)$$

where

$$\text{SIGN} = 0 \quad \text{if} \quad (\rho v)_n < 0$$

and

$$\text{SIGN} = 1 \quad \text{if} \quad (\rho v)_n > 0$$

The formulation results in a banded (tridiagonal) matrix system of equations of the form

$$\begin{bmatrix} B_1 & C_1 & 0 & & & 0 \\ A_2 & B_2 & C_2 & & & 0 \\ 0 & A_3 & B_3 & C_3 & & 0 \\ \vdots & \vdots & \vdots & \vdots & \ddots & \vdots \\ 0 & & & A_{N-1} & B_{N-1} & C_{N-1} \\ 0 & & & 0 & A_N & B_N \end{bmatrix} \begin{bmatrix} (\tilde{\alpha}_F)_1 \\ (\tilde{\alpha}_F)_2 \\ (\tilde{\alpha}_F)_3 \\ \vdots \\ (\tilde{\alpha}_F)_{N-1} \\ (\tilde{\alpha}_F)_N \end{bmatrix} = \begin{bmatrix} D_1 \\ D_2 \\ D_3 \\ \vdots \\ D_{N-1} \\ D_N \end{bmatrix} \quad (57)$$

where A_n , B_n , and C_n are the coefficients of the $(\tilde{\alpha}_F)_{n-1}$, $(\tilde{\alpha}_F)_n$, and $(\tilde{\alpha}_F)_{n+1}$ terms, respectively, and D_n are the terms appearing on the right-hand side in equation (56). At the wall boundary, $n = 1$, the coefficients are $B_1 = 1$, $C_1 = 0$, $D_1 = 1$ and at the shock boundary, $n = N$, the coefficients are $A_N = 0$, $B_N = 1$, $D_N = 0$. The system of equations is easily solved by Potters' method, which is a form of Gaussian elimination that is efficient for solving a banded matrix system of equations (see Potters and Conte). The solution to equation (56) yields the total mass fraction distribution, at N nodal points, of the ablation products, subject to the constraint that $0 \leq (\tilde{\alpha}_F)_n \leq 1$. The

mass fractions of the individual air and ablation product elements are then computed from equations (31) and (32).

The transport properties, μ and P_r , required in the solutions to the x-momentum and energy equations are obtained from a tabular lookup as functions of the temperature, calculated in the FEMP subroutine, and the pressure, obtained in the y-momentum equation solution.

The x-momentum equation (36) is next solved. The equation is cast in finite difference form using the central difference expressions given by equation (46) to approximate the first- and second-order derivatives. Since the equation is nonlinear in the velocity gradient, a , an iterative procedure is required for its solution. A quasi-linearization approach (see Bellman and Kalaba) is employed which generates the solution by a rapidly converging iteration.

The x-momentum equation is quasi-linearized by the following technique: At a given nodal point, let

$$\begin{aligned} \left[a^{(i)} \right]^2 &= \left[a^{(i-1)} + a^{(i)} - a^{(i-1)} \right]^2 = 2a^{(i-1)}a^{(i)} \\ &\quad - \left[a^{(i-1)} \right]^2 + \left[a^{(i)} - a^{(i-1)} \right]^2 \end{aligned} \quad (58)$$

where the superscripts i and $i-1$ refer to the values of $a(\eta)$ at the i th and $i-1$ th iterations, respectively.

Upon assuming that

$$\lim_{i \rightarrow \infty} \left[a^{(i)} - a^{(i-1)} \right]^2 \rightarrow 0 \quad (59)$$

the x-momentum equation becomes linear in $a^{(i)}(\eta)$ where

$$\left[a^{(i)} \right]^2 \approx 2a^{(i-1)}a^{(i)} - \left[a^{(i-1)} \right]^2 \quad \text{as } i \rightarrow \infty \quad (60)$$

Combining the finite difference formula for the derivatives (eq. (46)) and equation (60) yields the finite difference form of the x-momentum equation:

For $n = 1$,

$$a_1^{(i)} = 0 \quad (61a)$$

For $n = 2, \dots, N-1$,

$$\begin{aligned} & \left\{ \frac{(\kappa \rho^2 v)_n}{2\delta(\Delta\eta)} - \frac{(\kappa \rho)_n [(\rho \mu)_{n-1} + (\rho \mu)_n]}{2\delta \text{Rey}_s (\Delta\eta)^2} \right\} a_{n-1}^{(i)} + \left\{ 2 \left[\rho a^{(i-1)} \right]_n \right. \\ & \quad \left. - (\kappa \rho v)_n + \frac{(\kappa \rho)_n [(\rho \mu)_{n-1} + 2(\rho \mu)_n + (\rho \mu)_{n+1}]}{2\delta \text{Rey}_s (\Delta\eta)^2} \right\} a_n^{(i)} \\ & \quad - \left\{ \frac{(\kappa \rho^2 v)_n}{2\delta(\Delta\eta)} + \frac{(\kappa \rho)_n [(\rho \mu)_n + (\rho \mu)_{n+1}]}{2\delta \text{Rey}_s (\Delta\eta)^2} \right\} a_{n+1}^{(i)} \\ & \quad = \beta + \left\{ \rho \left[a^{(i-1)} \right]^2 \right\}_n \end{aligned} \quad (61b)$$

For $n = N$,

$$a_N^{(i)} = a_s \quad (61c)$$

The subscript n refers to the n th nodal point in the shock layer and the superscript i refers to the i th iterative value of a .

For a linear iteration on the velocity gradient, a , let

$$a_n^{(i)} = a_n^{i-1} + \epsilon_n \quad (62)$$

where ϵ_n is the error in the i th iteration at the n th nodal point.

Substituting equation (62) for $a_n^{(i)}$ into equation (61) yields a tri-diagonal matrix system of equations of the form:

$$A_n \epsilon_{n-1} + B_n \epsilon_n + C_n \epsilon_{n+1} = \bar{D}_n \quad n = 2, \dots, N-1 \quad (63)$$

where the A_n , B_n , and C_n are the coefficients of the $a_{n-1}^{(i)}$, $a_n^{(i)}$, and $a_{n+1}^{(i)}$ terms, respectively of equation (61b) for $n = 2, \dots, N-1$.

The term \bar{D}_n is given by

$$\bar{D}_n = \beta + \left\{ \rho \left[a^{(i-1)} \right]^2 \right\}_n - A_n a_{n-1}^{(i-1)} - B_n a_n^{(i-1)} - C_n a_{n+1}^{(i-1)} \quad (64)$$

for $n = 2, \dots, N-1$. Since the boundary conditions are specified at the body and at the shock, then the equations at the boundaries become:

$$\left. \begin{aligned} \epsilon_1 &= 0 \quad (\text{or } A_1 = C_1 = D_1 = 0 \text{ and } B_1 = 1) \\ \epsilon_N &= 0 \quad (\text{or } A_N = C_N = D_N = 0 \text{ and } B_N = 1) \end{aligned} \right\} \quad (65)$$

The matrix system of equations (64) and (66) is solved by Potters' method and is iterated until

$$|\epsilon_n| \leq \tau \quad \forall n$$

In this study, this assigned convergence interval, τ , is 0.01.

The total enthalpy distribution is obtained from the tridiagonal matrix solution to the energy equation (38) in a single pass. As previously discussed, the total enthalpy derivative for the combined convective and diffusive heat flux terms is included explicitly in the matrix solution for the H_n 's, whereas the radiative flux term is computed using the enthalpy profile of the previous iteration and the updated pressure and elemental mass fraction profiles from the y-momentum and species diffusion equation solutions, respectively. The three-point central

difference formulas for the derivatives (eq. (46)) yield the following finite difference form of the energy equation:

For $n = 1$,

$$H_1 = H_w \quad (66a)$$

For $n = 2, \dots, N-1$,

$$\begin{aligned} & \left\{ \frac{1}{2 \Delta \eta^2} \left[\left(\frac{\kappa^2 \rho \mu}{P_r} \right)_{n-1} + \left(\frac{\kappa^2 \rho \mu}{P_r} \right)_n \right] - \frac{\delta \text{Rey}}{2 \Delta \eta} (\kappa^2 \rho v)_n \right\} H_{n-1} \\ & - \left\{ \frac{1}{2 (\Delta \eta)^2} \left[\left(\frac{\kappa^2 \rho \mu}{P_r} \right)_{n-1} + 2 \left(\frac{\kappa^2 \rho \mu}{P_r} \right)_n + \left(\frac{\kappa^2 \rho \mu}{P_r} \right)_{n+1} \right] \right\} H_n \\ & - \left\{ \frac{1}{2 \Delta \eta^2} \left[\left(\frac{\kappa^2 \rho \mu}{P_r} \right)_n + \left(\frac{\kappa^2 \rho \mu}{P_r} \right)_{n+1} \right] + \frac{\delta \text{Rey}}{2 \Delta \eta} (\kappa^2 \rho v)_n \right\} H_{n+1} \\ & = \left[\frac{d}{d\eta} \left(\frac{\kappa^2 \mu}{P_r} \rho v \frac{dv}{d\eta} \right) \right]_n + \delta \text{Rey} \left[\frac{d}{d\eta} (\kappa^2 q_{R, \eta}) \right]_n \end{aligned} \quad (66b)$$

For $n = N$,

$$H_N = H_\infty \quad (66c)$$

The derivative terms appearing on the right-hand side of equation (66b) are evaluated by the central differences formulas (eq. (46)).

The density distribution which was required in the solution to the governing differential equations can now be updated by the equation of state

$$\rho_n = \rho_n \left[(\bar{\alpha}_i)_n, p_n, h_n \right] \quad (67)$$

at each nodal point. The updated values of ρ_n provide the mechanism for iterating the governing equations. Upon setting ρ_n equal to either

the newly computed values or some percentage of the old values of density, $\rho_n^{(i-1)}$ and the new values $\rho_n^{(i)}$ (in order to speed convergence of the flow field solution), the entire procedure, beginning with the continuity equation, can be repeated until

$$\frac{|\rho_n^{(i)} - \rho_n^{(i-1)}|}{\rho_n^{(i)}} \leq \epsilon \quad \forall n \quad (68)$$

The interval of convergence ϵ used in this analysis is 0.02 or less.

Salient Features of the Implicit Finite Difference Algorithm

The implicit finite difference algorithm developed in the previous section is really quite simple, yet sufficiently flexible to treat the viscous radiating shock layer problem.

With the two- and three-point difference approximations for equally spaced increments, the governing thin shock layer equations can be made amenable to numerical solution without making unduly restrictive assumptions for the purpose of yielding analytically tractable solutions. The tridiagonal matrix system of equations which results can be efficiently solved by Potters' method, which requires only about $3n$ computations as contrasted to the $(n)^2$ computations required for a full matrix inversion.

Simple linear and quadratic profiles can be initially assumed as functions of the boundary conditions. Or, one may take advantage of prior knowledge of the solution behavior to begin with improved estimates of the profile parameters (i.e., read in the parameter values at each nodal point).

No singularities appear in the governing finite difference equations since division by ρv is not required in the present formulation of the

problem. In the region where ρv (or v) approaches zero, the diffusion terms become important in the elemental diffusion equation (eq. (56)). Likewise, the viscous terms predominate in the x-momentum and energy equations (eqs. (61) and (66)) near $\rho v = 0$.

The method is an implicit scheme in which the unknown quantities at point n are calculated as functions of conditions at surrounding points as well as conditions at the point itself. This is in contrast to explicit schemes where the unknown quantities at a point are evaluated solely as a function of conditions at a former point (such as the function and its derivative being evaluated at the $n-1$ point and then extrapolated to the n th point to determine the unknown function). For a given step size, implicit schemes are unconditionally stable (bounded), whereas explicit schemes may or may not be stable.

In the present approach to the two-point boundary value problem, the boundary conditions are specified at the shock wave and at the body. Since the matrix system of equations (for a particular governing equation) is completely coupled across the entire shock layer (e.g., note the appearance of $(\tilde{\alpha}_T)_n$ in the $n-1$ th, n th, and $n+1$ th elemental diffusion equations (eq. (56)) and the known boundary conditions are included in the system of equations, then the computed distributions between each endpoint are bounded and are monotonic in behavior (with the exception of the pressure, which reaches a maximum at the stagnation point). Thus, one has near-maximum information about the behavior and levels of the unknowns which are to be computed and also a high degree of assurance that the computer run will not be aborted because of overflow (numbers larger than the computer will accept).

Perhaps one of the biggest advantages of the present approach over initial value methods resides in the limited number of unknown quantities which must be evaluated in order first to satisfy the governing differential equations and, second, to provide the necessary inputs for the radiative flux computations. In the present method, the unknowns are only the properties themselves (ρv , p , etc.) at each nodal point about which one has maximum information as to the bounds on the values and the general behavior of the properties across the shock layer. In contrast, consider the computations which must be performed in an initial value treatment of the problem (such as Runge-Kutta forward integration). In the initial value approach for the solution of a single governing equation, the unknown property and also its derivative must be computed. Generally, little information is available as to the behavior of the derivative across the shock layer. As a consequence, the function or derivative changes from point to point are generally closely controlled, by restricting the step size, to maintain stability as the calculations proceed downstream.

Yet there are several clear advantages of the initial value treatment of the complete system of coupled governing equations. If all boundary conditions are matched at the downstream side in the iterative process, then, because of the strict stability requirements, one is reasonably assured that all governing equations have been satisfied both locally and globally, and the detailed distributions are sufficient for the radiation computations. Whereas, in the implicit finite difference approach, there is no assurance apriori that the coupled system of equations will converge in the overall iteration scheme. It may be possible that two equations (e.g., the continuity and the x-momentum)

may interact with one another such that the ρv and a profiles oscillate back and forth and never converge. Further, there is no controlled step size from stability considerations. Thus, care must be exercised in inputting the nodal spacing which will satisfy the governing equations both locally and globally. An indication of the required nodal spacing can be obtained by a cursory examination of stability requirements for the individual equations and by decreasing the step size until the numerical solutions become asymptotic. These aspects, along with the convergence behavior of the overall solution, are examined in the Results and Discussion chapter which follows.

RESULTS AND DISCUSSION

In this chapter the numerical results obtained from the solution to the governing equations developed in the previous chapter are presented and discussed. The solutions which were obtained in the various phases in the development of the method are presented in the sequence of their development, beginning with the constant density solutions and continuing through the viscous radiating shock layer solutions with ablation products injection. Results are compared with results from existing approaches to the radiating flow field problem.

All numerical solutions were generated on a Control Data Corporation CDC 6600 digital computer.

Constant Density Solutions

The results of the constant density study are presented in this section. The convergence behavior of the solution for the reduced system of equations that govern the flow of a constant density gas is examined. Selected solutions are shown for inviscid and viscous flows. Results are presented for a range of blowing rates and Reynolds numbers.

The overall solution to the governing equations is by iteration until satisfactory convergence is obtained on the density. For a constant density assumption (and a viscosity and Reynolds number specification required for the viscous flow solution), the continuity, x-momentum, and y-momentum equations can be solved independent of the energy and diffusion equations. Naturally, the density is not iterated; however, the remaining system of equations (continuity and x- and y-momentum) are still coupled and, in the present approach, an iterative scheme is required for their solution as indicated by Figure 6. The

equations are solved "one at a time" by a method successive approximations until the computed values of ρv , a , and p for two consecutive iterations are within a specified accuracy at each nodal point. The constant density solutions thus serve a twofold purpose. First, the solutions provide a most fundamental means of studying the convergence behavior of the coupled system of equations for a wide variety of blowing rates and Reynolds numbers and thus permits an assessment of the adequacy of the successive approximation iterative scheme. Second, it provides an indication as to the nodal spacing requirements for the implicit finite difference equations formulation.

Several cases were run for a range of typical blowing rates ($(\rho v)_w = 0$ to -0.2), Reynolds numbers ($Re_{y_s} = 1$ to 10^5), and nodal spacings ($N = 11$ to 101) for a constant density of 20. and a viscosity of 1.0. All solutions required about three or four iterations and a total 2 to 4 seconds of computer time. No discernible differences were observed in the computed ρv , p , and a profiles or δ for $N = 11$ and $N = 101$. It was observed that the computer times were a function on the number of nodal points (the 2- and 4-second run times were for the $N = 11$ and $N = 101$ cases, respectively), whereas increasing the blowing rates or Reynolds number had little or no effect on the computer run times.

The convergence behavior of a typical constant density is shown in figure 7 where the successive solutions to the continuity and x-momentum equations are plotted. The solution is for a constant density of 20., a constant viscosity of 1.0, a typical Reynolds number of 10^5 , and a blowing rate at the wall of -0.2 . Twenty-one nodal points were used in

the computations. Initial linear profiles for $\rho v(\eta)$ were assumed. The accuracy criteria required that the computed values of $\rho v(\eta)$, $p(\eta)$, and $a(\eta)$ for two consecutive iterations be within 0.01 at each nodal point (i.e., $|\rho v_n^{(i)} - \rho v_n^{(i-1)}| \leq 0.01 \quad \forall n$). This accuracy criterion was maintained throughout the entire course of the present study of viscous radiating flows. As indicated by the legend in Figure 7, the solution converged in four iterations which required about 3 seconds of computer time.

Three constant density solutions for no blowing are shown in Figure 8: an inviscid case and two viscous cases for Reynolds numbers of 1 and 10^5 . The $Rey_s = 10^5$ case is typical of the Reynolds number of interest, whereas the $Rey_s = 1$ is actually outside the limits of applicability of the thin shock layer equations and is shown merely to demonstrate that the present approach yields solutions over the entire range of Reynolds numbers. The effect of the boundary layer and its extent can be seen in Figure 8(a). For inviscid flow there is no boundary layer and a nonzero velocity gradient exists at the wall which, from equation (36), is given by $a_1 = \sqrt{\beta/\rho_1}$. For the $Rey_s = 10^5$ case, most of the shock layer is inviscid, with only a thin boundary layer present near the wall (to $\eta \approx 0.03$) where the velocity gradient slope in y (i.e., da/dy) is a maximum, whereas for the $Rey_s = 1$ case, the entire shock layer is viscous and no abrupt changes in da/dy are observed. The plot in Figure 8(b) indicates that there is little difference in the mass flux distributions in the inviscid and $Rey_s = 10^5$ cases. Also shown in the figure are the transformed shock layer thicknesses, δ for the three cases. In the inviscid case, the

stagnation line analysis yielded a value for δ of 0.796, which is close to the value correlated by Inouye ($\delta = 0.78$) from inviscid analyses for the entire subsonic flow field surrounding a spherical body. In the $Re_{y_s} = 10^5$ case, the shock layer thickness, δ is about 2 percent greater than that for the inviscid case, whereas for the $Re_{y_s} = 1$ case, the shock layer thickness increased about 25 percent.

The influence of the blowing rate on the velocity gradient and the shock layer thickness, y_s , for a constant density is shown in Figure 9 where a is plotted in the physical coordinate system. The figure indicates that the inner flow region from the body to the stagnation point ($y_s - (y)_{\rho_v=0} \approx 0.041$) is drastically modified due to blowing but that the inviscid outer flow is virtually unaffected by the blowing rate. For the constant density model, the shock wave simply moves outward from the body as the blowing rate increases while the inviscid outer flow retains the same character independent of the blowing rate.

The constant density results demonstrate that, for a wide range of blowing rates and Reynolds numbers, the solution to the flow equations converges in a minimum number of iterations, the nodal spacing requirements are indeed moderate, and the computational times are reasonably short. With this knowledge, the behavior of the overall solution with the variable density iteration can now be examined.

Non-Radiating Air Solutions

The overall convergence of the flow solution for a variable density is examined in this section for an equilibrium air-gas mixture without

radiation. Solutions for both non-blowing and the blowing of air into air are presented. The air model consists of elemental mass fractions of 0.78 nitrogen and 0.22 oxygen.

The development of stability criteria is difficult even for the simplest of equations. For the coupled system of nonlinear equations which are solved in this study, it becomes necessary to rely on the behavior of the numerical solution in order to obtain information of the overall stability and convergence behavior of the solution. The results of the information are reflected in the logic presented in the flow diagram for the overall solution procedure shown in Figure 6. It should be emphasized that Figure 6 represents the results of the stability study which is used in all subsequent studies. The numerical results which led to this particular iterative procedure for the variable density solutions are discussed below.

The solutions to be presented below are for the following free-stream conditions unless otherwise noted.

$$U_{\infty}' = 14.6 \text{ km/sec}$$

$$p_{\infty}' = 1.6 \times 10^{-4} \text{ atmos}$$

$$\rho_{\infty}' = 2.38 \times 10^{-7} \text{ gm/cm}^3$$

$$R_b' = 342.7 \text{ cm}$$

It was observed in the numerical solution that major oscillation occurred in the enthalpy and the density, particularly in the viscous region of the flow, as the iterative procedure progressed in time. These enthalpy oscillations are shown in figure 10, which is a plot of the calculated enthalpies at the first three nodal points adjacent to

the wall and within the shock layer (Note that $H_1 = H_w = 0.1$ and is constant.) versus iteration number, where one iteration represents one complete pass through the governing equations. From the figure it can be seen that the amplitudes of the oscillations generally decrease with η and, while it is not shown here, it was observed that after about five iterations the enthalpy values had converged beyond $\eta \approx 0.3$. However, the solutions near the wall did not converge but merely continued to oscillate even after thirty iterations.

The density profiles exhibited a similar oscillatory behavior as the enthalpy profiles but in an inverse fashion (i.e., an overprediction of the enthalpy led to an underprediction of the density). This is because there is a strong inverse coupling between the density and the enthalpy in the equation of state. The equation of state for air has been correlated by Smith, G. L. (see Garrett, Smith, and Perkins) in the form $p \propto \rho^a h^b$, where a and b are positive exponents. Since p is nearly constant, then an overprediction of the enthalpy obtained in the energy equation is a corresponding underprediction of the density from the equation of state and vice versa. It is possible to get into a resonant computing mode in which the density and the enthalpy oscillate back and forth and can be slowly convergent or even divergent.

From the results it was not clear that the solution was divergent; however, it was apparent that if it was converging near the wall it was prohibitively slow.

Since the calculations appear to be oscillating about the solution, then by proper damping of the calculated quantities it is possible to speed convergence. Fox has discussed the method of underrelaxation whereby the quantity(s) which are highly oscillatory are weighted (or

damped) before they are used in subsequent calculations. It was found that by weighting the enthalpy and the density profiles by a certain percentage of their former value and their newly calculated values, rapid convergence of the overall solution could be obtained. The weighted values of the enthalpy and the density at each nodal point are computed from the following relations:

$$h_n = (\text{HDAMP})h_n^{(i-1)} + (1 - \text{HDAMP})h_n^{(i)}$$

and

$$\rho_n = (\text{RODAMP})\rho_n^{(i-1)} + (1 - \text{RODAMP})\rho_n^{(i)}$$

The convergence behavior of the solution for damping factors of 0.5 and 0.9 is shown in Figure 11. Plotted in this figure are the weighted enthalpy and the density values computed at nodal point 2. Both solutions converged; however, it is apparent that, while over-damping will insure convergence of an otherwise oscillatory solution, it can be unduly time consuming. For most of the cases examined, both with and without blowing, the 0.5 damping factors appeared to be near optimum in terms of generating a converged solution in a minimum number of iterations. For damping factors around 0.2 to 0.3, certain solutions would converge but required more iterations than the 0.5 damping factor cases. It was also observed that for the largest blowing rate (-0.2) considered in this analysis, damping factors of 0.7 speeded convergence of the solution by about a factor of 2 over the 0.5 damping factor solution. Because of the sensitivity of the computer run times to the damping factors, and since no attempt was made in the present study to optimize the damping factors for a particular solution beyond that

which was just discussed, the reader is reminded that subsequent discussions of computer time relate closely to the 0.5 damping factors. With a thorough study of damping factor requirements for optimum solutions, run times may be improved significantly.

In order to obtain an indication of the stability of the variable density solution for various blowing rates, three cases for blowing rates of 0, -0.1, and -0.2 were examined. The same free-stream conditions given previously and the 0.1 wall enthalpy value was specified. Twenty-one nodal points were used across the shock layer. All solutions converged to an absolute density accuracy of 0.01 for damping factors of 0.5. It was observed that the number of iterations of the governing equations, and consequently the run times, increased with increasing blowing rate. For the $(\rho v)_w = 0$, -0.1, and -0.2 cases, the number of iterations required to obtain convergence were 11, 16, and 21, respectively, and the corresponding computer times were 1.5, 2.5, and 3.5 minutes, respectively. The computer run times are well within reason for the fully viscous shock layer with equilibrium air chemistry computations.

The results obtained for the $(\rho v)_w = 0$ and -0.1 cases are shown in Figure 12. On a physical scale the boundary layer for the $(\rho v)_w = 0$ case occupies about 5 percent of the shock layer and the combined inner layer and boundary layer for the $(\rho v)_w = -0.1$ case occupies about 20 percent. The $(\rho v)_w = -0.2$ results are not shown in the figure. The $(\rho v)_w = -0.2$ solution converged; however, in the inviscid outer region the enthalpy profiles were extremely irregular. Enthalpy values ranging from 0.45 up to about 0.7 (the latter value being greater than the free-stream total enthalpy) were observed. To a similar degree,

density profile irregularities and minor inconsistencies in the velocity gradient profiles were observed. Initially, it was felt that this oscillatory behavior of the enthalpy was due to the non-radiating gas assumption because the conditions were sufficient to produce non-adiabatic effects in the outer inviscid region. About this time in the study, the radiation computer code was fully incorporated into the program and results were being generated with the radiation flux term included in the energy equation. And, indeed it was observed that the slight oscillations which were present in the enthalpy distribution in the outer inviscid region for the $(pv)_w = 0$ and 0.1 cases (Fig. 12(d)) were not observable in the radiating flow field solutions.

It appeared that the solutions were indicating that the radiative fluxes must be taken into account in the energy equation at the 14.55 km/sec velocity. Thus it was decided to run a lower velocity case of 10 km/sec where radiation is not significant, and to observe the behavior of non-blowing and massive blowing solutions, particularly the enthalpy distributions. The results of this study are shown in Figure 13 for $(pv)_w = 0$ and -0.2 blowing rates. The numerical results show that while there is improvement in the solutions for the lower velocity case, the oscillatory behavior of the energy equation solution persisted. In retrospect, the improved behavior for the lower velocity case is due to the decrease in the Reynolds number (7.8×10^4 and 4.0×10^4 for the $U_\infty = 14.55$ km/sec and the $U_\infty = 10.0$ km/sec cases, respectively) which permits a coarser nodal spacing.

It was observed much later in the study, when the solution to the elemental diffusion equation was required for the foreign ablation

product injection study, that the energy equation and the elemental diffusion equations are similar and have coefficients on the derivative terms which under further dimensional analysis reduce to about the same order of magnitude. As will be subsequently discussed, the elemental diffusion equation can be unstable unless the nodal spacing is made prohibitively small ($\Delta\eta \approx 10^{-4}$) and a windward difference formulation is required to obtain meaningful $\tilde{\alpha}_1$ profiles. The one notable difference in the two equations is the appearance of the radiative heat flux and term in the right-hand side of the energy equation. When radiation was included, this term provided sufficient damping in the computations to yield accurate solutions to the energy equation. However, as a consequence of the elemental diffusion equation study, a windward difference form of the energy equation was also examined. Certain radiating cases were rerun, replacing the central difference form of the energy equations, which is used in most of the results to follow, with the windward difference form. It was noted there were no significant differences in the radiative heat flux at the wall. Comparisons of the results for the two formulations appear in a subsequent section.

Radiating Air Solutions

The viscous radiating shock layer solutions, including air-to-air injection are discussed in this section. The present results are compared with results from existing approaches.

General Results From the Present Analysis

The results obtained for $(\rho v)_w = 0, -0.1, \text{ and } -0.2$ cases are shown in Figure 14 for the following free-stream conditions:

$$U_\infty' = 15.25 \text{ km/sec}$$

$$\rho_\infty' = 2.72 \times 10^{-7} \text{ gm/cm}^3$$

$$\rho_{\infty}' = 1.95 \times 10^{-4} \text{ atm}$$

and a nose radius of 3.048 meters.

A wall enthalpy of 0.028 was specified which corresponds to a wall temperature of 3,600° K. This temperature is close to the steady state ablation temperature predicted by Smith et al. (1970). Twenty-one nodal points were used for all computations with the exception of the radiative flux computations where 11 points were used to avoid excessive computer time. The intermediate values of the radiative heat fluxes required in the energy equation solution were obtained by linear interpolation. Typical computer time ranged from about 30 minutes for the no-blowing case to about 70 minutes for the $(\rho v)_w = -0.2$ cases.

A comparison of the radiating solutions shown in Figure 14(a) with the non-radiating solutions shown in Figure 12(a) for slightly different free-stream and wall enthalpies shows that the physical shock displacement distance significantly decreases when radiation is taken into account. However, the mass flux distributions were only slightly altered in the η -coordinate system. The significant decrease in y_s when radiation is included is due largely to the non-adiabatic effects in the outer inviscid region which results in higher values in density (by almost a factor of 2 as shown by comparing Figures 12(e) and 14(e)) and to a somewhat lesser extent, the adjustment of the inner flow to the wall boundary conditions. On a physical scale the outer inviscid region occupies about 95, 75, and 60 percent of the total shock layer for blowing rates of 0, -0.1, and -0.2, respectively.

The y-momentum equation solution given in Figure 14(b) shows that in all cases the pressure, as expected, reaches a maximum at the stagnation point.

As previously mentioned, the inclusion of the radiative flux term in the energy equation has a damping effect on the solution. A comparison of the velocity gradient profiles shown in Figures 13(a) and 14(c) for $(\rho v)_w = -0.2$ shows that the waviness in the velocity profile vanishes when radiation is included. Further, the enthalpy profiles (Fig. 14(d) for $(\rho v)_w = 0$ and -0.1) are regular, and although the enthalpy profile for $(\rho v)_w = -0.2$ exhibits a slight waviness, it is considerably improved over the large oscillations shown in Figure 13(b) for the non-radiating cases. It is noted that this improvement was obtained at an even higher Reynolds number than the non-radiating cases ($Rey_s = 9 \times 10^4$ for the radiating case).

The radiative heat flux distributions across the shock layer are shown in Figure 14(f). The positive heat flux values indicate that the net radiative heat transfer is away from the body and the negative values indicate toward the body. The nondimensional heat fluxes at the wall are -0.0434 , -0.0390 , and -0.0369 ($q'_{R,w} = -4150$, -3740 , and -3490 watts/cm², respectively) for the $(\rho v)_w = 0$, -0.1 , and -0.2 cases, respectively. Thus for air-to-air injection at $(\rho v)_w = 0$, -0.1 , and 0.2 the radiative heating rates are reduced 10 and 18 percent, respectively, below the non-blowing rates. The absolute values of heat fluxes for the blowing rate cases decrease slightly in the inner region in the direction of the body; however, the results indicate that the inner air layer is only moderately effective in absorbing the incident radiation from the high-temperature outer layer.

It is observed in Figure 14(f) that the radiative heat fluxes reach a minimum near the stagnation point, which is expected based on an examination of the governing differential equations. This feature

provides an important self-test of the overall accuracy of the present method, i.e., the ability of the method to generate sufficiently accurate thermodynamic properties which, when input into the radiative heat flux computations, yield the minimum in the fluxes at the stagnation point.

More interesting and important checks on the adequacy of the present method for the stagnation line solution can be made by comparison with solutions to the entire subsonic flow field and by comparison with existing stagnation line solutions. The first exercise serves not only as a check on the accuracy of the solution but also as a check of the fundamental assumption that the stagnation line solution can be decoupled from the entire region of influence.

Comparisons of Non-Blowing Results With Existing Solutions

Shown in Figure 15 is a comparison of the enthalpy profiles generated in the present approach with the stagnation line enthalpy profiles obtained by Suttles (1969) from a one-strip method of integral relations solution and with those obtained by Falanga and Sullivan from an inverse method solution.

The solutions are for non-blowing, with the following free-stream conditions:

$$U_{\infty}' = 14.55 \text{ km/sec}$$

$$\rho_{\infty}' = 2.377 \times 10^{-7} \text{ gm/cm}^3$$

$$p_{\infty}' = 1.6 \times 10^{-4} \text{ atm}$$

and a nose radius of 3.427 meters. Both of the comparison solutions are extracted from complete radiating solutions to the entire subsonic flow field. The present solution is viscous, whereas the comparison

cases are for inviscid flows; however, the comparisons are still meaningful since for non-blowing conditions the boundary layer occupies only a small percentage of the shock layer. The RATRAP computer code was used in all three studies. The present solution for the enthalpy profile compares favorably with the inverse solution in the inviscid region for both $N = 11$ and $N = 21$ points with radiative flux calculations at 11 points. While the inverse solution is considered more accurate than the method of integral relations solution in defining shock layer profiles, it is interesting to note that the radiative heat fluxes predicted at the wall by the three methods fall within 3 percent of each other.

A complete summary of the radiative heat fluxes calculated at the wall is given in Table II for the cases examined in the present study. Also shown in the table are comparisons with existing sources.

Comparisons of Air-to-Air Injection Results With Existing Solutions

The viscous radiating solutions for air-to-air injection with $(\rho v)_w = -0.1$ are compared in Figures 16 and 17 for the following free-stream conditions:

$$U_\infty' = 15.25 \text{ km/sec}$$

$$\rho_\infty' = 2.72 \times 10^{-7} \text{ gm/cm}^3$$

$$p_\infty' = 1.95 \times 10^{-4} \text{ atm}$$

and a nose radius of 3.048 meters. The wall enthalpy is 0.028 which corresponds to a wall temperature of 3,600° K.

Shown in Figure 16 are comparisons across the entire shock layer with the results of Rigdon et al. (1969) and with results supplied by

Wilson* in a private communication from his method presented in 1970 and by Smith, G. L.* in a private communication from the Smith et al. (1970) method for identical conditions as those given above. In general, for air-to-air injection, the flow field results from all approaches are in fairly good agreement although there are notable detailed exceptions in the flow field structure which are discussed below. Also, the wall radiative heat fluxes computed by Wilson, Smith et al. and in the present analysis are within 5 percent, whereas the results of Rigdon et al. are about 30 percent higher. This disagreement is attributed primarily to the differences in the radiation model employed in the first three approaches (RATRAP) and that employed by Rigdon et al. (SPECS).

Although the radiative heat fluxes predicted by Wilson are in good agreement with the present method, there was a notable 10 percent difference in the shock layer thickness predicted by Wilson and by the other three approaches. The possible sources of this difference are associated with the x-momentum equation solution and are discussed below.

Tangential Velocity Gradient. There is fairly good agreement in all the tangential velocity gradient results in the inviscid outer region for all the solutions and, in general, somewhat poorer agreement near the body as shown in Figure 16(a). Near the body the present results for the velocity gradient are close to the results obtained by

*This author is indebted to Mr. K. H. Wilson of the Lockheed Aircraft Corporation and Dr. G. L. Smith of the Langley Research Center for generating the computer solutions for direct comparison with the present approach.

Rigdon et al. (1969). The major differences near the body in the present solution and those obtained by Wilson (1970) are due to differences in the computed inner layer and boundary layer thickness as shown in Figure 17(a).

The major source of the discrepancy in Wilson's inner region solution and the present results is probably due to differences in the assumptions made for the pressure gradient coefficient, $(\partial^2 p / \partial x^2)_{x=0}$. The higher the pressure coefficient, the more rapidly the oncoming flow sweeps around the body and, thus, the smaller the standoff distance. The value of the pressure gradient coefficient is not well defined at the present. Wilson assumes a coefficient of -3.0, whereas the value of -2.0 is assumed by Rigdon et al. and in the present analysis. Smith et al. use a value of -2.5 which has been correlated by Inouye on the basis of inverse flow field solutions.

A case was run to examine this effect. The pressure gradient coefficient was set to -2.5 and the shock was considered to remain concentric. Thus, the velocity gradient behind the shock became, by equation (42), $a_s = \sqrt{\beta/2} = 1.12$. The results indicated that the shock layer thickness decreased 7 percent, which agrees more closely with Wilson's shock layer thickness. However, most of the adjustment occurred in the outer inviscid region (by virtue of the higher velocity gradients in this region). As shown in Figure 18 there was not any significant change in the inner region of values of the velocity gradient or in the extent of the inner region.

Two assumptions are made by Wilson which are not necessary in the present method. First, because of numerical stability problems, Wilson treats the inner region as inviscid and begins his fully viscous

calculations near the inner region and boundary layer interface. A case was run assuming that the first five nodal points, up to $y/y_s \approx 0.04$ were inviscid. This was accomplished by setting $\mu = 0$ at these points. There was no discernible differences in the fully viscous and the inviscid/viscous solutions. This indicates that the inviscid inner region assumption is valid for the massive blowing problem.

The second assumption made by Wilson in his solution to the governing equations is that of a constant density viscosity product across the shock layer given by $\rho\mu = (\rho\mu)_w$. Since the value $\rho\mu$ within the boundary layer for the comparison case examined was about one-half that of the wall value, it was decided to examine this assumption. Two cases were run for $(\rho v)_w = 0$ and -0.1 in which the density viscosity products appear in x-momentum and the free energy equation was set equal to $(\rho\mu)_w$ at each nodal point. The results of the constant $\rho\mu$ cases and the corresponding variable $\rho\mu$ cases were nearly identical. This is shown in Figure 19. The results tend to indicate that while viscosity is important in the boundary layer, it need not be too well defined in the computations since the boundary layer is actually a thin transition region which adjusts to the outer and inner flow regions.

Returning to Figure 16(a), the results from the integral solution of Smith for the total shock layer thickness agrees fairly well with the present results; however, his inviscid inner layer thickness agrees more closely with Wilson calculations.

Also shown on this figure are the solution obtained by Wilson and Hoshizaki (1969) from their integral solution approach. The comparisons indicate that the method, which was sufficient for the non-blowing radiation studies, is not adequate for the strong blowing conditions.

Total Enthalpy. The total enthalpy results across the shock layer are compared in Figure 16(b). With the exception of the differences in the shock displacement distances which have been noted, the present results compare favorably with the results of Wilson. The enthalpy results of Smith et al. (1970) are fairly good overall. Their method is based on a one-strip integral relation solution for the outer inviscid flow coupled with an integral solution for the boundary layer and inner inviscid region. It is not expected to yield the detailed flow field structure results obtainable from the other approaches (i.e., Wilson (1970), Rigdon et al. (1969), and the present method).

Temperature. The temperature results obtained from the four approaches agree fairly well in the outer inviscid region with somewhat poorer agreement in the boundary layer and near the wall as shown in Figure 16(c). Since the radiative heat fluxes are strong functions of temperature, the results near the wall are compared in more detail in Figure 17(b). The present results compare favorably with the results of Wilson. It is unfortunate that, because of differences in the radiation models, no direct comparison can be made with Rigdon et al., who also solves the fully coupled viscous radiating shock layer equations. However, it is apparent from their temperature profile that the radiation model has a strong influence on the resulting temperature and the radiative heat flux predictions.

The temperature results of Smith et al. shown here indicate that the temperature is nearly constant in the inviscid inner region, whereas all other solutions indicate an appreciable drop in temperature going

toward the body due to radiation exchange. This author has been advised by Smith that their constant temperature results were due to a programing error which affected the energy equation solution near the wall and that they now expect the temperature to increase more rapidly with y .

Radiative Heat Flux. The radiative heat fluxes are shown in Figure 16(d). The present results indicate that the inviscid inner air layer is relatively ineffective in reducing the radiation to the wall and, as a consequence, the wall heat flux results of Wilson and of Smith et al., who predict thinner inner layers, agree well with the present results.

A summary of the predicted heat fluxes at the wall for the various air-to-air injection rates is given in Table 2-A.

It is interesting to note that the radiative heat fluxes at the wall converged much more rapidly than the detailed thermodynamic properties across the shock layer. A typical example of the sensitivity of the radiative heat flux at the wall on the density profile is shown in Figure 20. It was observed that the heat flux at the wall for the $(\rho v)_w = -0.1$ case converged within ± 2 percent of its final value after only five iterations, whereas the density values in the inner region ($\eta = 0.2$ and 0.4) were about 50 percent below their final value. This indicates that the radiative heat fluxes at the wall for air-to-air injection may not be as sensitive to the thermodynamic properties in the inner region as previously expected. If one is interested only in the gross quantity of the heat flux at the wall, then the 1 or 2 percent density convergence criteria could be relaxed considerably to provide substantial savings in computational time for air-to-air injection studies.

As previously noted, the air in the inner region is not too effective in absorbing the incident radiation from the high-temperature outer layer. However, since certain chemical species of ablators are strong absorbers and emitters, the flux to the wall may be sensitive to the relative amounts of these species. If this is the case, then a detailed definition of properties across the shock layer is desired. Thus, the density convergence criterion of 2 percent was retained in the subsequent ablation study.

Stability Study of the Elemental Diffusion and Energy Equations

The solution to the elemental diffusion equation is required in the analysis of the radiating shock layer with ablation product injection. In extending the present method from the air-to-air injection analysis to the ablation products injection into air, it became evident that problems of numerical stability existed in the solution of the elemental diffusion equation. Presented in this section is the stability study which led to the windward difference formulation for the elemental diffusion equation and the subsequent reexamination of the energy equation formulation.

Initially, a central difference form of the elemental diffusion equation was used and an attempt made to solve the fully viscous radiating shock layer equations, including ablation product injection. The diffusion equation solution was unstable in the first pass through the equation resulting in values of $\tilde{\alpha}_T$ at certain nodal points which were outside the ranges of $0 \leq \tilde{\alpha}_T \leq 1.0$. The program was immediately aborted in the equilibrium chemistry calculations because of negative mass fractions of the individual species. The reason for this instability was investigated both analytically and numerically.

The properties vary too rapidly across the shock layer in the variable density solution to perform any meaningful analytical analysis of the stability of the equation. However, some insight into the stability of the equation and the associated nodal spacing requirements can be obtained from a constant density, constant diffusion coefficient assumption.

For a constant ρ and D_{12} across the shock layer, the elemental diffusion equation (39) becomes

$$\rho v \frac{d\tilde{\alpha}_F}{d\eta} = - \frac{\rho^2 D_{12}}{\delta} \frac{d^2 \tilde{\alpha}_F}{d\eta^2}$$

Let

$$\frac{d\tilde{\alpha}_F}{d\eta} \equiv \alpha' = \gamma$$

thus,

$$\gamma' = - \frac{\rho v \delta}{\rho^2 D_{12}} \gamma$$

where the primes are used to denote the derivative.

Central differencing the two above equations yields

$$\frac{\alpha_{n+1} - \alpha_{n-1}}{2 \Delta\eta} = \frac{\gamma_{n+1} + \gamma_{n-1}}{2}$$

and

$$\frac{\gamma_{n+1} - \gamma_{n-1}}{2 \Delta\eta} = - \frac{\rho v \delta}{\rho^2 D_{12}} \left(\frac{\gamma_{n+1} + \gamma_{n-1}}{2} \right)$$

In matrix form the above equations become

$$\begin{bmatrix} \alpha_{n+1} \\ \gamma_{n+1} \end{bmatrix} = \begin{bmatrix} 1 & \begin{bmatrix} 1 - \frac{\rho v \delta}{\rho^2 D_{12}} \Delta \eta \\ 1 + \frac{\rho v \delta}{\rho^2 D_{12}} \Delta \eta \end{bmatrix} \Delta \eta \\ 0 & \begin{bmatrix} 1 - \frac{\rho v \delta}{\rho^2 D_{12}} \Delta \eta \\ 1 + \frac{\rho v \delta}{\rho^2 D_{12}} \Delta \eta \end{bmatrix} \end{bmatrix} \begin{bmatrix} \alpha_{n-1} \\ \gamma_{n-1} \end{bmatrix}$$

For stability, the determinant of the matrix must be positive (see, e.g., Crandall). Thus,

$$\frac{1 - \frac{\rho v \delta}{\rho^2 D_{12}} \Delta \eta}{1 + \frac{\rho v \delta}{\rho^2 D_{12}} \Delta \eta} \geq 0$$

The nodal spacing requirement for stability can be established when it is noted that

$$\delta = 0 \begin{bmatrix} 1 \end{bmatrix} \quad \text{and} \quad \rho v = 0 \begin{bmatrix} 1 \end{bmatrix}$$

For a constant density of 20, the nodal spacing requirement becomes

$$\Delta \eta \leq \left| \frac{\rho^2 D_{12}}{\rho v \delta} \right| = \frac{400 D_{12}}{0 \begin{bmatrix} 1 \end{bmatrix} 0 \begin{bmatrix} 1 \end{bmatrix}} \approx 0 \begin{bmatrix} 400 D_{12} \end{bmatrix}$$

Since D_{12} is typically of order 10^{-6} , then $\Delta \eta \leq 4 \times 10^{-4}$.

This nodal spacing requirement is prohibitive in this analysis since it would require at least 2,500 nodal points across the shock layer to generate a stable solution. However, a case was run in which 1,001 nodal points were used for the elemental diffusion equation solution with the same 21 points used for the other equations. Although some improvement was noted in the solution (for which only about 3 seconds was required to solve the diffusion equation), it did not eliminate the instability.

The numerical results which substantiate this stability analysis are shown in Figure 21. The computed mass fractions for a diffusion coefficient of 10^{-6} is shown in Figure 21(a) for a model spacing of 0.05. The solution is clearly unstable. The results obtained when the coefficient was increased to 1.25×10^{-4} and $\Delta\eta$ was set to 0.1 (which accomplishes the same stability effect as decreasing the model spacing to 4×10^{-4}) is shown in Figure 21(b). The sharp oscillations have vanished, but $\tilde{\alpha}_F$ still exceeded the value of 1.0. The case was rerun for a nodal spacing of 0.02 with no noticeable improvement. Only when D_{12} was raised to 10^{-3} did the $\tilde{\alpha}_F$ monotonically decrease from 1.0 at the wall to 0.0 at the shock.

Since the central difference form of the elemental diffusion equation was inadequate, a windward difference form for the convection term was employed. Windward differencing provides automatic damping of the profiles and has been shown in time-dependent studies of fluid and heat flow problems to be required in order to obtain meaningful solutions (see, e.g., Richmeyer; Larkin; and Khajeh-Nouri).

A physical explanation given for using windward differencing is that if fluid is flowing downstream the upstream cell influences the

downstream cell more than the downstream cell influences the upstream cell. It is correct for supersonic flow that the downstream conditions have no influence on the upstream flow, whereas the upstream conditions may have a pronounced effect on the downstream flow. Even for the stagnation line where the flow is subsonic and each cell or nodal point influences all other cells, the explanation that the upstream cell influences more than the downstream cell is palatable.

The mathematical reason for windward differencing is that higher order harmonics that are introduced into the solution because of finite difference approximations to the differential equations decay exponentially, whereas for central difference formulations these higher order disturbances can be exponentially amplified.

The results obtained for both central and windward difference forms of the diffusion equation are shown in Figure 22. The computations were for a viscous radiating solution assuming binary diffusion coefficient based on an atomic hydrogen-atomic nitrogen mixture. The windward difference formulation yields a stable solution in which $\tilde{\alpha}_F$ monotonically decreases across the shock layer.

A check case was run to establish the effect of the damping on the $\tilde{\alpha}_F$ profiles that is introduced by the windward difference formulation. This damping, which is a form of artificial viscosity, tends to smooth or smear out the gradients more than is natural. To check this, both central and windward difference solutions were obtained for diffusion coefficients which yield stable solutions for central difference approximations. The results from these two formulations, shown in Figure 23, indicate that the windward difference formulation does not introduce any noticeable artificial viscosity.

The enthalpy profiles in the non-radiating equilibrium air solution for the $(\rho v)_w = -0.2$ case were shown in Figure 13 to be unstable. These profiles exhibited an oscillatory behavior similar to the constant density $\tilde{\alpha}_F$ profiles for the central difference approximations. As previously mentioned, the enthalpy profiles became smooth when the radiation term was included, and at that time no more attention was devoted to the non-radiating solutions. However, after the elemental diffusion equation solutions were obtained, it was decided to reexamine the energy equation, neglecting radiation, to see if the central differencing assumption was responsible for the oscillations in enthalpy.

An order of magnitude analysis of the coefficients on the second derivative term of the energy and elemental diffusion equation revealed that these coefficients could be the same order of magnitude. This analysis is given below.

For constant density and constant transport properties assumption, the energy and the elemental diffusion equations (eqs. (38) and (39)), respectively, can be written as (where the convective term on the right-hand side of the energy equation has been neglected).

$$\rho v \frac{dH}{d\eta} = - \frac{\rho \mu}{\delta \text{ReyPr}} \frac{d^2 H}{d\eta^2}$$

and

$$\rho v \frac{d\tilde{\alpha}_F}{d\eta} = - \frac{\rho^2 D_{12}}{\delta} \frac{d^2 \tilde{\alpha}_F}{d\eta^2} = - \frac{\rho \mu}{\delta \text{ReySc}} \frac{d^2 \tilde{\alpha}_F}{d\eta^2}$$

where Sc , the Schmidt number, is given by

$$Sc \equiv \frac{\mu'}{\rho' D'_{12}}$$

Since the Prandtl and Schmidt numbers are typically of order unity, then the energy equation and the elemental diffusion equation are controlled by the same stability requirements.

As a result of this analysis, the convective term in the energy equation $\left(\rho v \frac{dH}{d\eta}\right)$ was recast in windward difference form and the non-radiating equilibrium air solution for $(\rho v)_w = -0.2$ was rerun. The enthalpy, density, and velocity gradient profiles became smooth. The x-momentum and energy equation solution results are plotted in Figure 24 and compared with the previous central difference solutions.

A significant change in the shock layer thickness also occurred when the windward difference form of the energy equation was used to improve the profiles. The shock layer thickness, y_s , was reduced by about 12 percent from 0.0703 to 0.0622 in going from central to windward difference form. It was found that this reduction in y_s was due primarily to the large blowing rate which introduced the strong oscillations in the profiles for the central difference formulation. The $(\rho v)_w = 0$ and $(\rho v)_w = -0.1$ non-radiating cases were rerun with the improved formulation of the energy equation. There was no change in y_s for $(\rho v)_w = 0$ and there was a 3 percent reduction in y_s for the $(\rho v)_w = -0.1$ case.

The strong oscillations in the enthalpy profiles were not present in the radiating solutions. However, the $(\rho v)_w = -0.1$ case for $U_\infty' = 15.25$ km/sec was rerun to determine the effect of the windward difference approximation in energy equations. The radiation flux at the wall was unchanged and shock standoff distance increased by only 2 percent.

As a result of this study it was decided to retain the windward difference form approximation for the radiating ablation products analysis which follows.

Radiating Flow Field Solutions With Ablation Products

The solutions to the fully coupled viscous radiating flow field with ablation products injection are presented in this section. The results of the present analysis are compared with existing solutions. The binary diffusion model assumption is also investigated in this section.

The heat-shield material is considered to be a carbon phenolic ablator composed of 90 to 95 percent carbon and the remaining elemental mass fractions consisting of nitrogen, oxygen, and hydrogen. Exact values of the elemental mass fractions of each of the constituents are specified for the particular cases presented.

Check on the Binary Diffusion Model Assumption

The binary diffusion coefficients were computed on the basis of the dominant species present. For the ablator, the dominant species is atomic carbon and for air it is atomic nitrogen, hence the binary diffusion coefficient for atomic carbon atomic nitrogen diffusion was used in the computations.

However, to obtain an indication of the validity of the assumption, two cases were run at identical conditions with the exception that atomic carbon/atomic nitrogen was used in one solution in calculating the diffusion coefficient and atomic hydrogen/atomic nitrogen was used in the other solution. A comparison of the elemental diffusion equation solution for the ablator mass fraction profiles with the two assumptions is shown in Figure 25 for the conditions noted there. The

two profiles show that the results differ in the mixing region and its extent, with the ablator elements extending further into the shock layer for the hydrogen-nitrogen diffusion coefficient. This is to be expected since D_{H-N} is almost an order of magnitude larger than D_{C-N} , as shown in the figure.

A detailed analysis of the heat flux distributions for the two cases indicated a maximum difference in the radiative heat fluxes of 3 percent which occurred in the outer inviscid mixing region ($\eta = 0.7$), as shown in Figure 26. At the wall, the nondimensional heat fluxes differed by less than 1 percent (-0.02892 and -0.02917 for D_{H-N} and D_{C-N} , respectively). The shock layer thicknesses, y_s , were 0.04173 and 0.04168 for D_{H-N} and D_{C-N} , respectively. Thus, it appears for the conditions examined in this study that the binary diffusion model assumption is valid.

General Results From the Present Analysis

The results obtained for $(\rho v)_w = 0$, -0.1 , and -0.2 cases are shown in Figure 27 for the following free-stream conditions:

$$U_\infty' = 15.25 \text{ km/sec}$$

$$\rho_\infty' = 2.72 \times 10^{-7} \text{ gm/cm}^3$$

$$p_\infty' = 1.95 \times 10^{-4} \text{ atm}$$

and a nose radius of 3.048 meters.

A wall enthalpy of -0.049 was specified which corresponds to a wall temperature of $3,600^\circ \text{ K}$ for the carbon phenolic ablator injection cases with the following elemental mass fractions:

$$\bar{\alpha}_C = 0.9207$$

$$\bar{\alpha}_N = 0.0086$$

$$\bar{\alpha}_O = 0.0491$$

$$\bar{\alpha}_H = 0.0216$$

For the non-blowing case, air is adjacent to the wall for which an enthalpy of 0.028 corresponds to the wall temperature of $3,600^\circ$ K.

In general, the profiles and parameters are much the same as those for the air injection cases with the exceptions of the enthalpy profiles for the $(\rho v)_w = -0.2$ case and the radiative heat flux predictions.

Even with the windward difference form of the energy equation, the enthalpy profile for the $(\rho v)_w = -0.2$ blowing rate was irregular near the stagnation point. This solution had not completely converged when the calculations were terminated on the computer after an accumulation of nearly 2 hours of machine time. However, it was near convergence. Apparently, this blowing rate is near the stability limit for obtaining the technique employed here for the solution to the governing equations. As can be seen in Figure 27(f), the density and temperature profiles, which are used in the radiative heat flux computations, are much better behaved than the enthalpy profiles.

It can be seen from the radiative heat flux profiles of Figure 27(g) that the flux out of the shock (at $\eta = 1.0$) increased with increasing ablator mass injection, whereas for the air-to-air injection cases the flux at the shock was nearly insensitive to the blowing rate (see Fig. 14(f)). The heat fluxes at the wall, which are of primary interest, decreased significantly with blowing rate for the carbon phenolic ablator (66 and 61 percent of the non-blowing radiative heat flux rate for the $(\rho v)_w = -0.1$ and -0.2 cases, respectively). Thus, the

ablation products are considerably more effective than air in reducing the heat flux to the wall.

It is not clear if the large negative heat flux near the stagnation point for the $(pv)_w = -0.2$ case is real or if it is a result of the uncertainty in the thermodynamic properties calculations. However, it is quite likely that the effects of this point on the resulting heat flux at the wall is washed out in the radiation exchange between this point and its surrounding points. This case is compared with the solution of Rigdon et al. (1969) in the next section.

Comparisons of Ablation Product Injection Results With Existing Solutions

Two carbon phenolic injection cases were run for comparison with the results of Smith et al. (1970) and Chin at a blowing rate of -0.076, and for comparison with Rigdon et al. (1969) at a blowing rate of -0.2. The pertinent free-stream and wall conditions are noted in Figures 28 and 29 for these corresponding cases. In general, the results for the thermodynamic and flow properties are in reasonable agreement, but there are noticeable exceptions relating to the heat flux computations which are discussed below.

In the Chin comparison case, it should be noted that the close agreement of the wall heat flux prediction with Chin's computations may be fortuitous. Chin's earlier radiation model is sufficiently different from RATRAP to make any quantitative comparison meaningless. This is evident from Table 2 where it is observed that the non-blowing radiation heat flux prediction of Chin and of the present method differ by 20 percent.

The comparison of interest for this case is with the results of Smith et al. (1970). It is noted in Figure 28(d) that the present

solution predicts a wall heat flux about 30 percent lower than that of Smith. An important conclusion made in their paper is that the radiation to the wall is not attenuated as much as previously predicted by Chin and by Rigdon et al. (1969). This was attributed to the presence of large percentages of CN in the mixing region which is a strong emitter. A comparison of the mole fractions of the major chemical species is shown in Figure 28(d). The comparisons are good considering the differences in the temperature distributions; however, it is noted that the peak mole fraction for CN predicted by the present method is only about one-half that of the comparison case. This discrepancy in the level of CN occurs in the region where Smith et al. (1970) employ a cubic fit to the elemental diffusion equation in order to join the wall products in the inner shear layer with the air composition beyond the boundary layer. It thus appears that contrary to the air-to-air injection study results which did not require too accurate a resolution of properties near the wall, the ablation products study indicates that these properties must be well defined near the wall to generate accurate wall radiative heat flux predictions.

The comparison with Rigdon et al. (1969) indicates reasonably good agreement in the radiative heat flux profiles, although there are significant differences in the radiation models employed. The predicted shock layer thicknesses are within about 5 percent. A slight waviness is noted in Rigdon's ρv profile (Fig. 29(a)) near the stagnation point ($y/y_s = 0.3$). In all the cases calculated by the present method, the ρv profile was smooth in this region. It is not apparent if this irregularity predicted by Rigdon et al. is real or if it related to their numerical procedure for integrating out in both directions from

the stagnation point. It is noted that their solution also exhibits an irregularity in the temperature profile near the stagnation point as does the present solution.

Summary of the Wall Radiative Heat Flux Predictions

A summary of the wall radiative heat fluxes calculated by the present method for the various conditions examined in this study and corresponding comparison results from previous investigations are tabulated in Table 2. With the exception of the non-blowing results of Suttles (1969) and the air injection comparison case with Wilson (1970), the present method predicts slightly to much lower heating rates than calculated by previous investigators.

These results are also summarized in Figure 30, which illustrates the effectiveness of the carbon phenolic ablator products in reducing the wall radiative heat fluxes. As can be seen from the figure, there is general agreement of all sources that air injection is moderately effective in reducing the heat transfer to the wall and, with the exception of the Smith et al. (1970) results, that the ablation products of the carbon phenolic heat shield is highly effective in reducing the fluxes.

As can also be seen from Figure 30 and Table 2, there is no consistent agreement from any sources when both the non-blowing and blowing results are considered. For sources which use different radiation transport models (Rigdon et al. (1969) and Chin), this disagreement is due, at least in part, to the differences in the radiation model. For sources which use the same model, Smith et al. (1970) and the present method, this disagreement is attributed to the numerical procedures employed. There was insufficient data available to fully evaluate

the Wilson (1970) results, with the exception of the assessment of the validity of the assumptions required in his analysis. These assumptions have been previously discussed and shown to be valid for the $(\rho v)_w = -0.1$ air-to-air injection case.

For air-to-air injection, the present results indicate a 10 and 17 percent reduction in the wall radiative heat fluxes for $(\rho v)_w = -0.1$ and -0.2 , respectively. For carbon phenolic ablation products injection at corresponding blowing rates, the reduction is 36 and 39 percent, respectively. Since ablation rates are typically expected to be about 0.1 (see Smith et al. (1970)), then the 36 percent reduction in the radiative heat fluxes represents a significant savings in heat-shield weight.

SUMMARY AND CONCLUSIONS

An implicit finite difference scheme is developed for the fully coupled solution of the viscous radiating stagnation line equations including strong blowing. Solutions are presented for both air-to-air injection and ablation products injection with blowing rates up to 20 percent of free-stream mass flow rates. The free-stream conditions examined are typical of interplanetary return conditions into earth's atmosphere near the point of peak radiative heating in the entry trajectory. A detailed radiative transport computer code (RATRAP) which accounts for both continuum and line radiation exchange processes is utilized in the study.

Starting with a minimum number of assumptions for the initially unknown parameters and profile distributions, convergent solutions to the full stagnation line equations are rapidly obtained by a method of successive approximations. No singularities exist in this formulation of the finite difference equations. Damping of selected profiles is required to aid convergence of the massive blowing cases; however, even for these cases, no patching of the viscous and inviscid regions is required. The results demonstrate that windward differencing of the convective term in the elemental diffusion equation is required for a stable solution to this equation. While the central difference approximation to the energy equation yields satisfactory solutions when radiation is included, the results are considerably improved for blowing rate of 0.2 when the convective term is windward differenced in this equation also.

Comparisons are made with currently existing solutions to the radiating shock layer problem. The present method predicts lower

wall radiative heat fluxes for carbon phenolic ablation than those predicted by previous investigators.

The results indicate that the ablation products are highly effective in blocking the incident radiation from the high-temperature outer layer of the shock. For blowing rates of 0.1 and 0.2, typical reductions range from about 35 to 40 percent of the non-blowing radiative heat fluxes at the wall.

The inner air layer is shown to be relatively ineffective in blocking the incident radiation, hence the thermodynamic properties need not be as well defined for air injection as for ablation product injection.

The binary diffusion model assumption was examined in the present analysis and, while a multicomponent diffusion study may remain meaningful for conditions and ablators other than those examined in the present study, the results indicate that the multicomponent diffusion model is not required.

The present results are sufficiently encouraging to recommend that the present method be extended to radiation calculations in the presence of chemical nonequilibrium. Since the solution to the governing flow equations requires only about 5 percent of the total computational time, with the radiation flux computation comprising the remaining 95 percent of the time, the implicit finite difference scheme should be relatively efficient for performing the computations.

Table 1. Diffusion coefficient
molecular constants

Molecular constants			
Species	$\epsilon/k, ^\circ K$	$\sigma, \text{\AA}$	$M, \text{gm/gm mole}$
C	30.6	3.385	12.01
N	71.4	3.298	14.01
H	37.0	2.708	1.008

Table 2. Summary of radiative heat fluxes at the wall

A. Air Injection

1. $U_{\infty}' = 14.55$ km/sec, $\rho_{\infty}' = 2.377 \times 10^{-7}$ gm/cm³, $p_{\infty}' = 1.6 \times 10^{-4}$ atm,
 $R_b' = 3.427$ m

$(\rho v)_w$	$q_{R,W}'$ (watts/cm ²)		
	Suttles (1969)	Falanga and Sullivan	Present Analysis
0	-2860	-3000	-2950

2. $U_{\infty}' = 15.25$ km/sec, $\rho_{\infty}' = 2.72 \times 10^{-7}$ gm/cm³, $p_{\infty}' = 1.95 \times 10^{-4}$ atm,
 $R_b' = 3.048$ m

$(\rho v)_w$	$q_{R,W}'$ (watts/cm ²)			
	Rigdon <u>et al.</u> (1969)	Smith <u>et al.</u> (1970)	Wilson (1970)	Present analysis
0	-5990	-4170	---	-4150
-0.1	-5130	-3991*	-3660*	-3740
-0.2	-4630	---	---	-3490

B. Carbon Phenolic Injection

1. $U_{\infty}' = 15.25$ km/sec, $\rho_{\infty}' = 1.77 \times 10^{-7}$ gm/cm³, $p_{\infty}' = 1.21 \times 10^{-4}$ atm,
 $R_b' = 2.56$ m

$(\rho v)_w$	$q_{R,W}'$ (watts/cm ²)		
	Chin	Smith <u>et al.</u> (1970)	Present analysis
0	-3030	-2795	-2540
-0.076	-1642	-2188	-1620

2. $U_{\infty}' = 15.25$ km/sec, $\rho_{\infty}' = 2.72 \times 10^{-7}$ gm/cm³, $p_{\infty}' = 1.95 \times 10^{-4}$ atm,
 $R_b' = 3.048$ m

$(\rho v)_w$	$q_{R,W}'$ (watts/cm ²)		
	Rigdon <u>et al.</u> (1969)	Smith <u>et al.</u> (1970)	Present analysis
0	-5990	-4170	-4150
-0.1	---	---	-2790
-0.2	-2670	-3246	-2560

*Private communications.

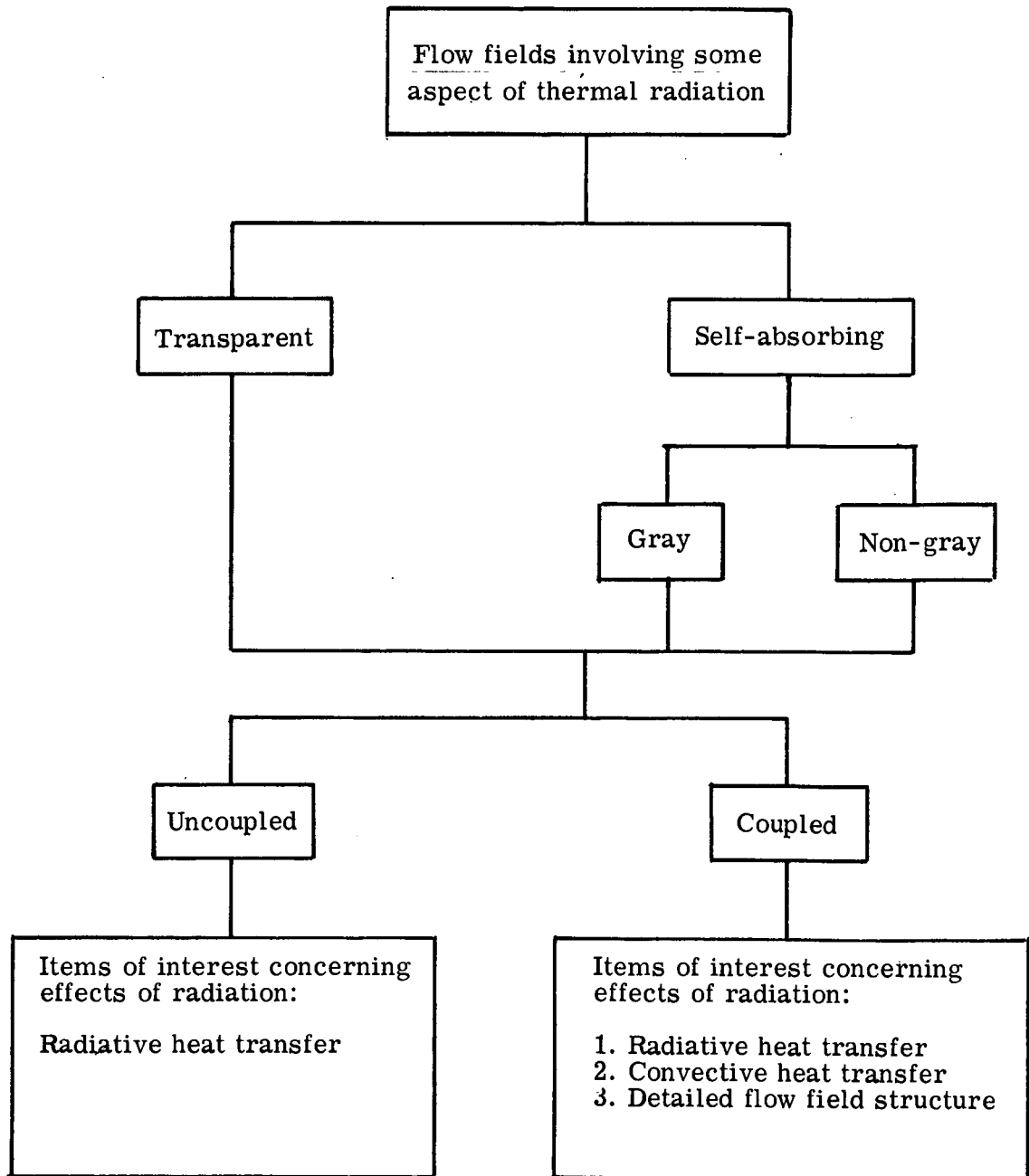


Figure 1. Diagram of various assumptions for the analysis of radiating shock layers (from Anderson, 1968, p. 2)

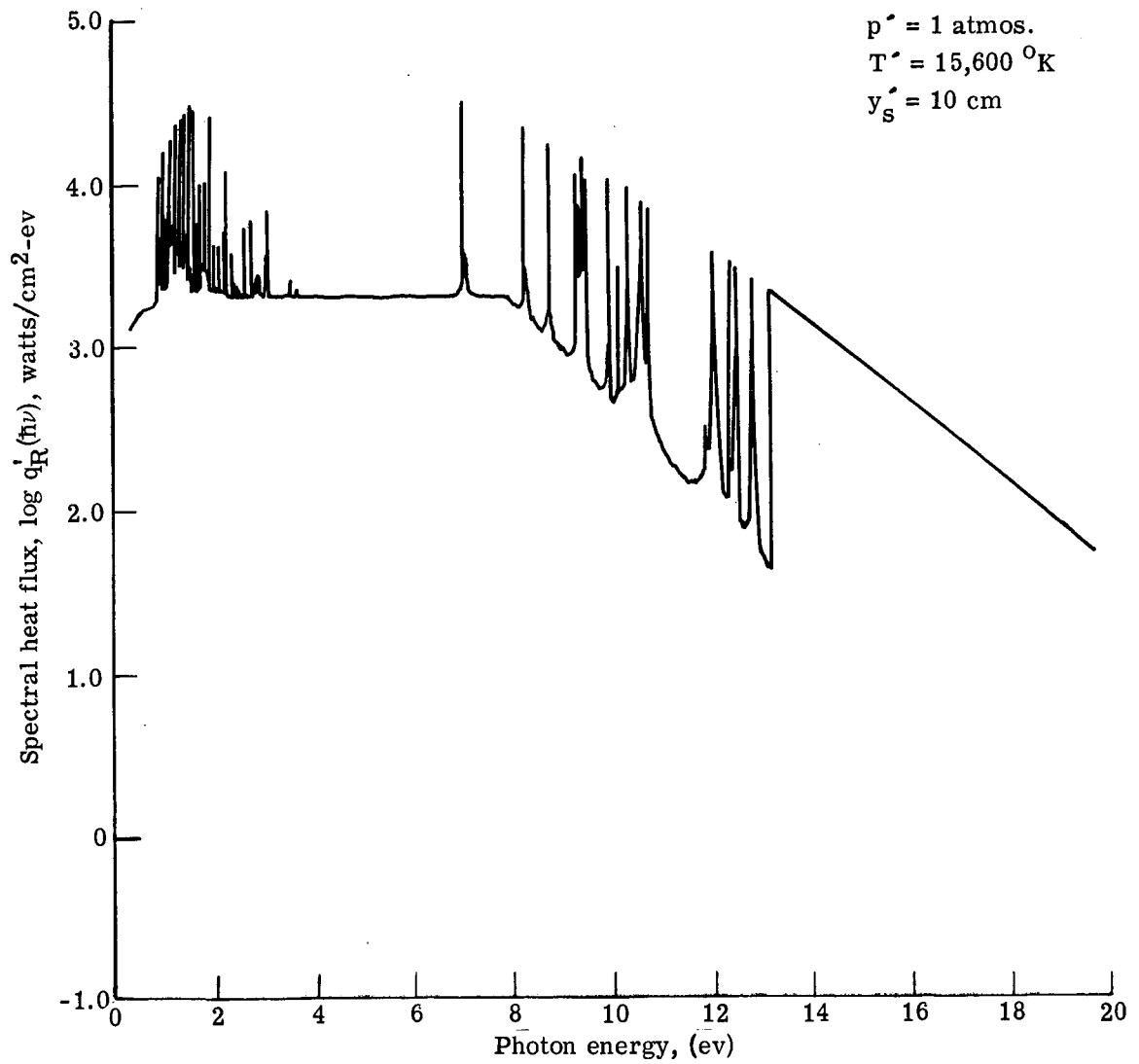


Figure 2. Spectral heat flux distribution for air from SPECS radiation code (Thomas, 1967)

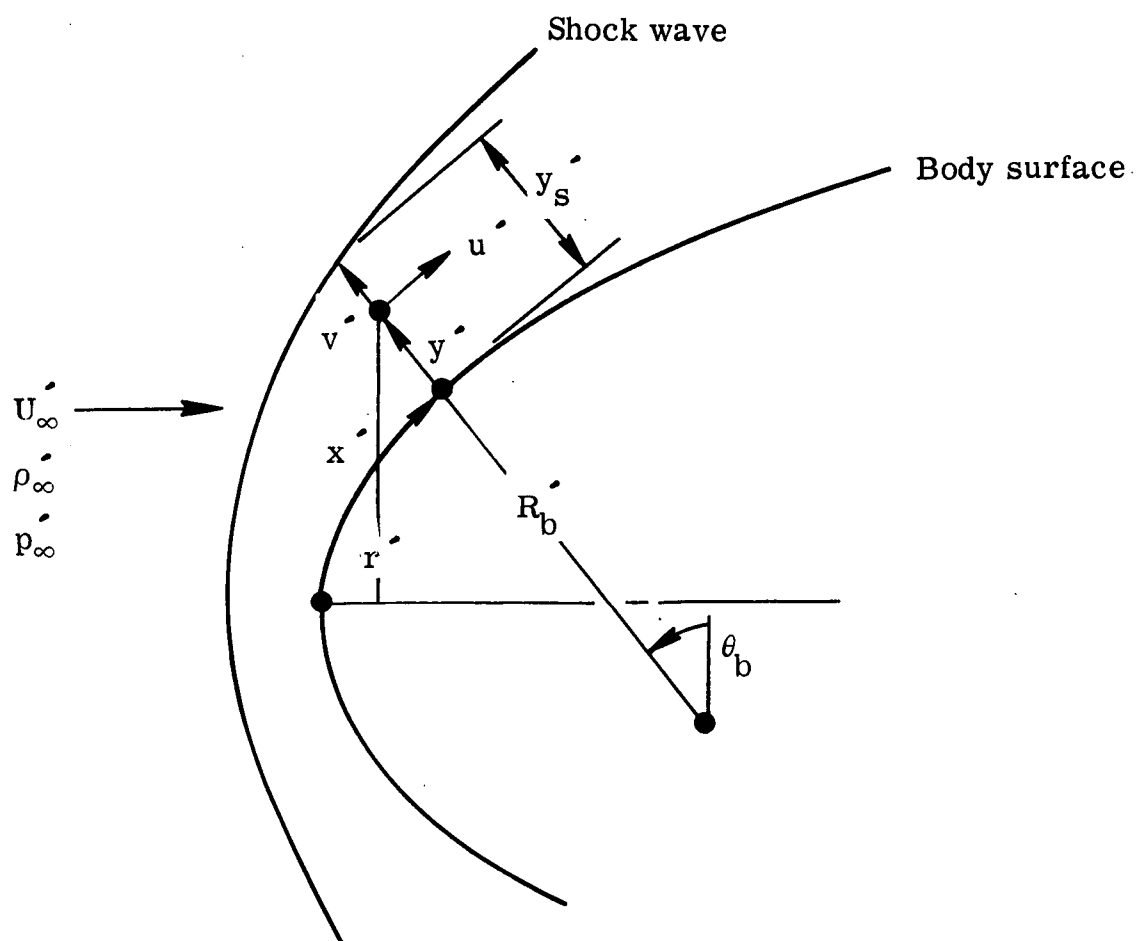


Figure 3. Flow-field coordinate system

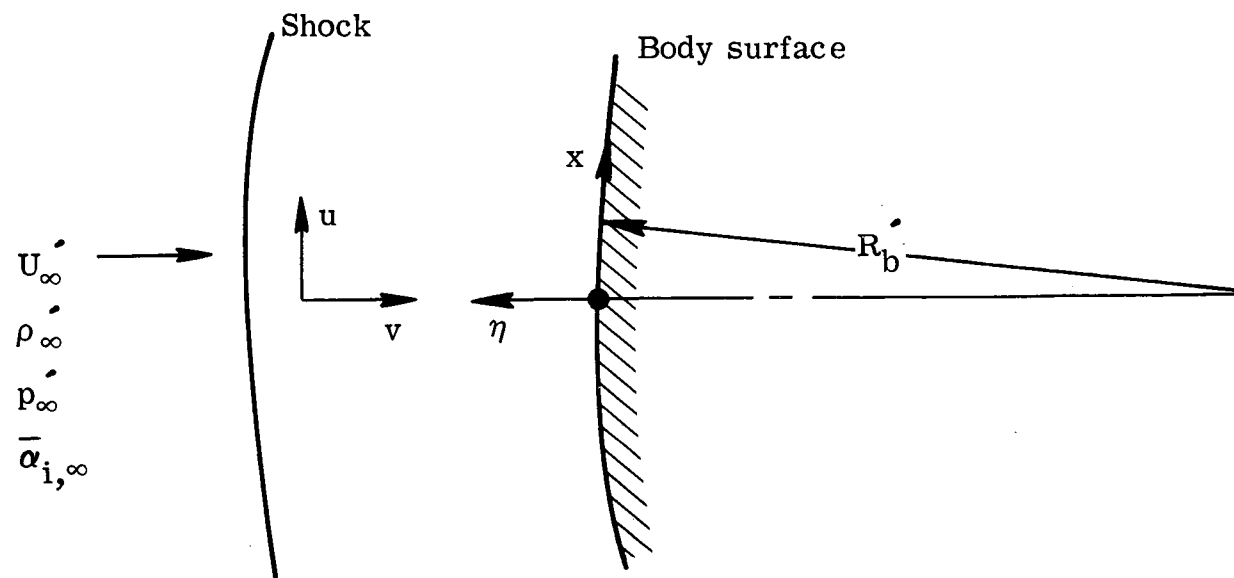
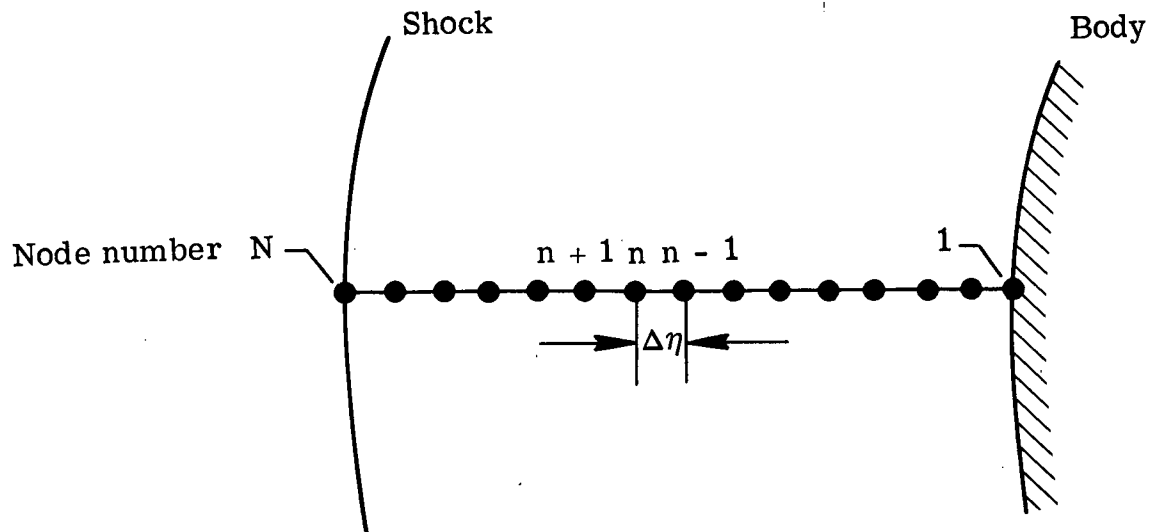


Figure 4. Flow-field coordinate system in the transformed coordinates



- Notes: (1) N must be odd
 (2) Nodal points are equally spaced in η

Figure 5. Finite difference network

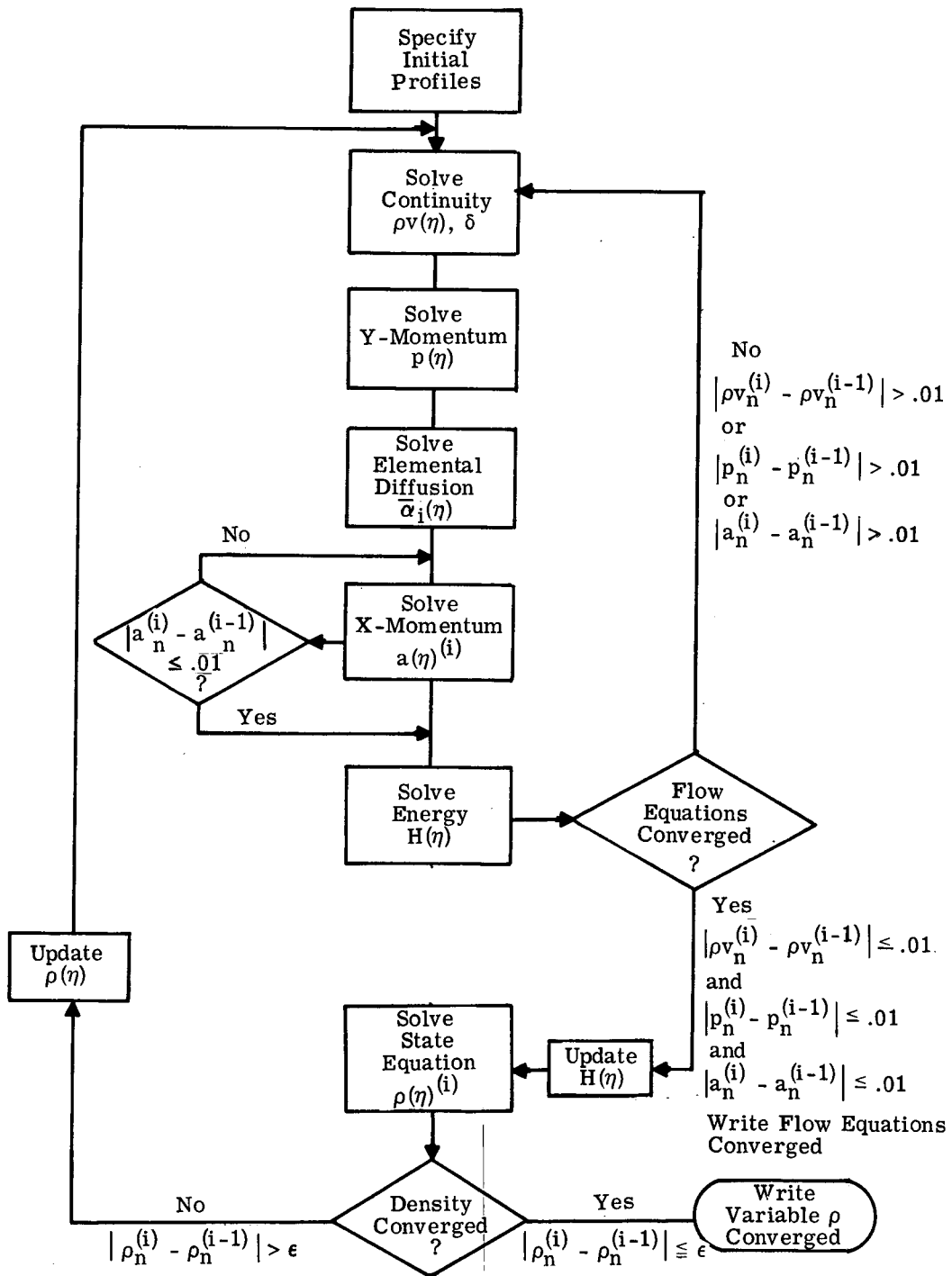


Figure 6. Flow diagram of the overall solution procedure

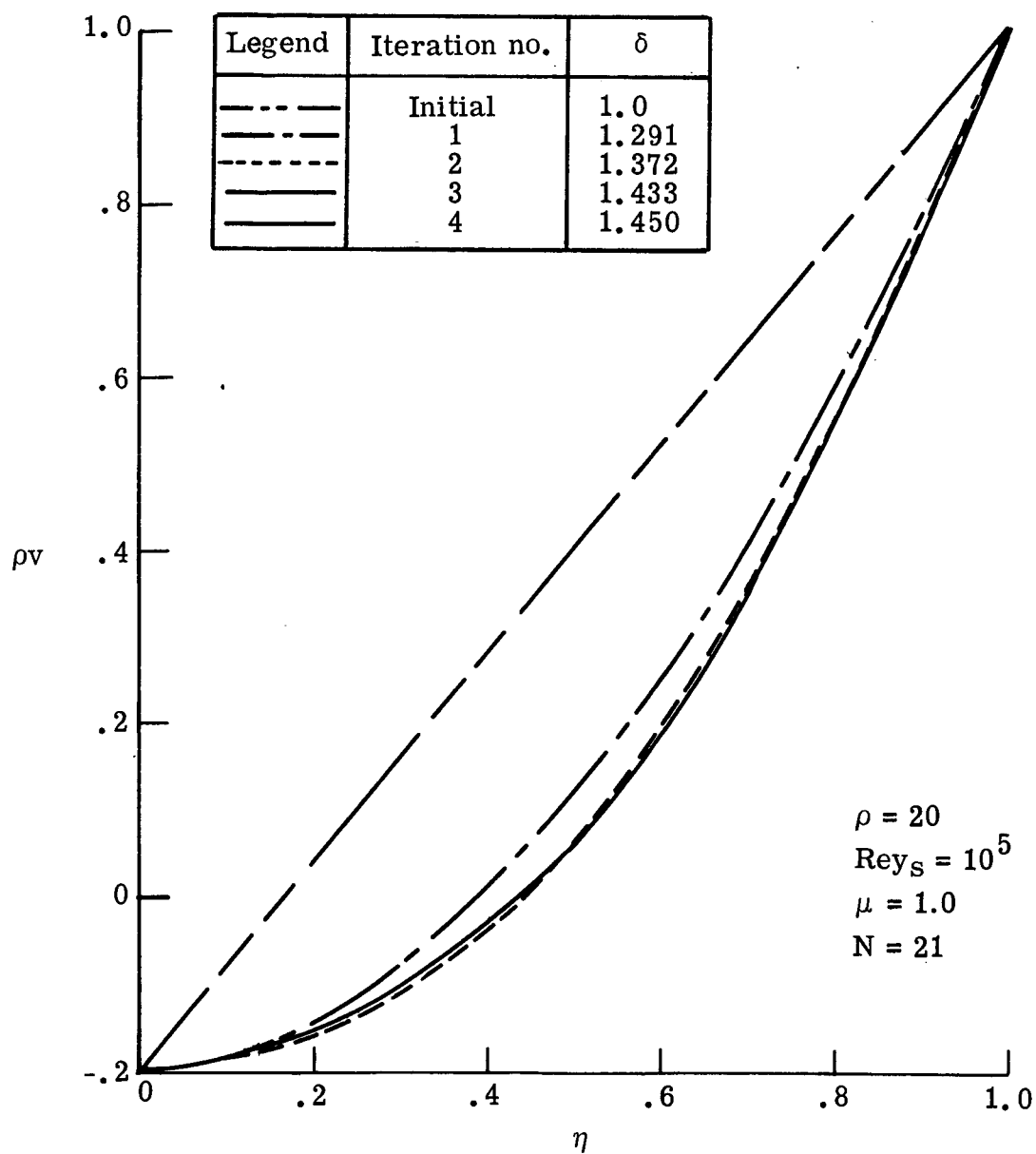
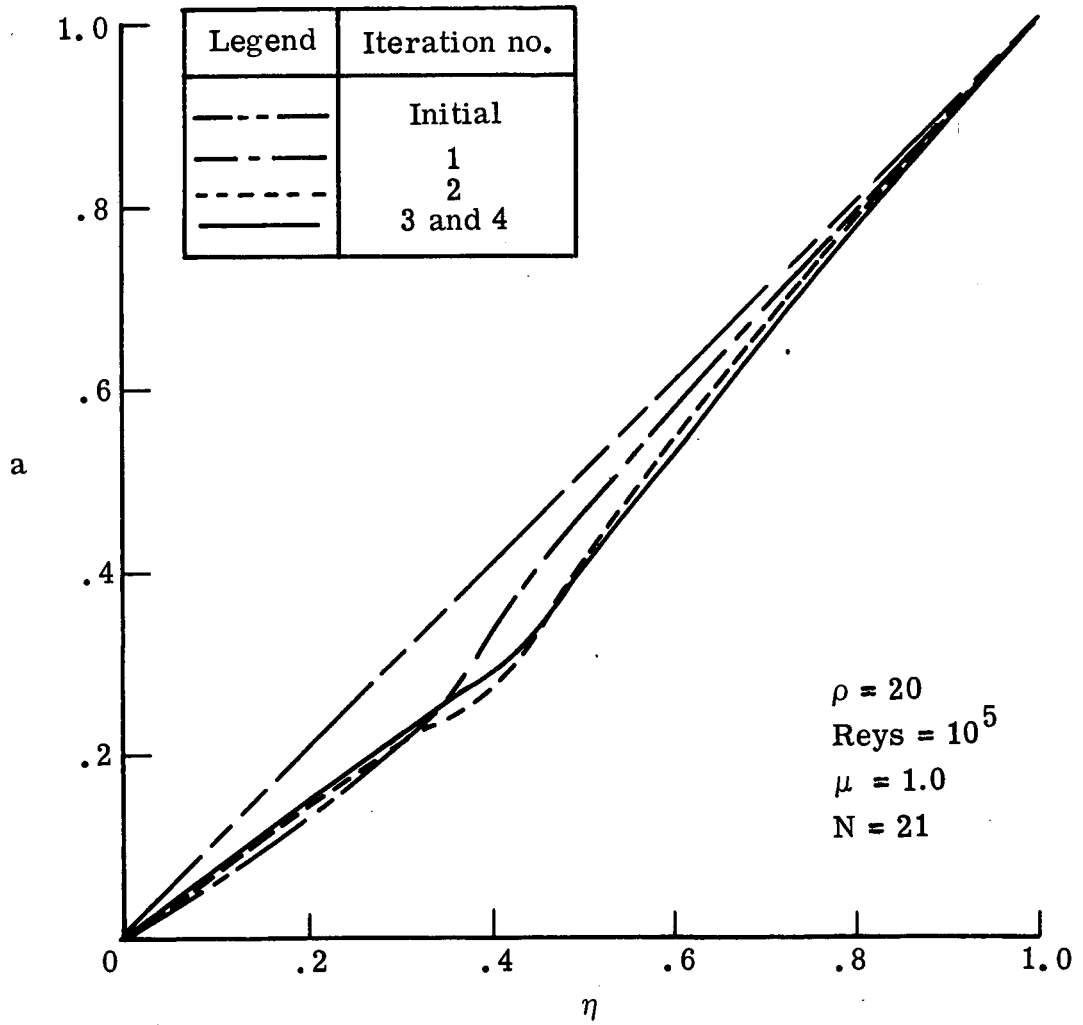
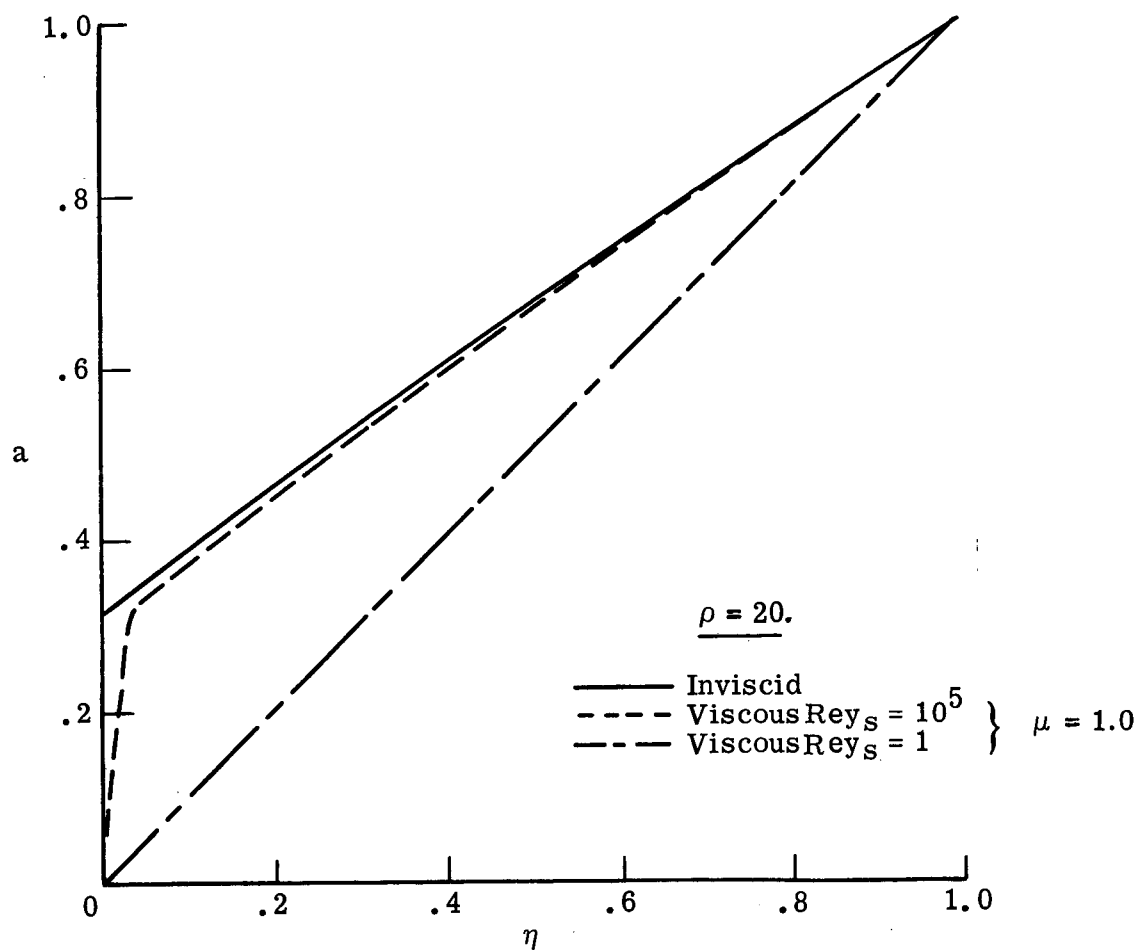
(a) Continuity equation, ρv

Figure 7. Convergence behavior of a typical constant density solution



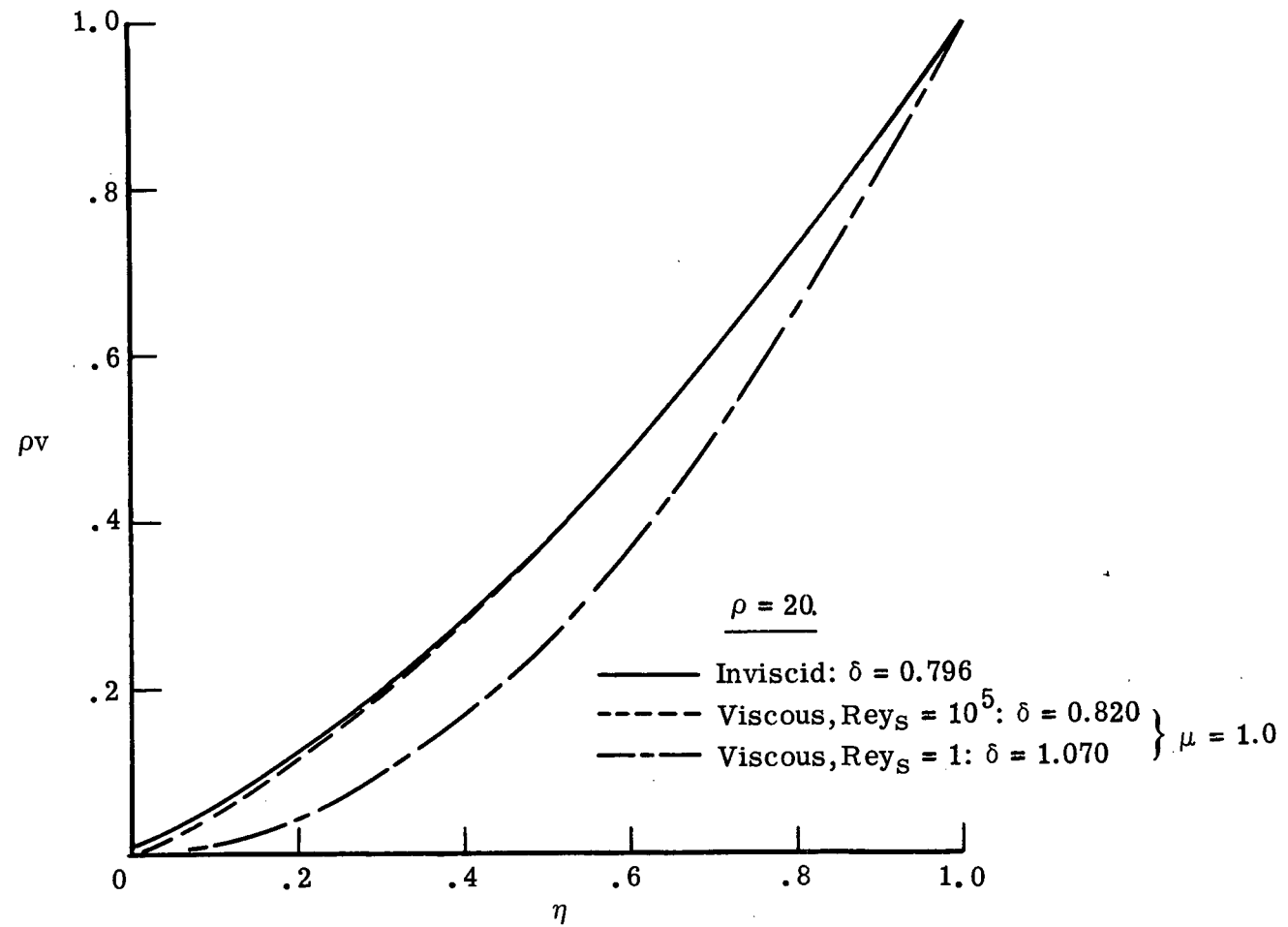
(b) X-momentum equation, a

Figure 7. Concluded



(a) Velocity gradient distributions

Figure 8. Constant density solutions for inviscid and viscous flows without blowing



(b) Mass flux distributions

Figure 8. Concluded

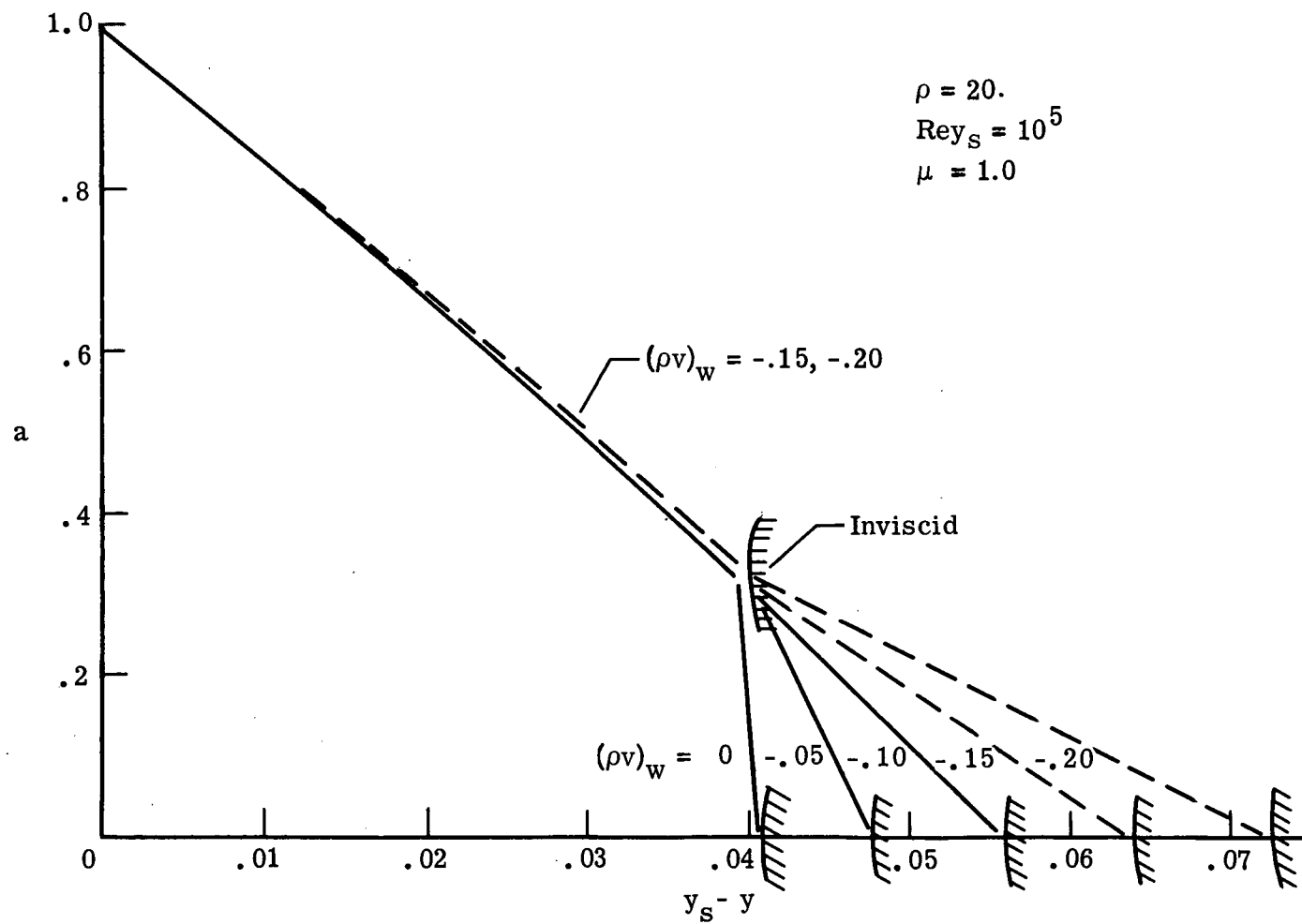


Figure 9. Influence of blowing rate on velocity gradient for the constant density solutions

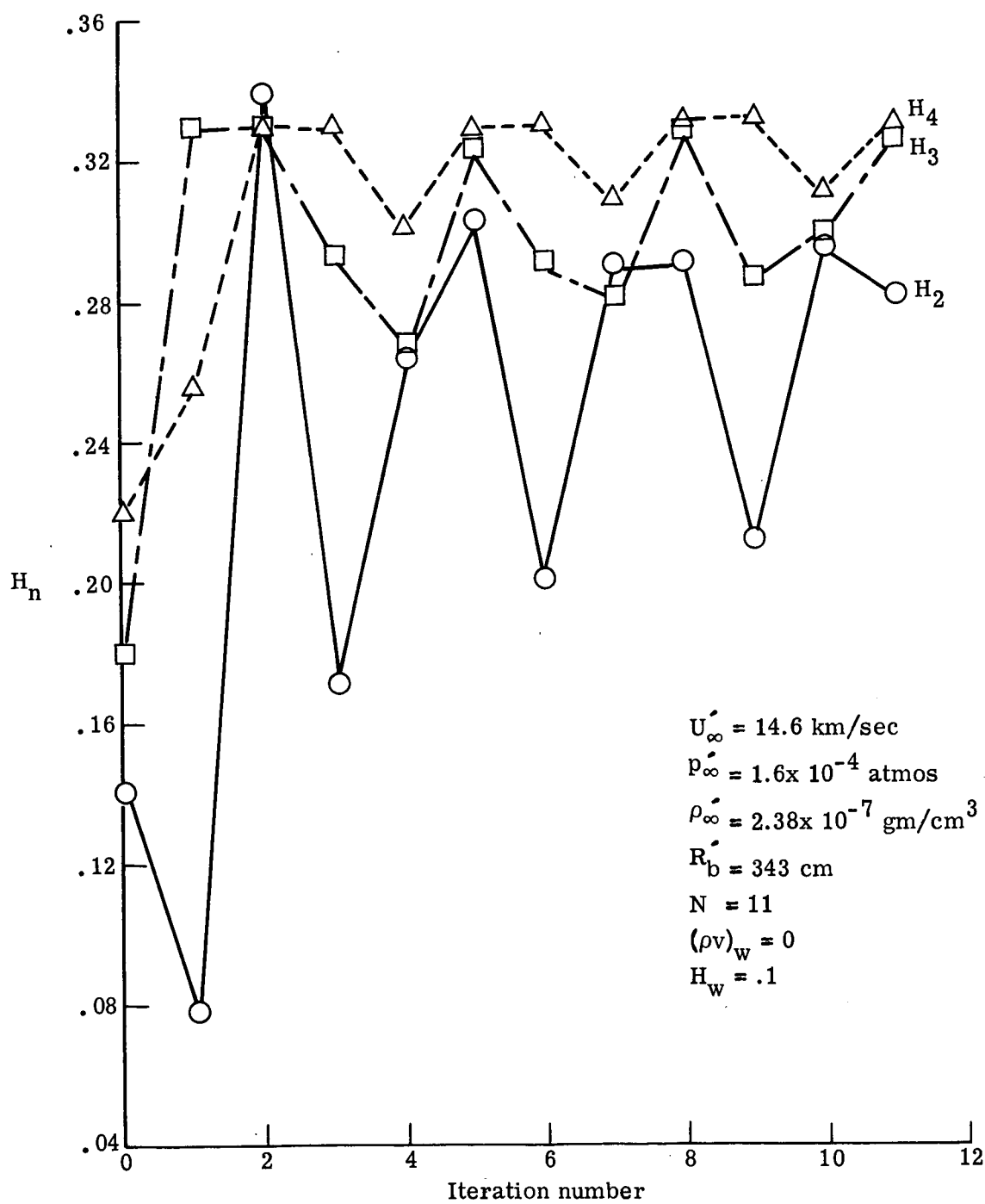
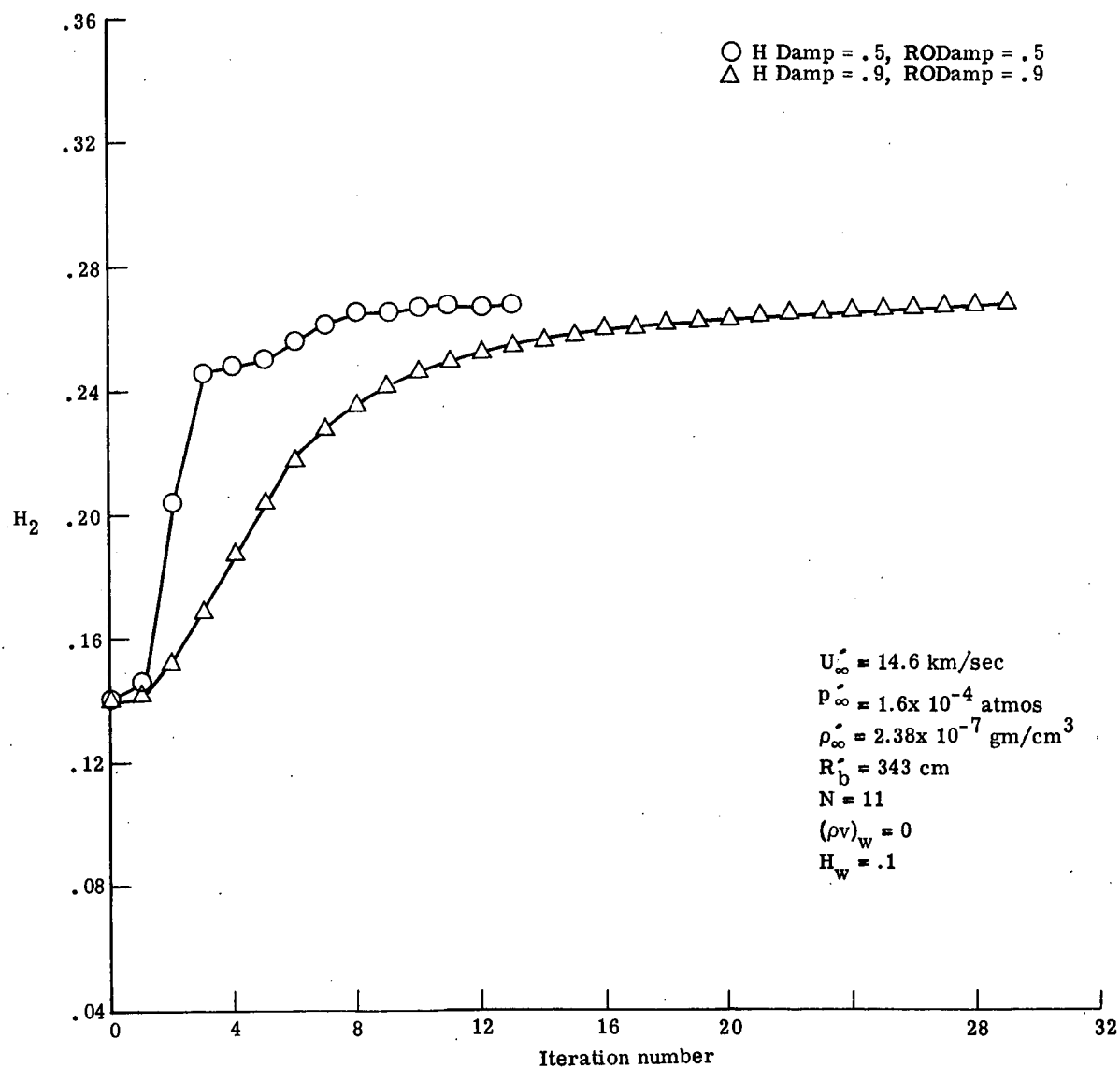
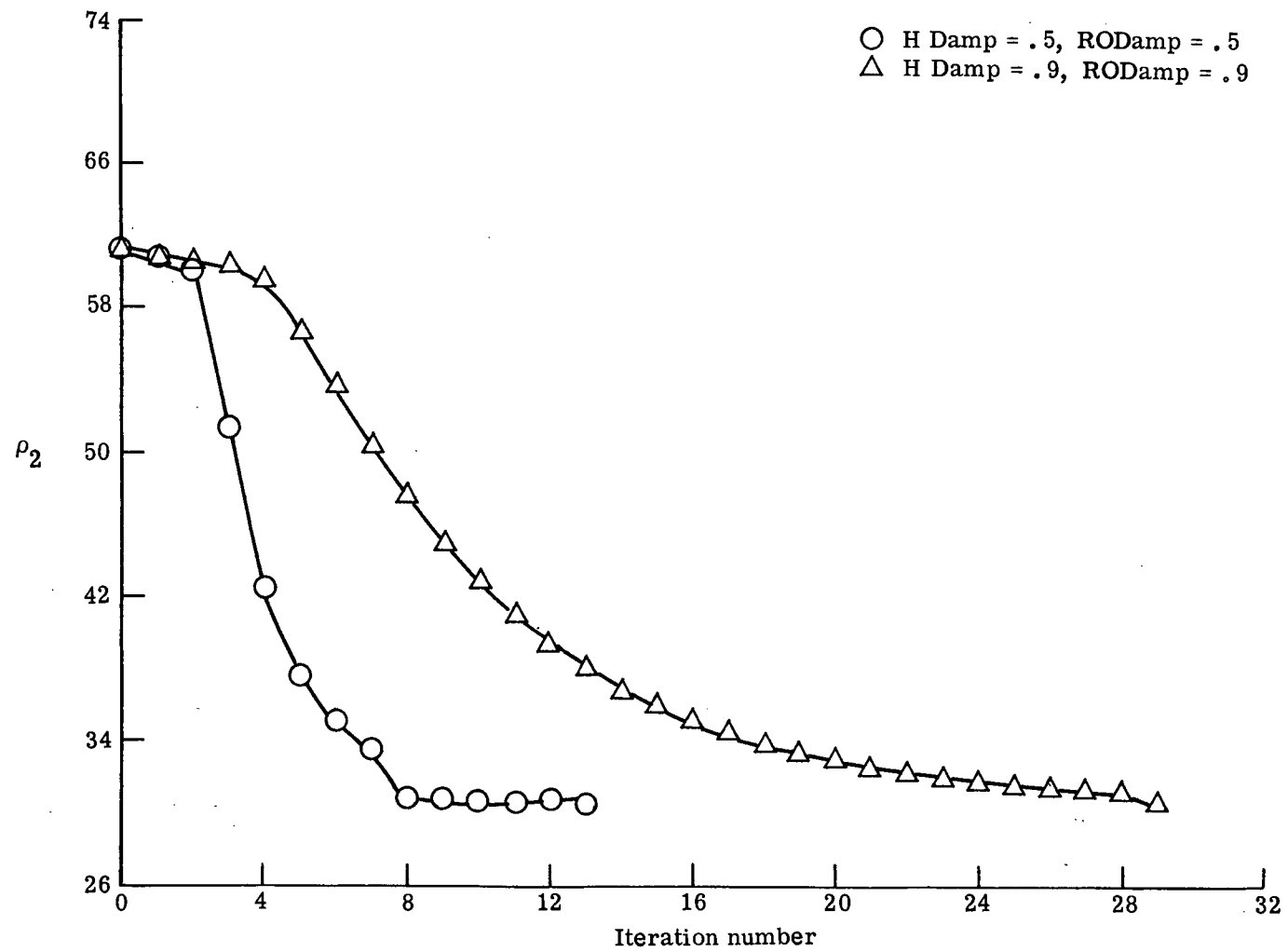


Figure 10. Convergence behavior of the variable density solution - equilibrium air without radiation



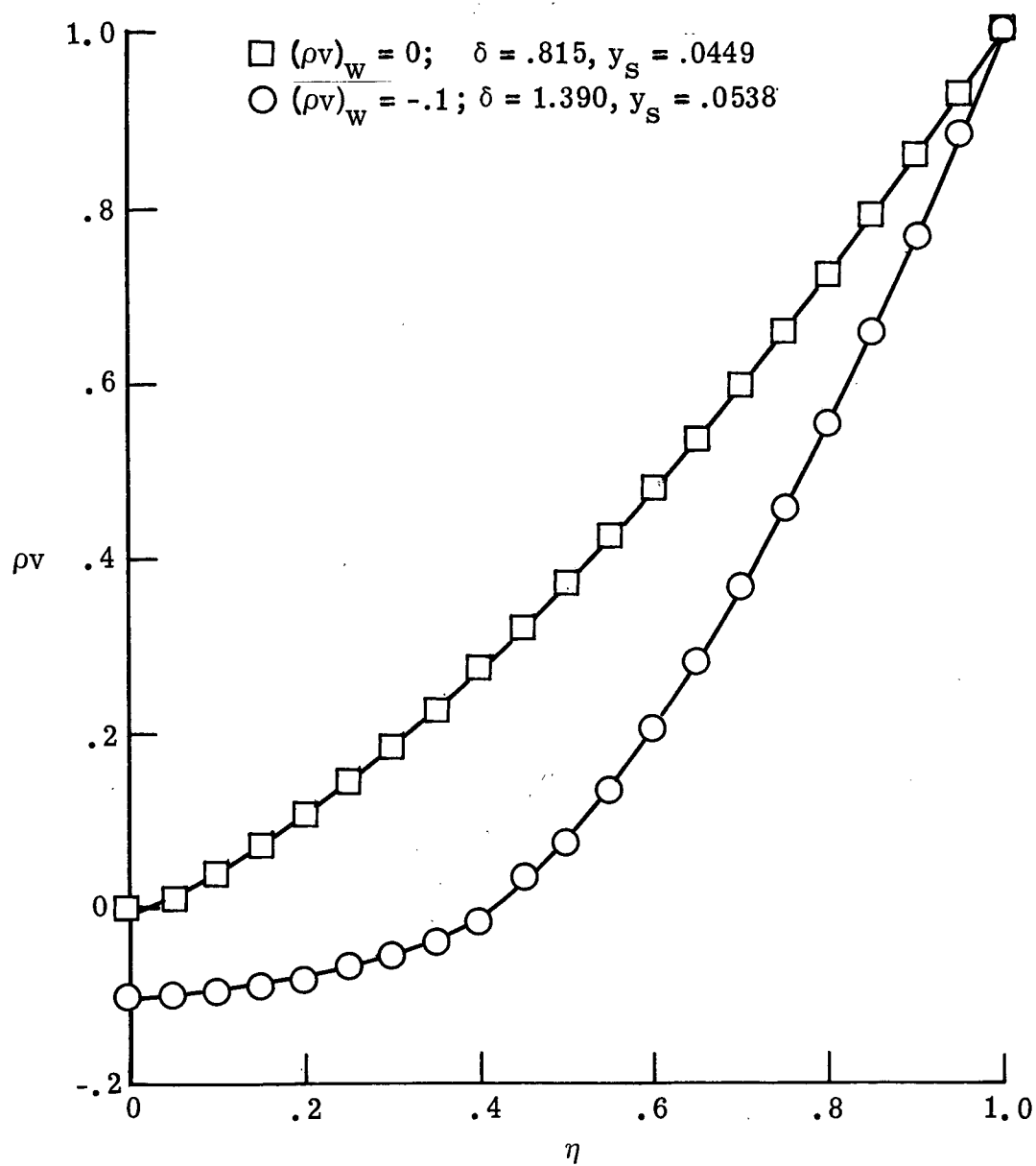
(a.) Enthalpy

Figure 11. Effect of profile damping on the convergence of the variable density solution (equilibrium air without radiation)



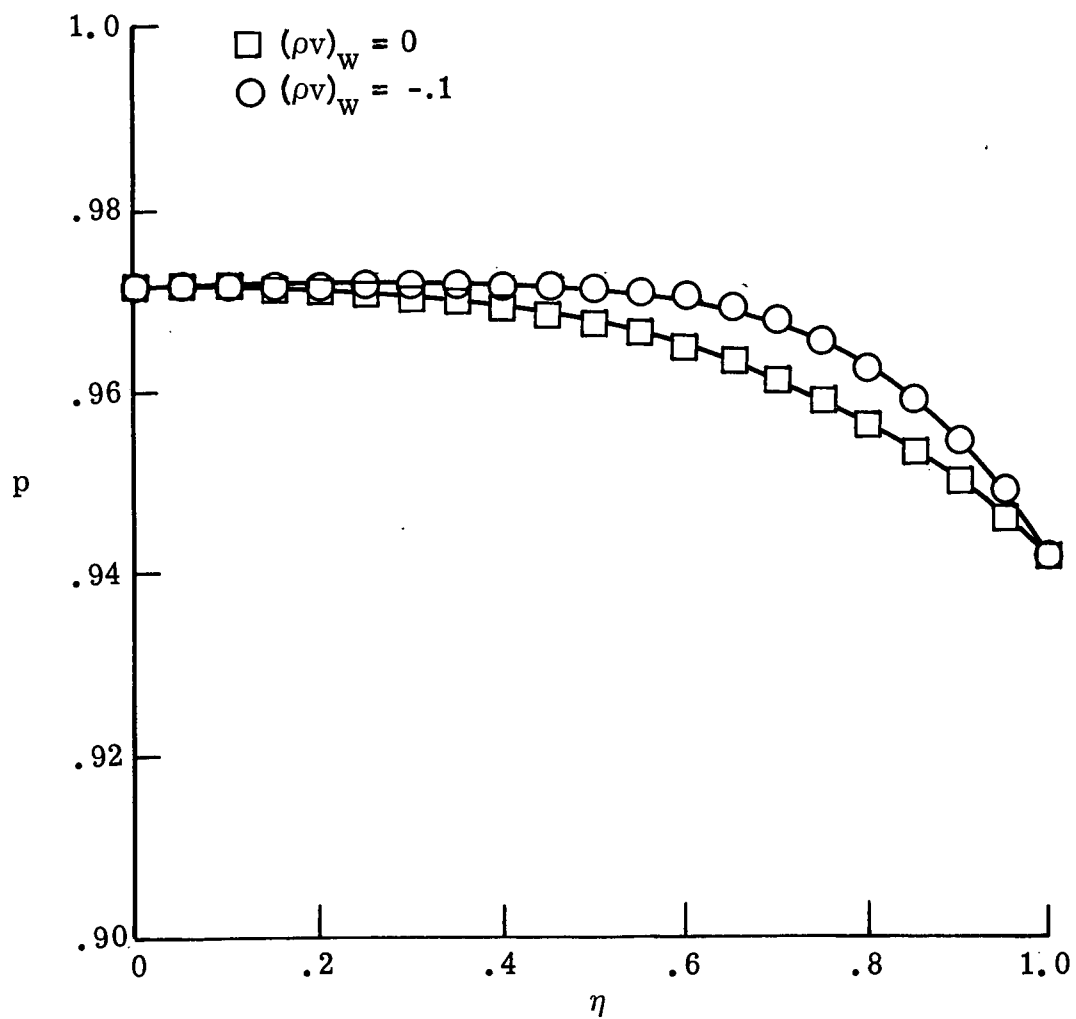
(b) Density

Figure 11. Concluded



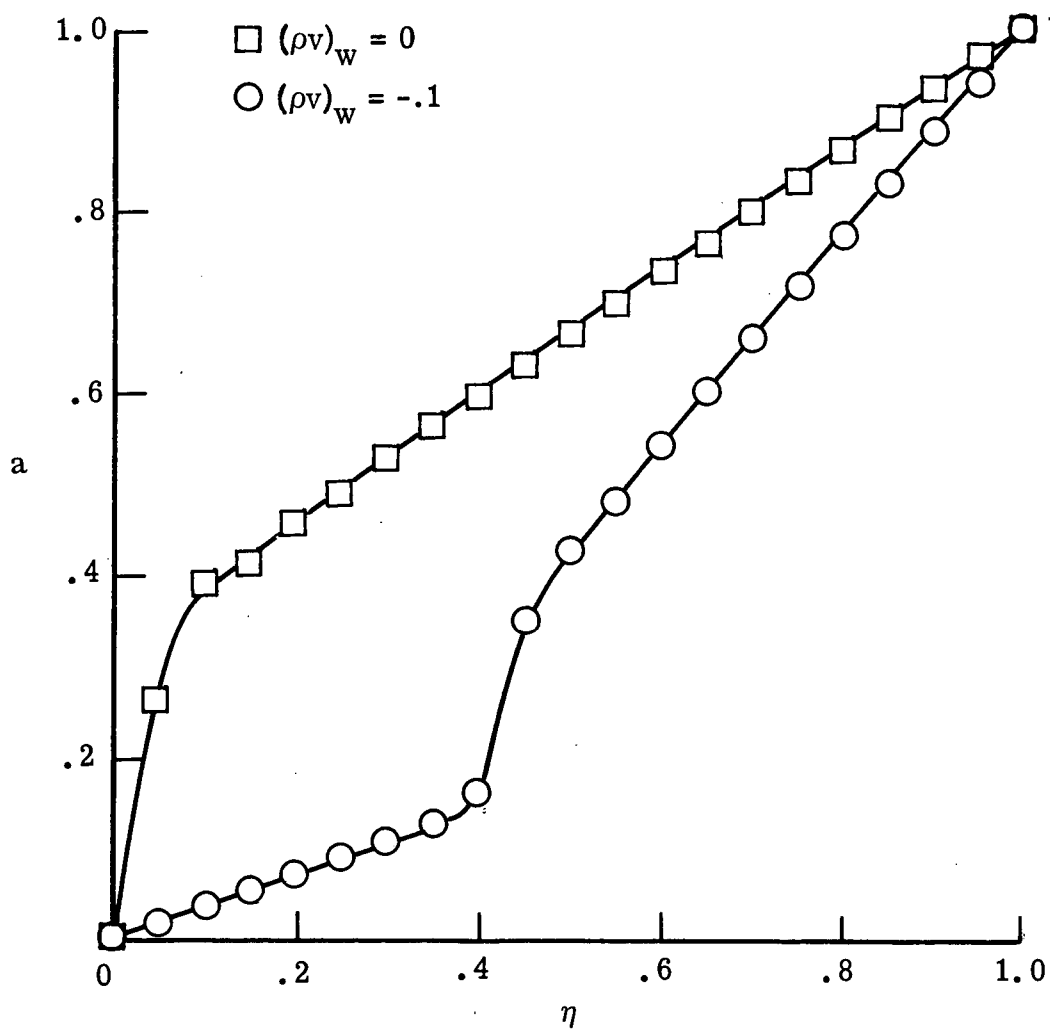
(a) Continuity equation

Figure 12. Equilibrium air solutions without radiation



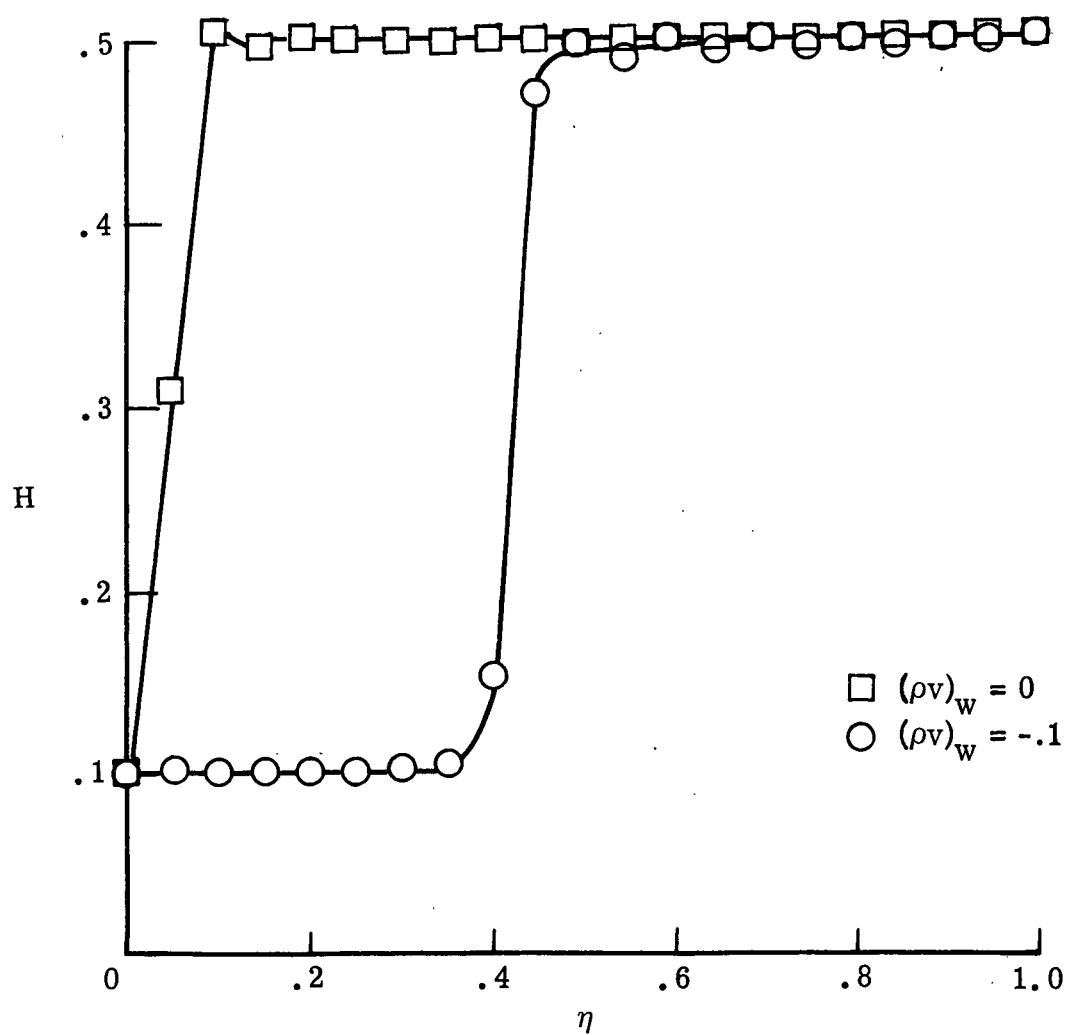
(b) Y-momentum equation

Figure 12. Continued



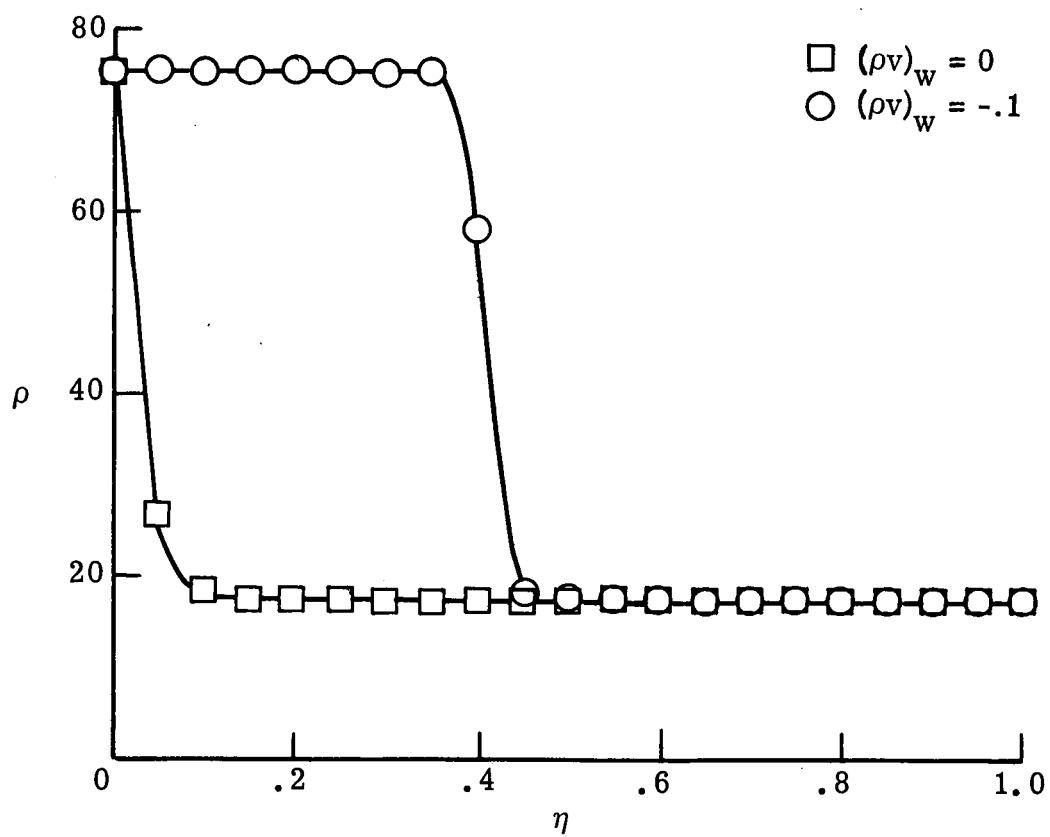
(c) X-momentum equation

Figure 12. Continued



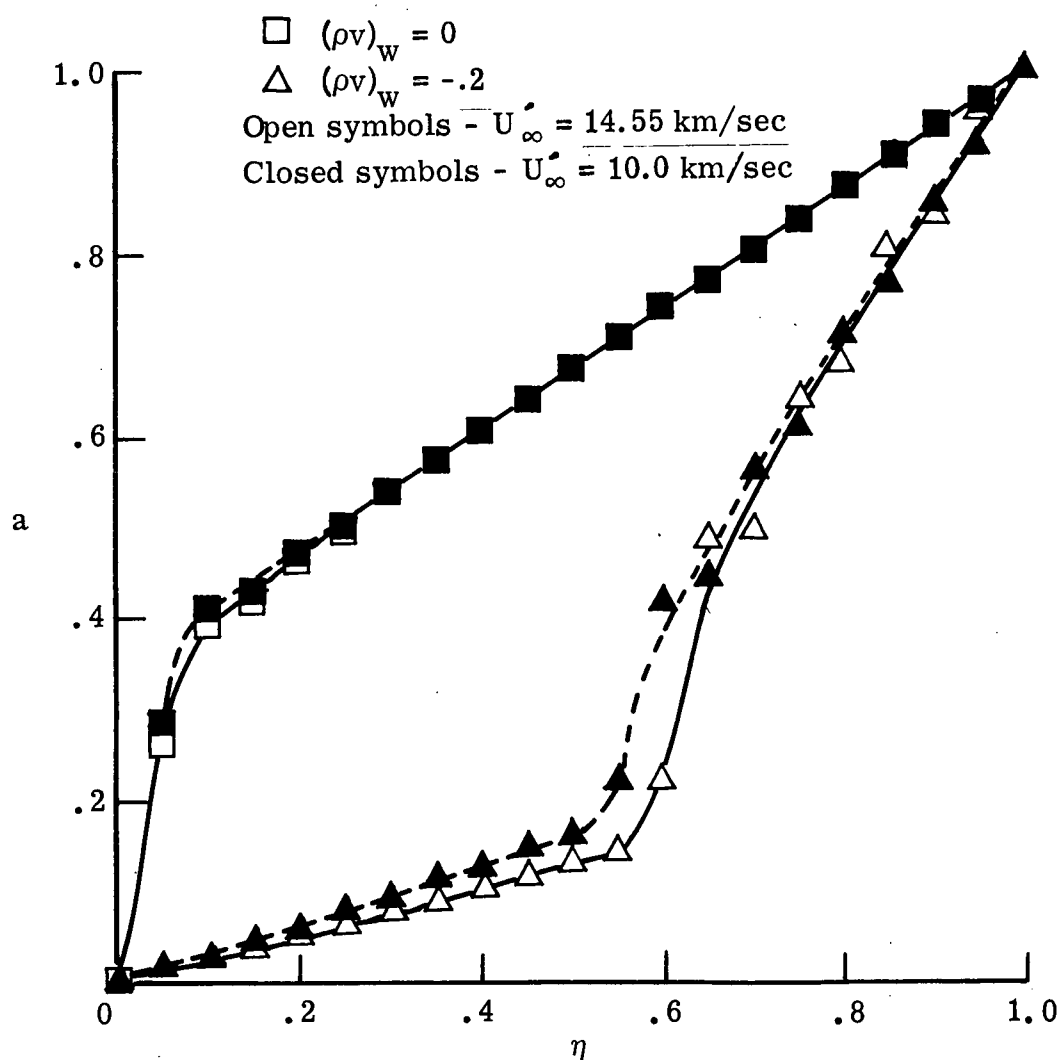
(d) Energy equation

Figure 12. Continued



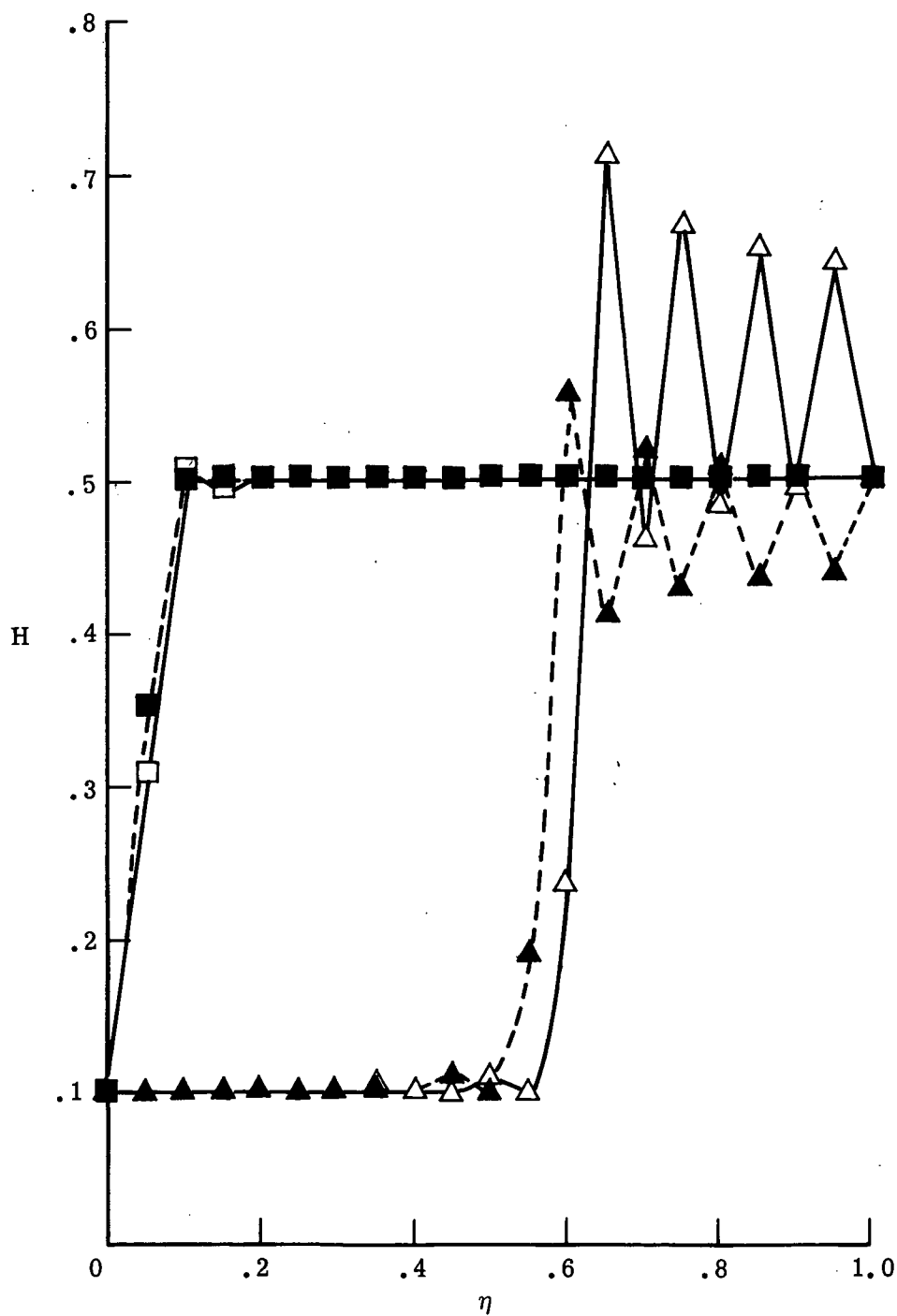
(e) Equation of state

Figure 12. Concluded



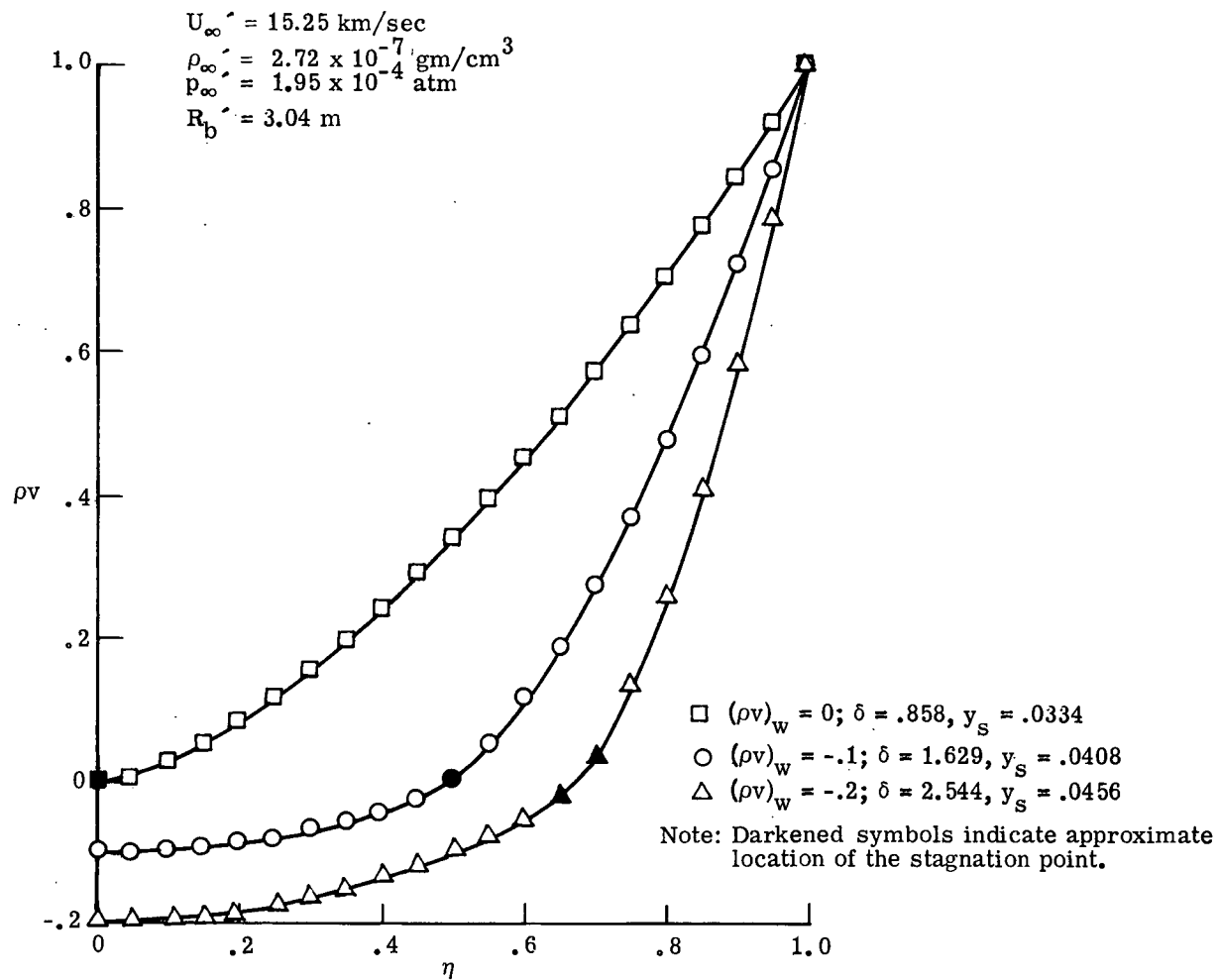
(a) X-momentum equation solution

Figure 13. Comparisons of the solutions in velocity regions where radiation fluxes are and are not significant



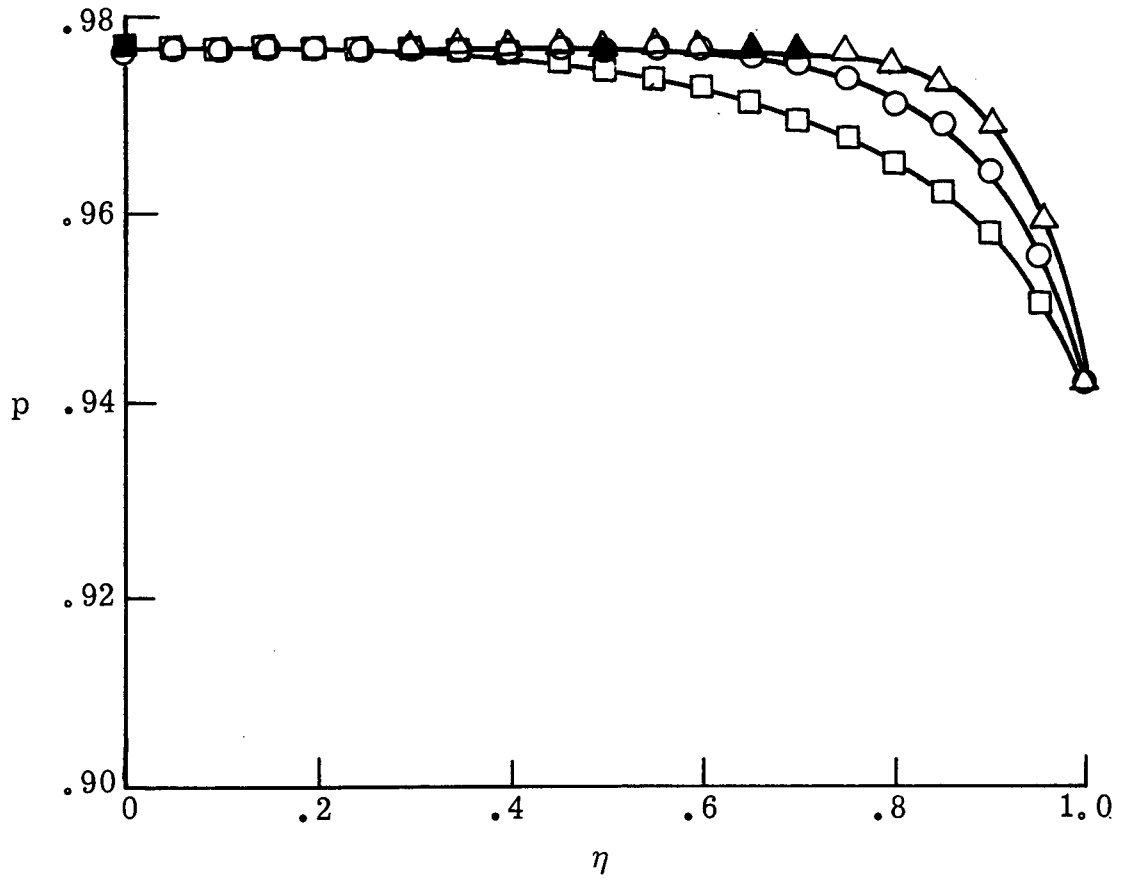
(b) Energy equation solution

Figure 13. Concluded



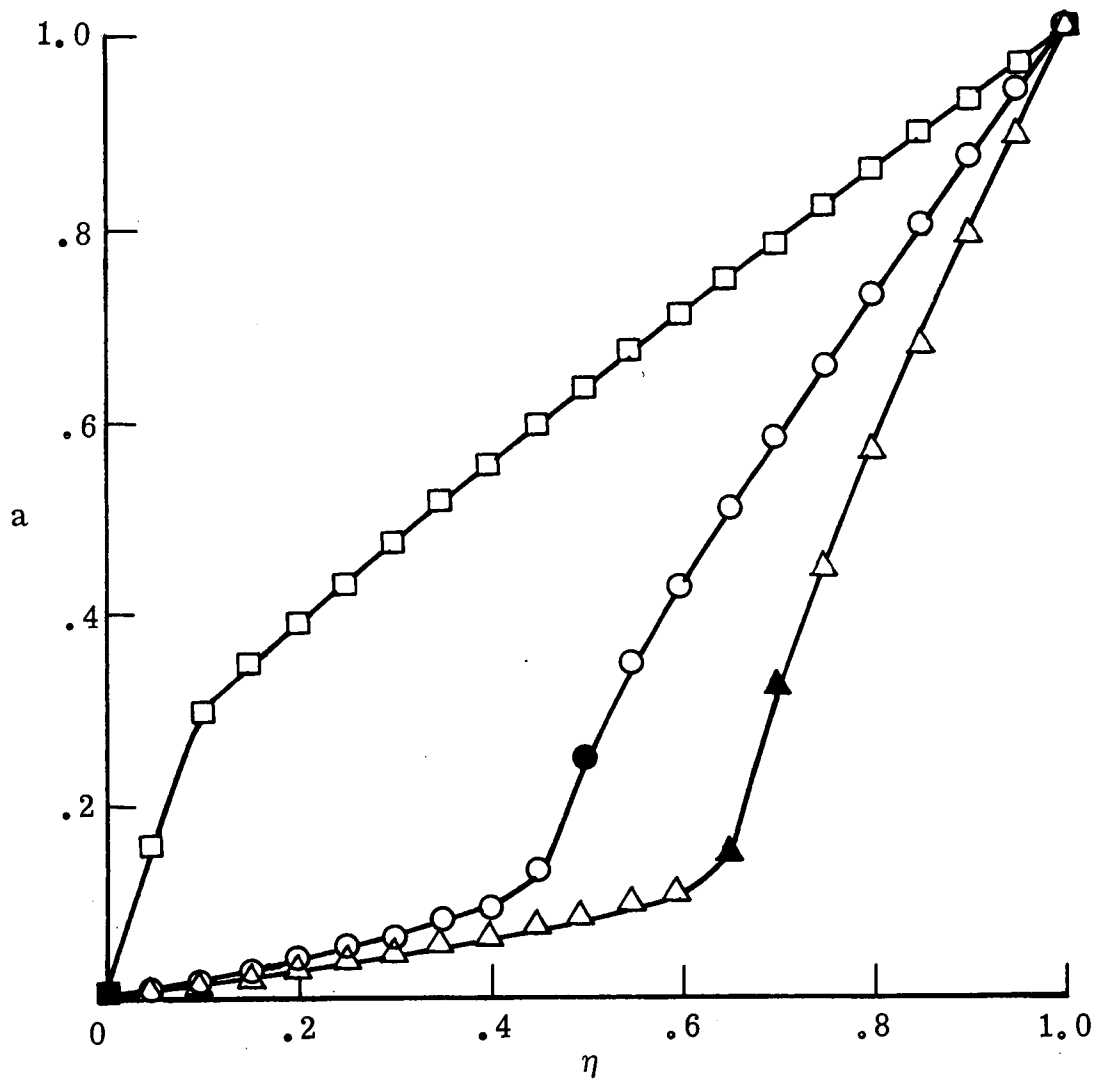
(a) Continuity equation

Figure 14. Equilibrium air solutions with radiation included



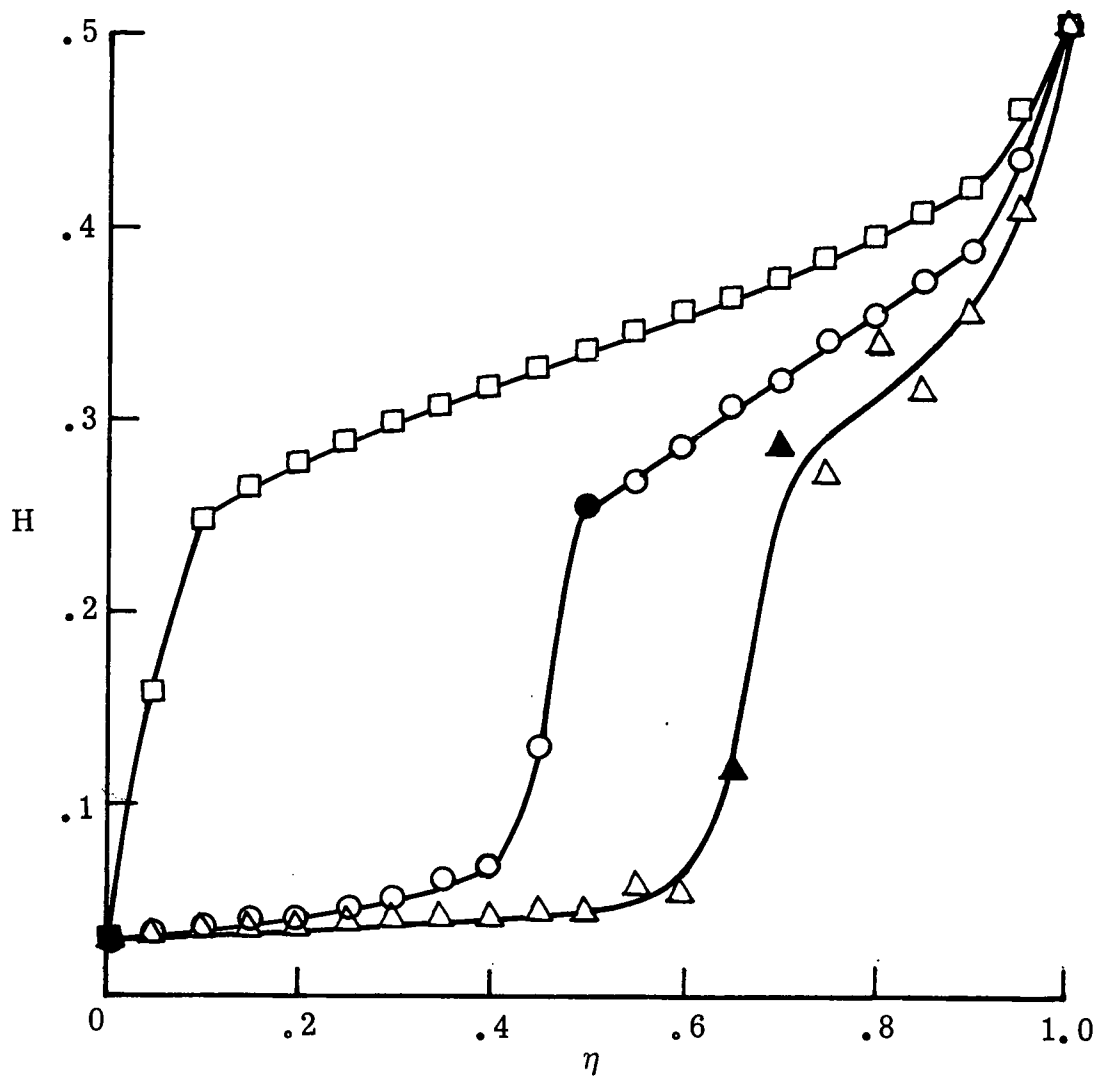
(b) Y-momentum equation

Figure 14. Continued



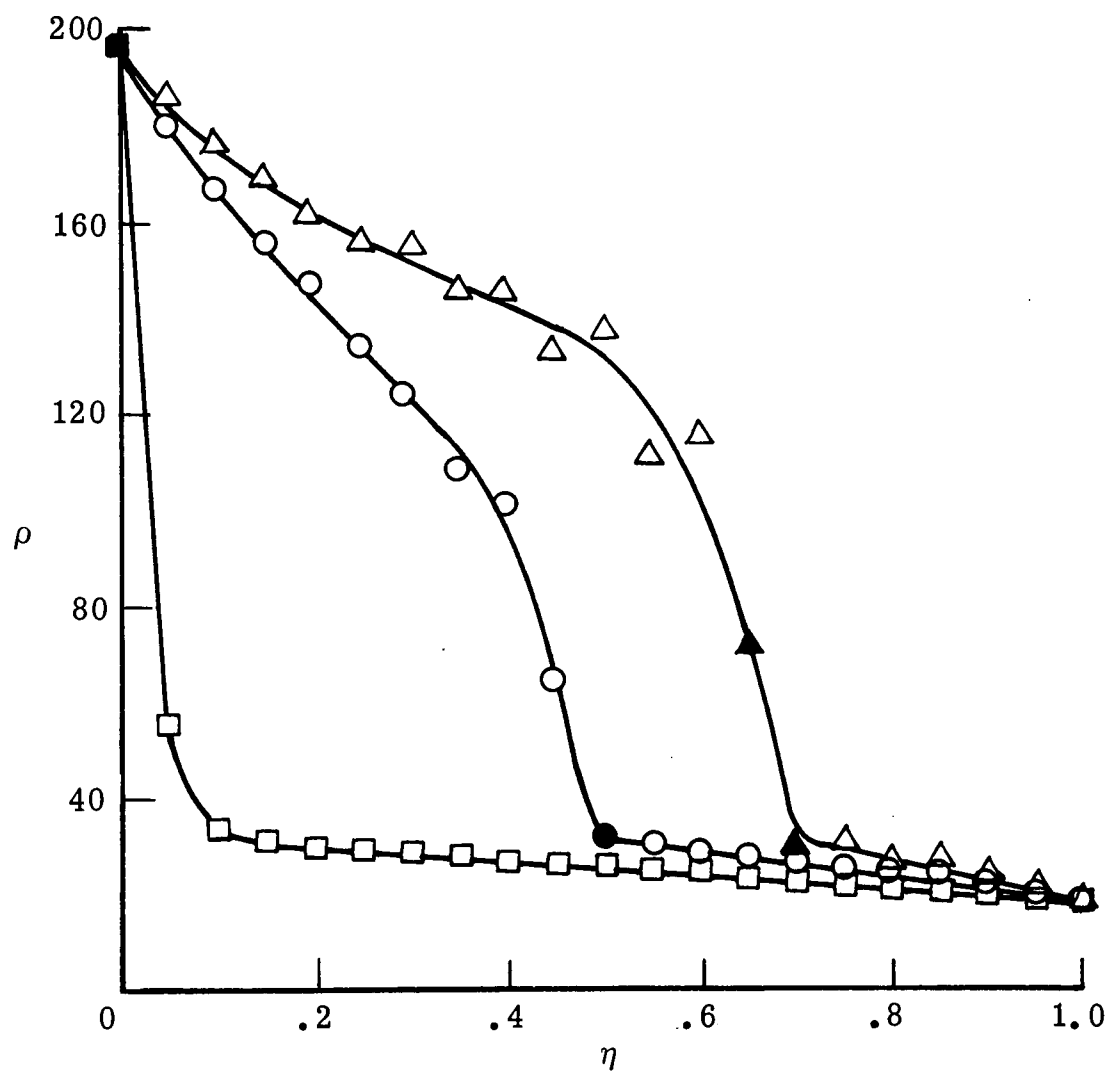
(c) X-momentum equation

Figure 14. Continued



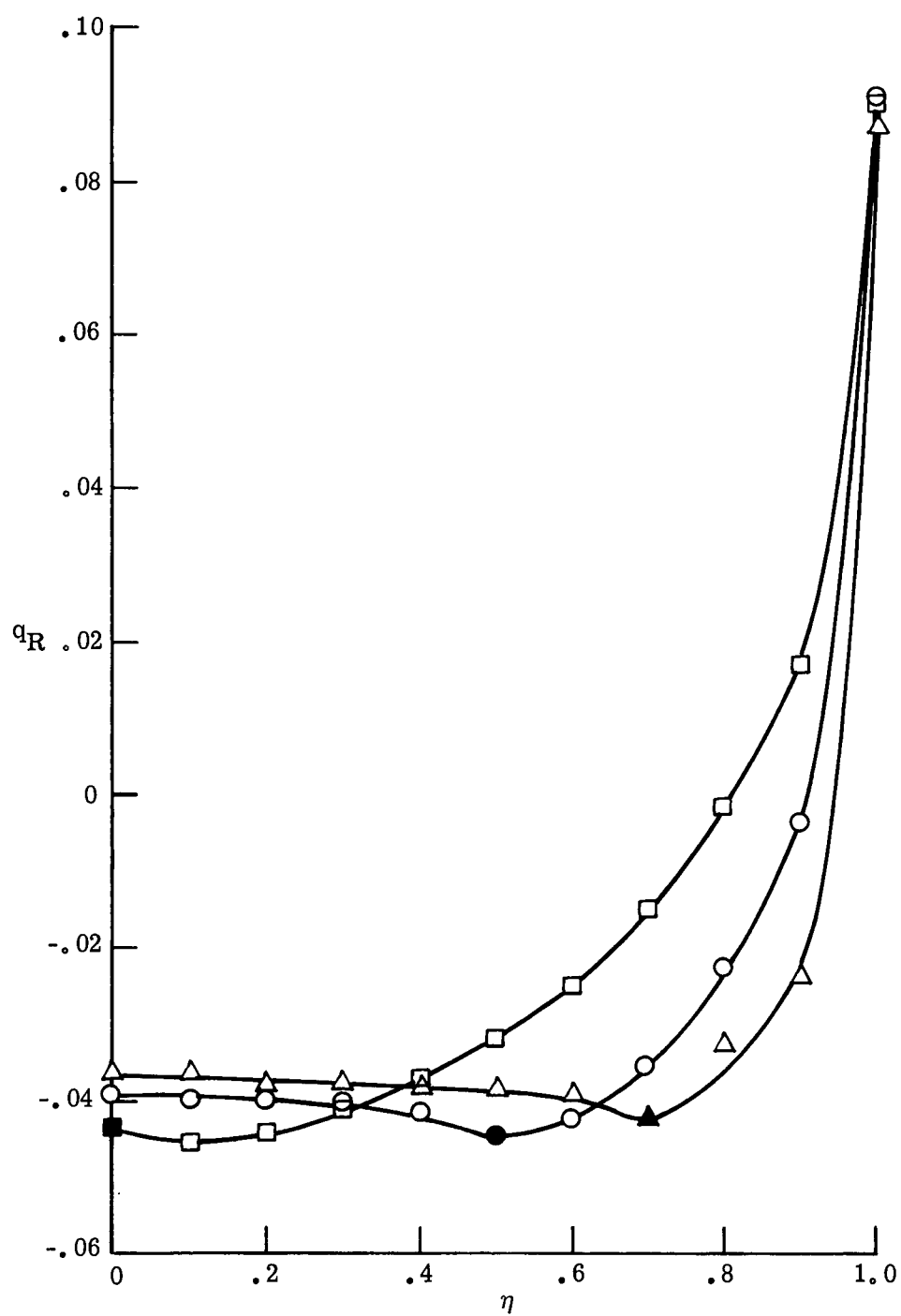
(d) Energy equation

Figure 14. Continued



(e) Equation of state

Figure 14. Continued



(f) Radiative heat flux

Figure 14. Concluded

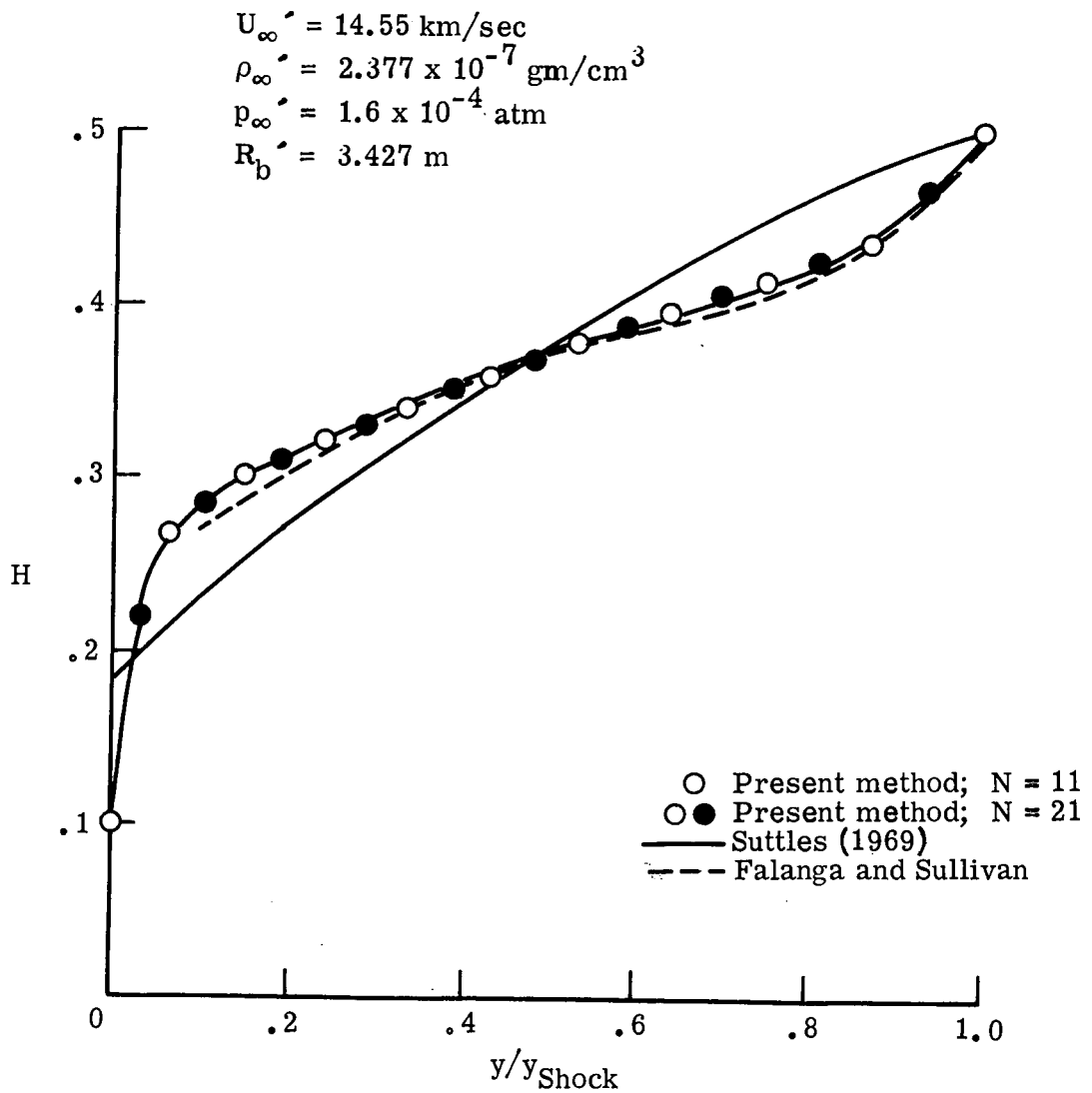
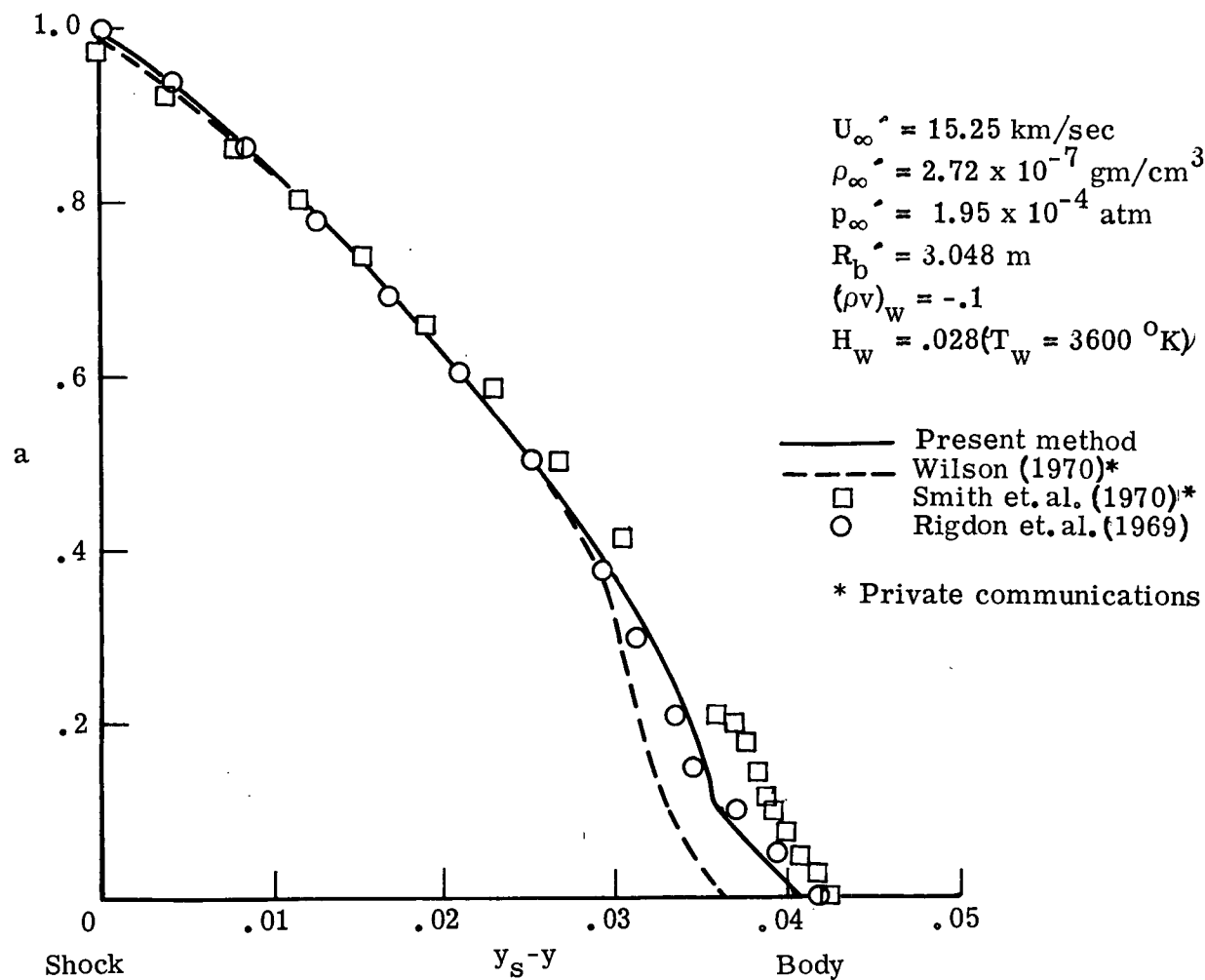
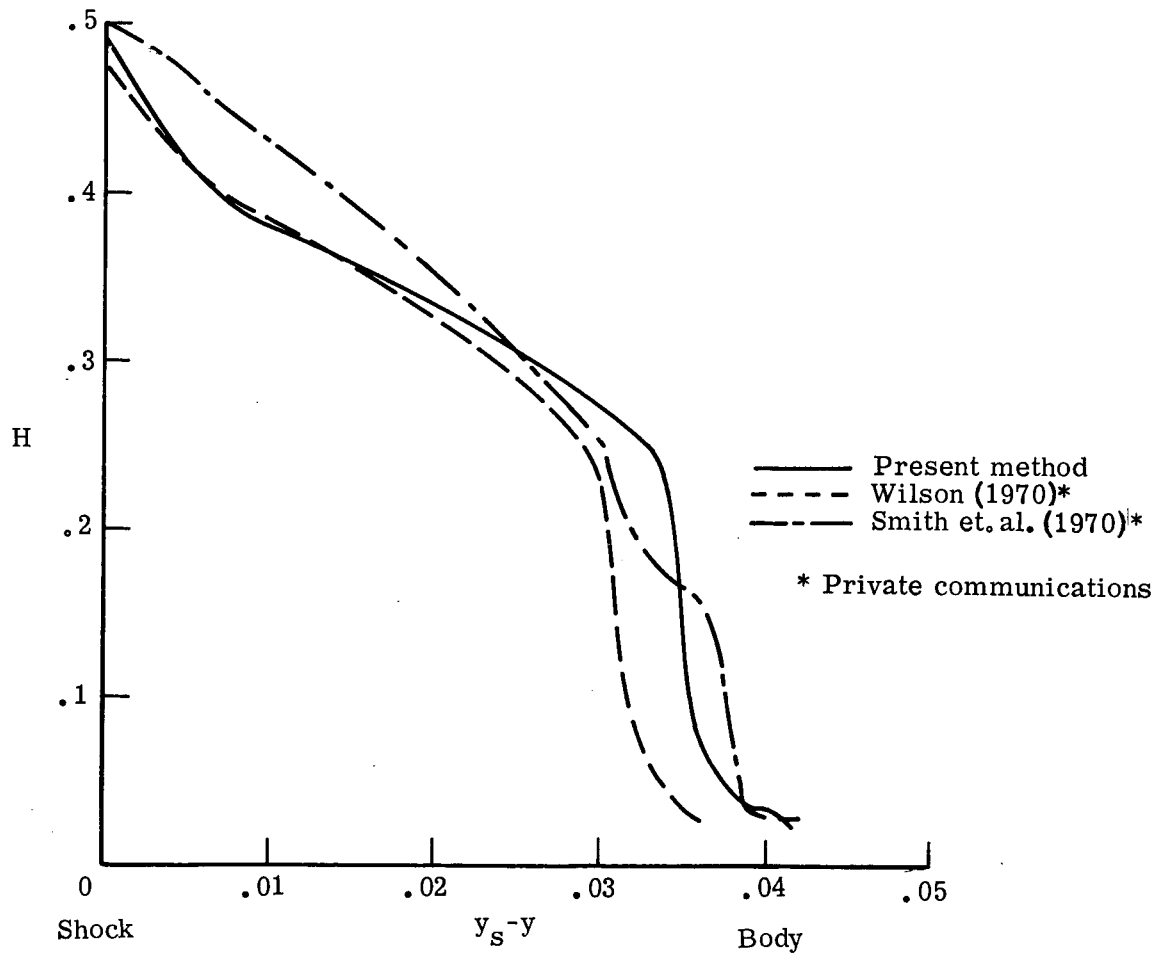


Figure 15. Comparison of the enthalpy profile along the stagnation line with solutions from complete subsonic flow field calculations - equilibrium air with radiation and without blowing



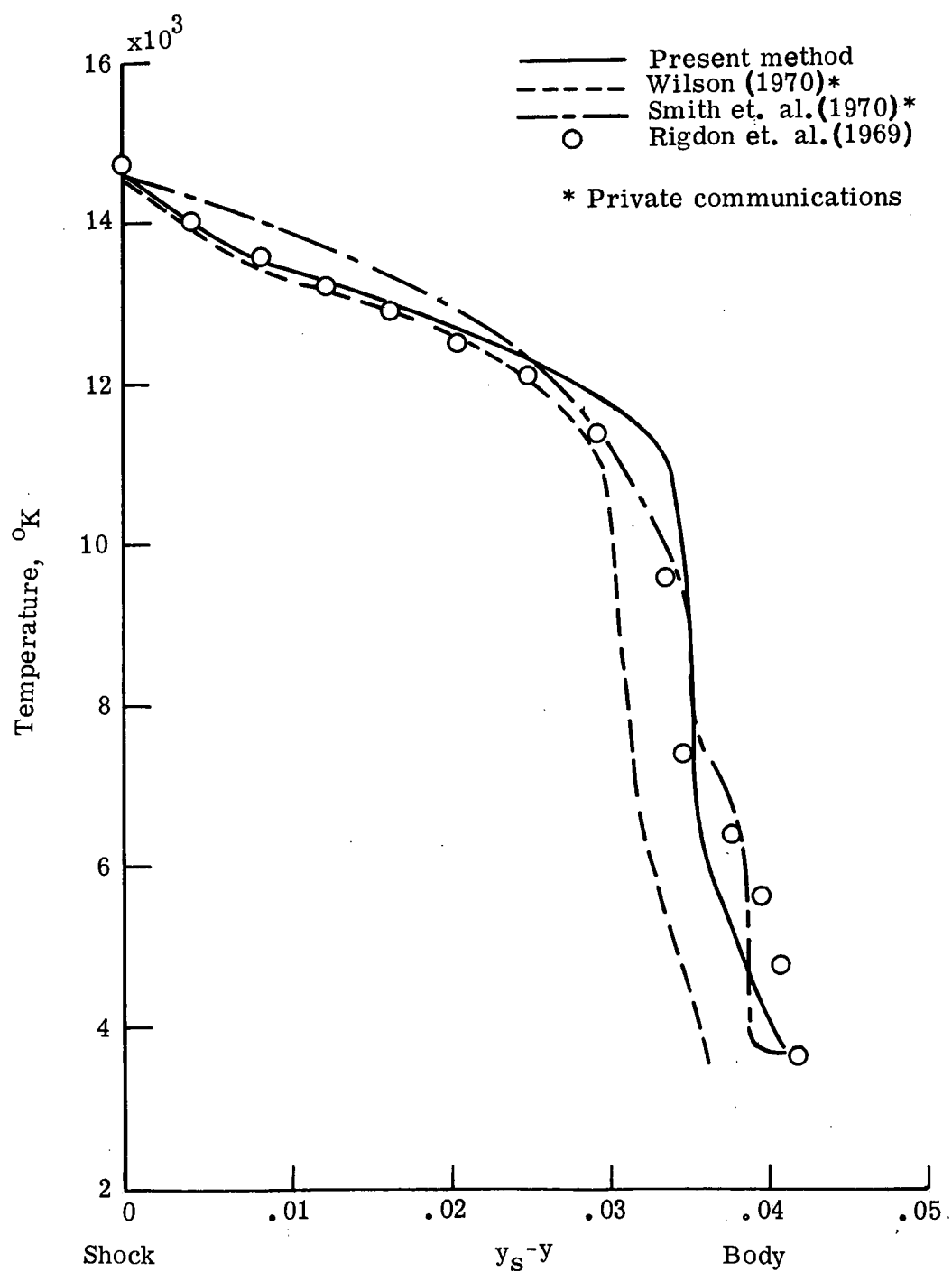
(a) Tangential velocity gradient

Figure 16. Comparison of equilibrium air solutions including radiation with air to air injection



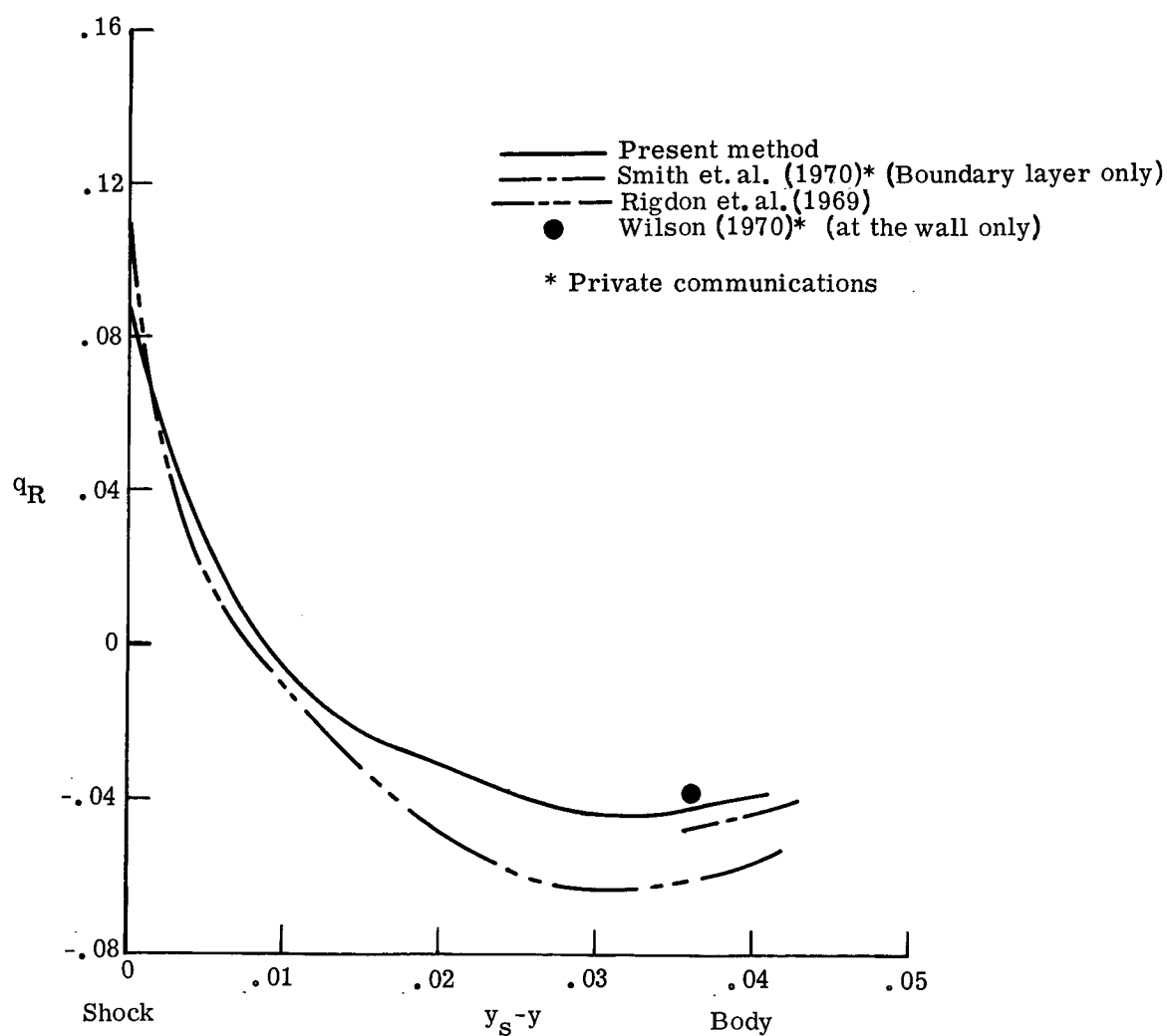
(b) Total enthalpy

Figure 16. Continued



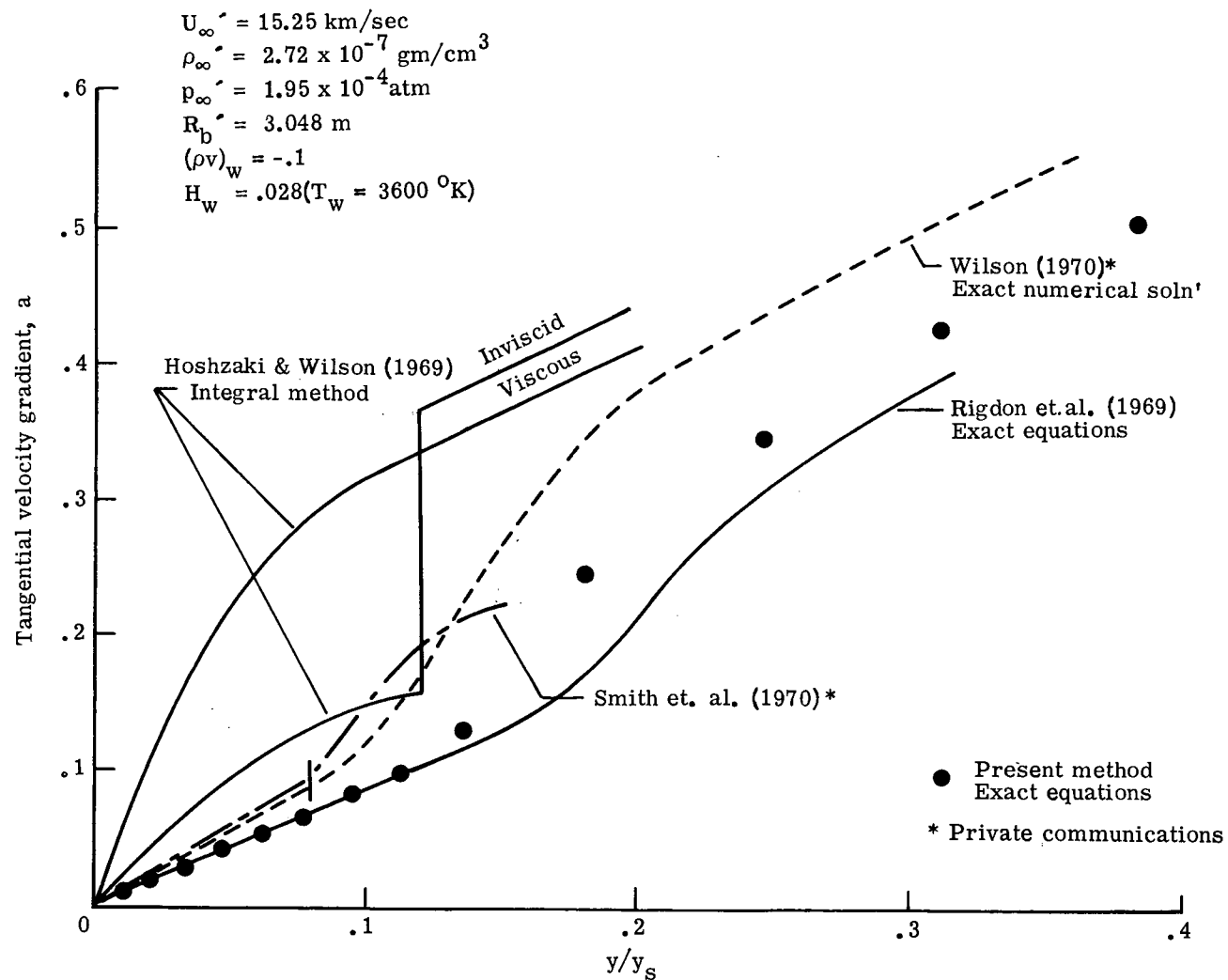
(c) Temperature

Figure 16. Continued



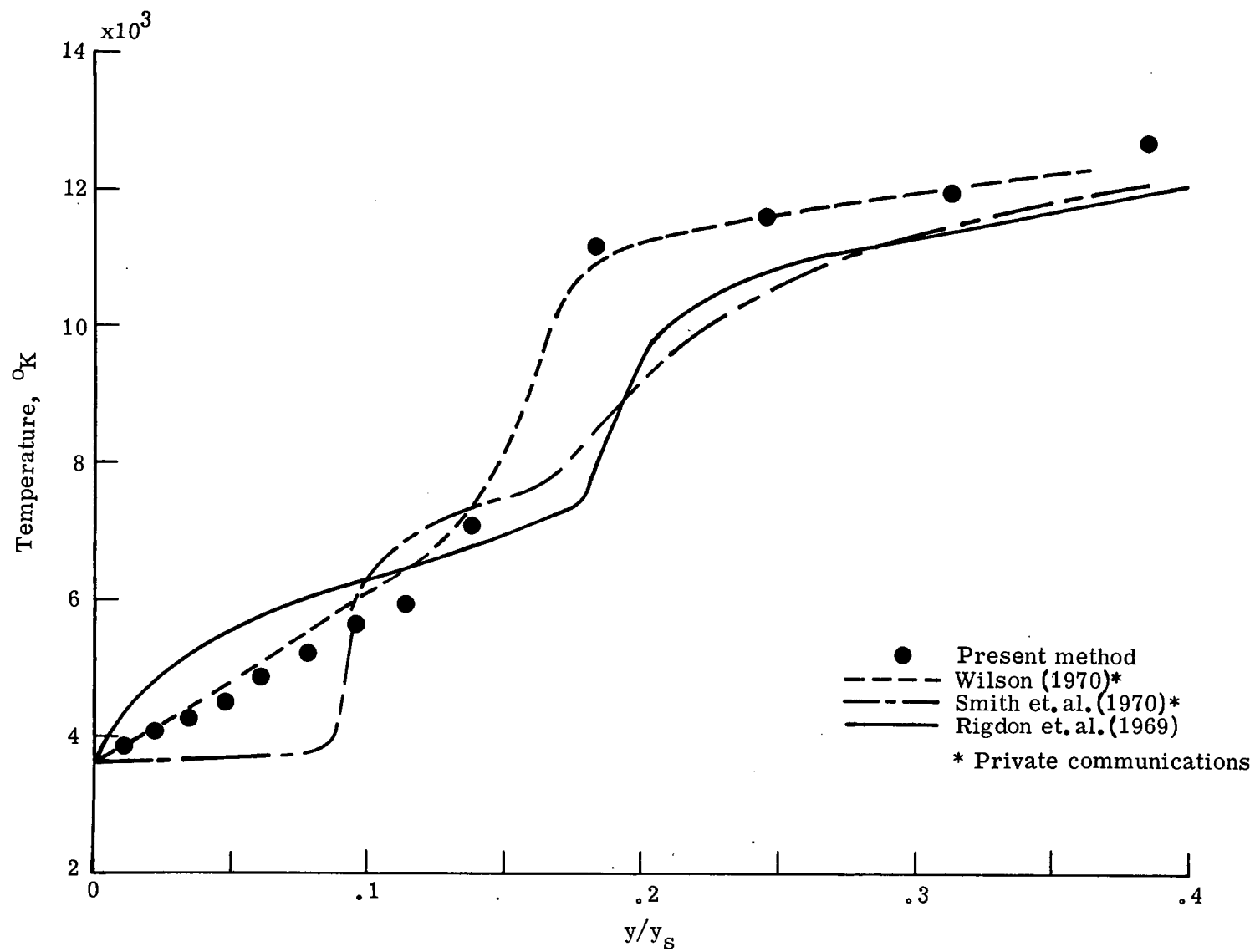
(d) Radiative heat flux

Figure 16. Concluded



(a) Tangential velocity gradient

Figure 17. Detailed comparisons near the wall of existing equilibrium air radiations shock layer solutions with air to air injection



(b) Temperature

Figure 17. Concluded

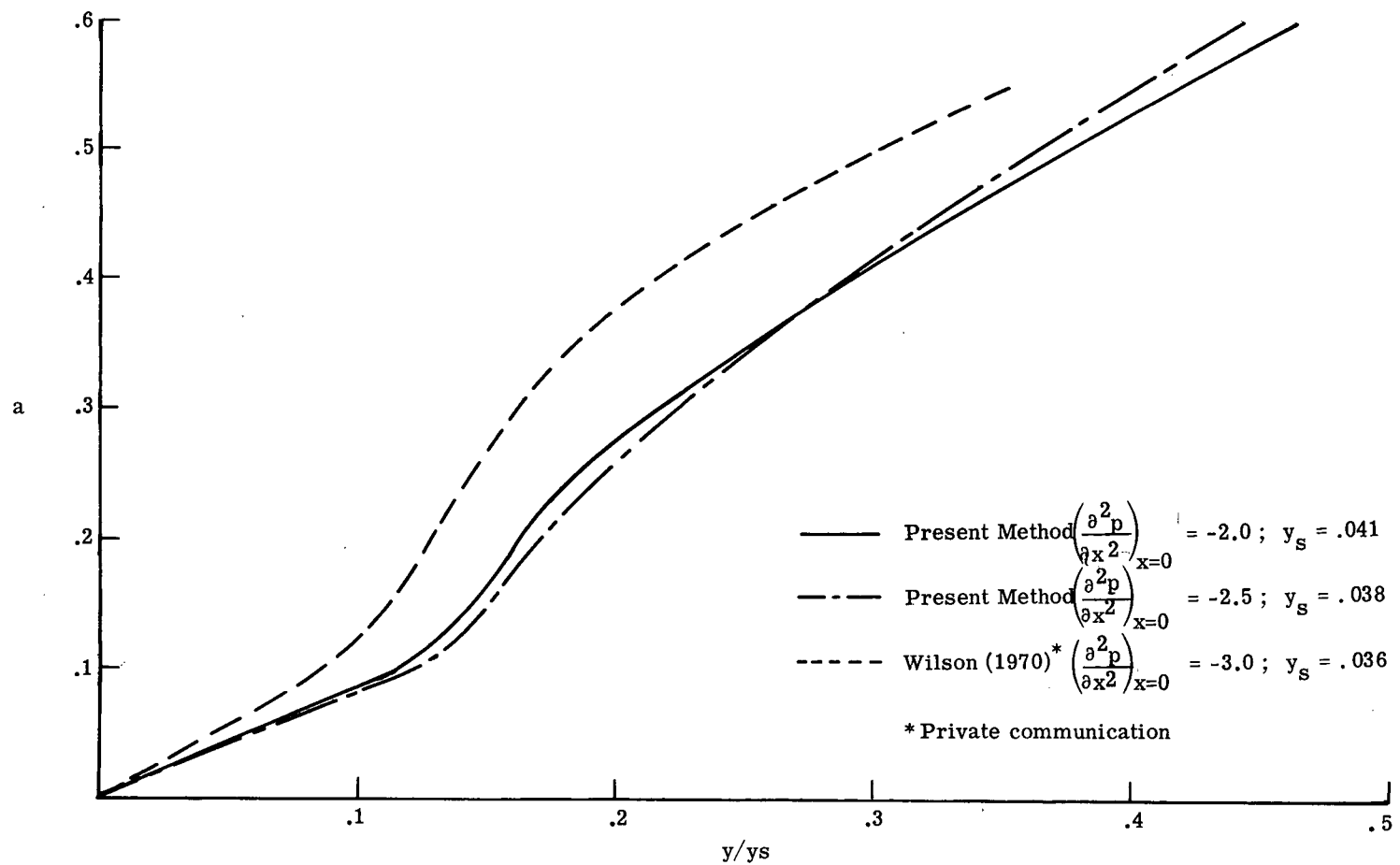
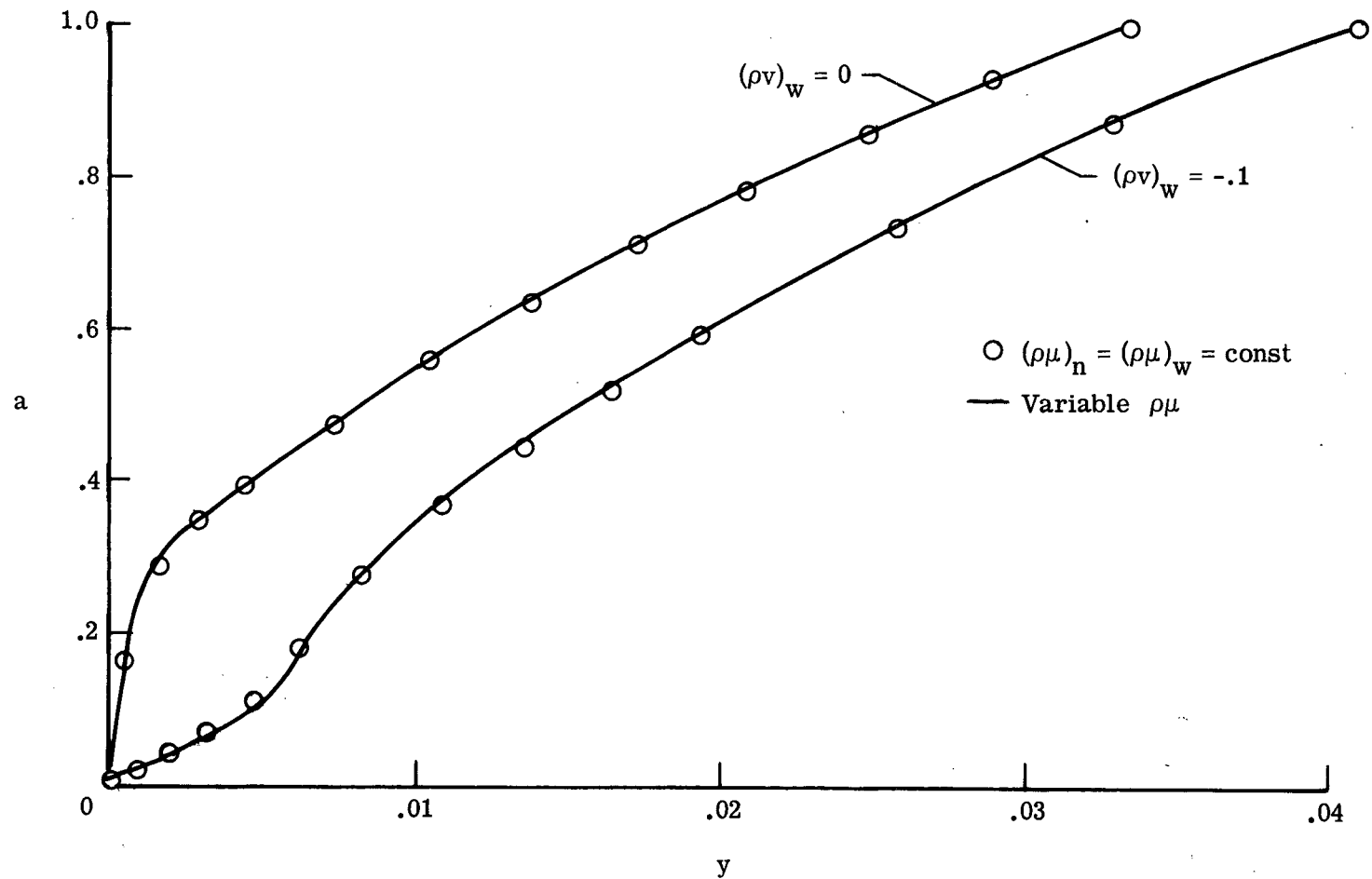
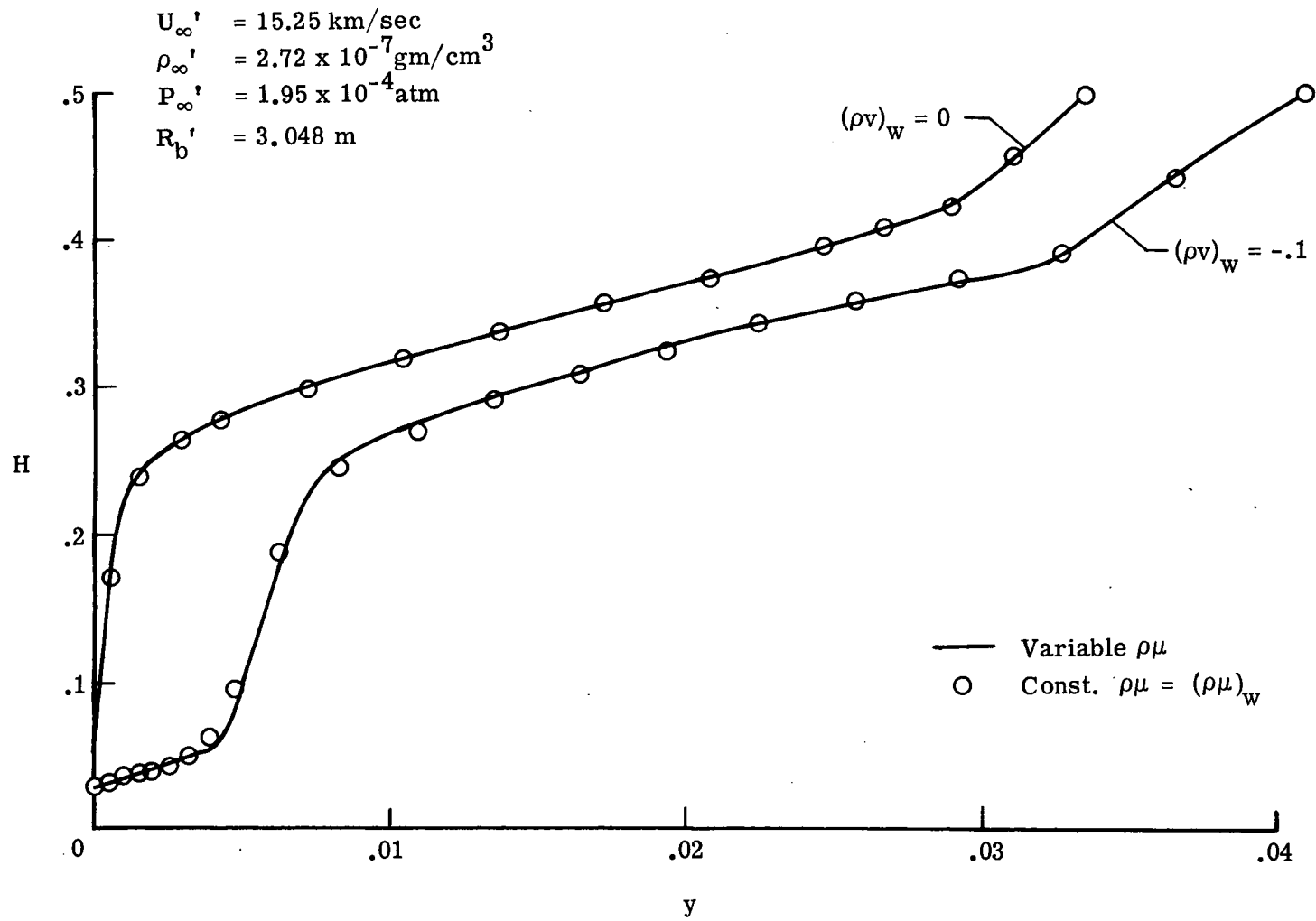


Figure 18. Effect of the pressure gradient on the tangential velocity gradient solution



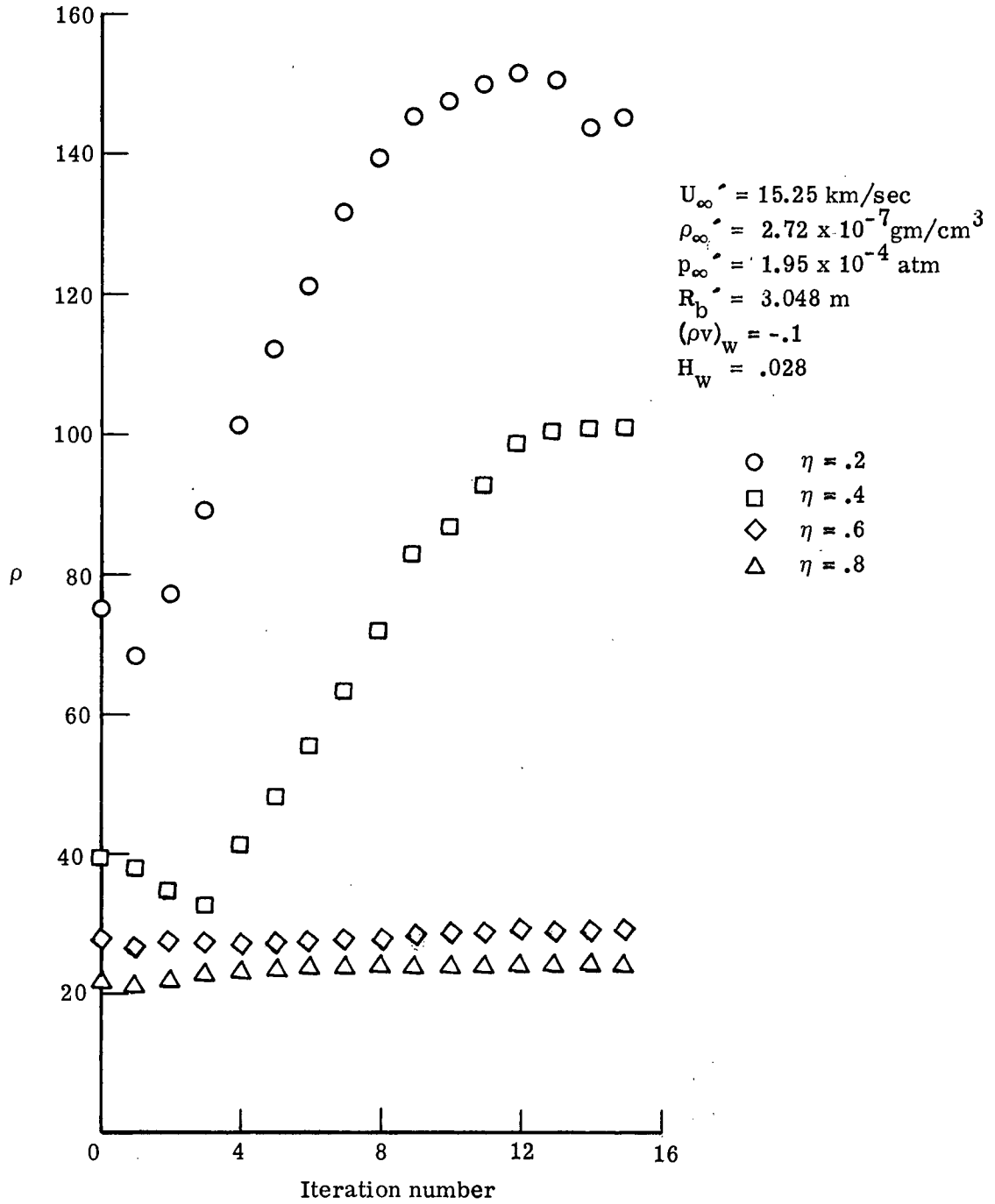
(a) Tangential velocity gradient

Figure 19. Effect of constant density viscosity product assumption on the solution



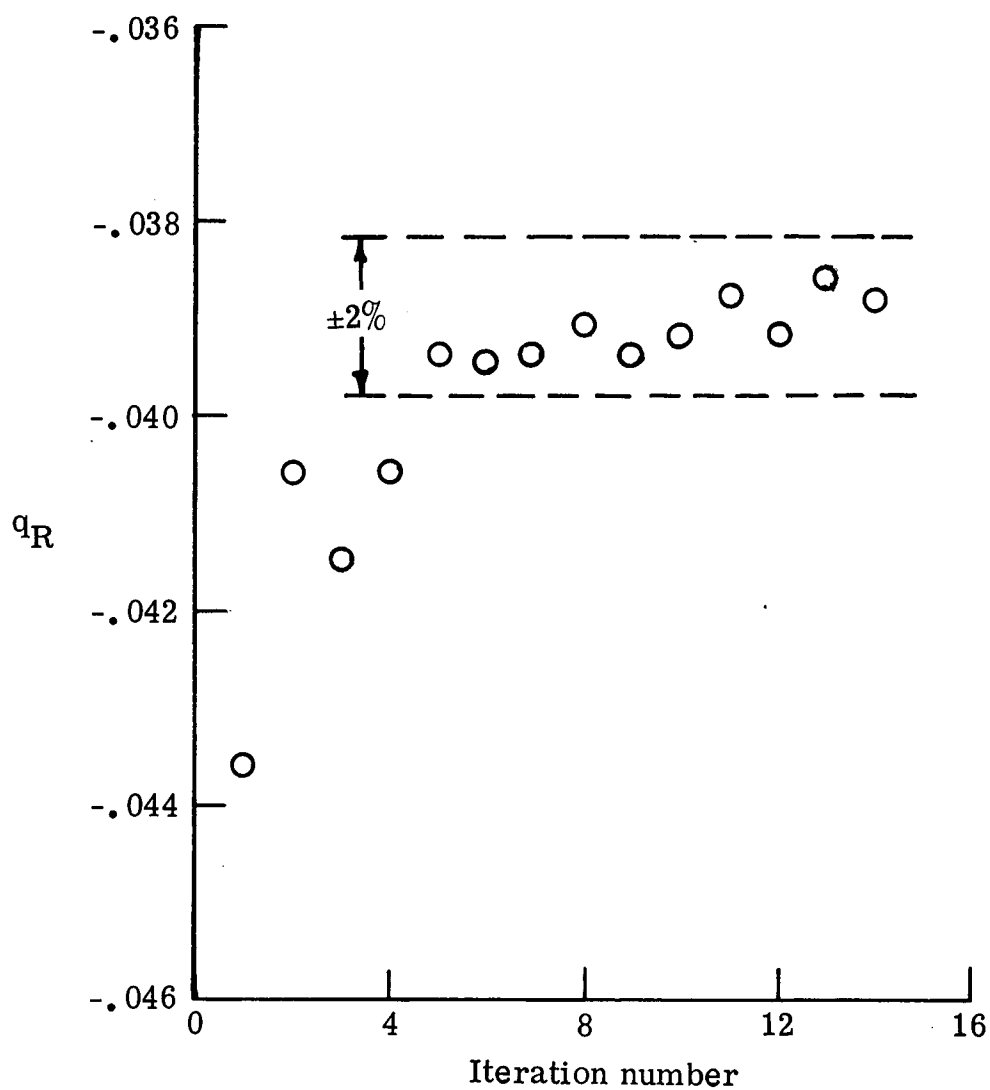
(b) Total enthalpy

Figure 19. Concluded



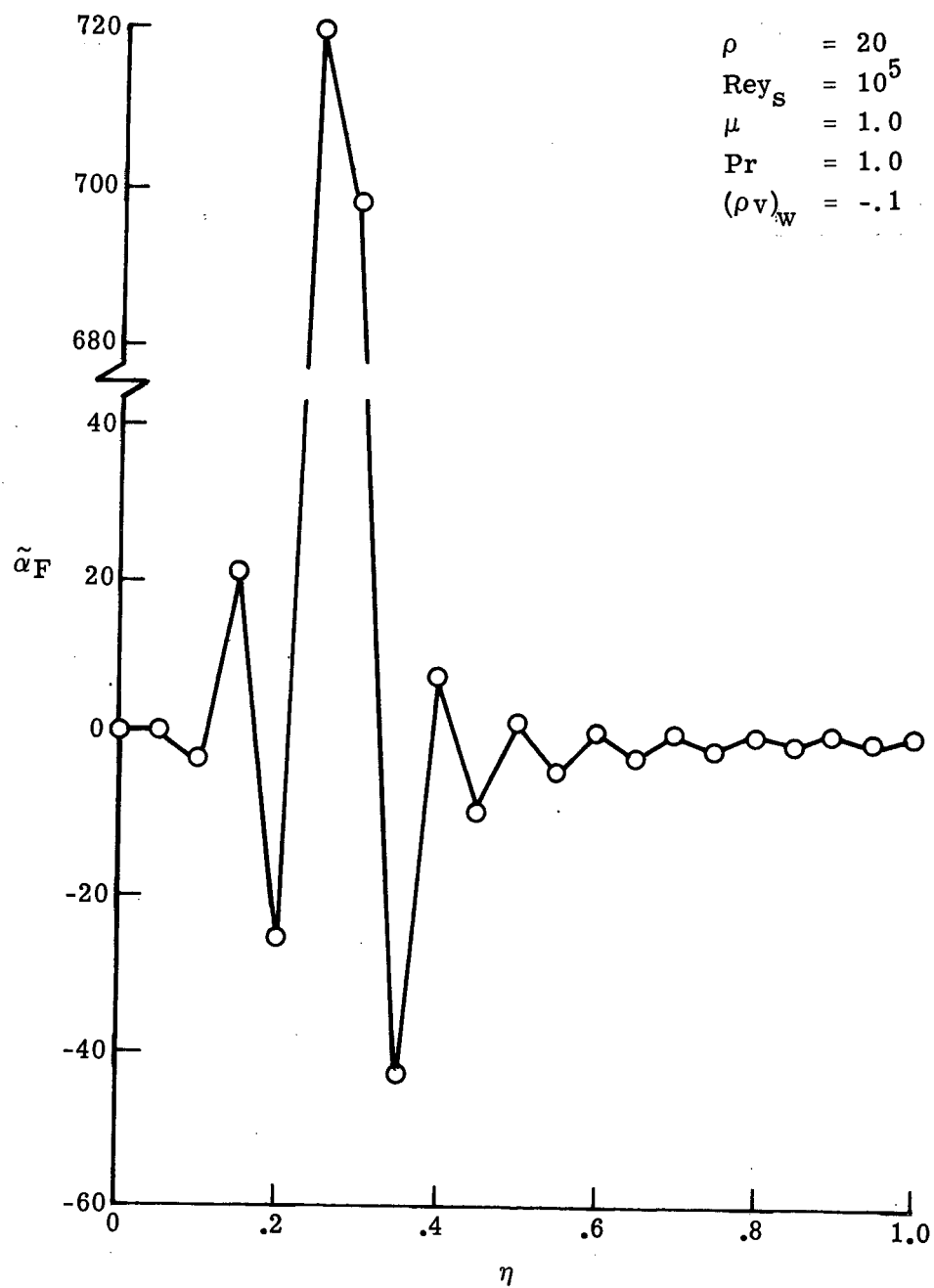
(a) Density behavior

Figure 20. Study of the sensitivity of the radiative heat flux to the density as the solution converges - equilibrium air with radiation



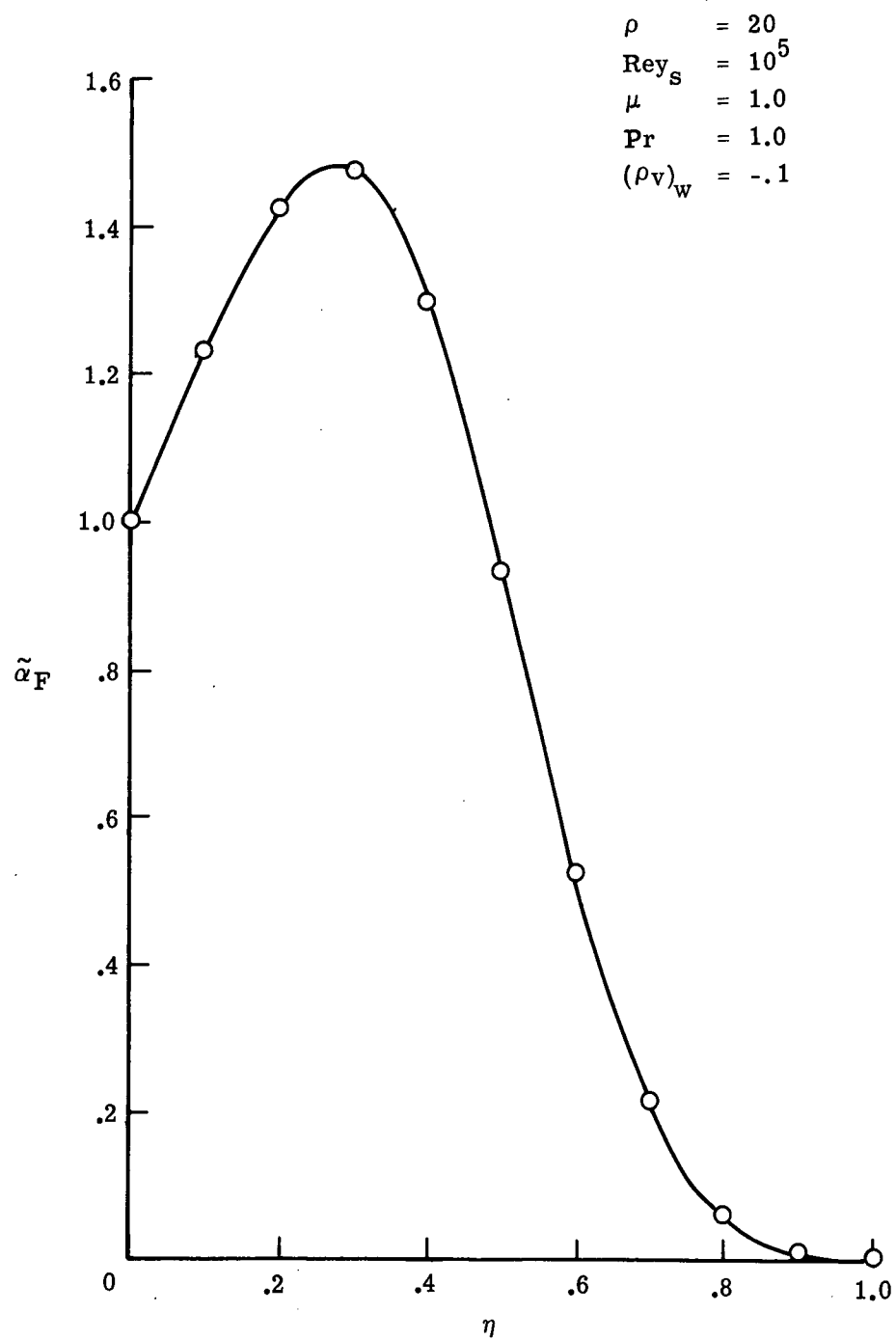
(b) Radiative heat flux behavior

Figure 20. Concluded



(a) $D_{12} = 10^{-6}$

Figure 21. Solution to the central difference form of the elemental diffusion equation for a constant density flow



(b) $D_{12} = 1.25 \times 10^{-4}$

Figure 21. Concluded

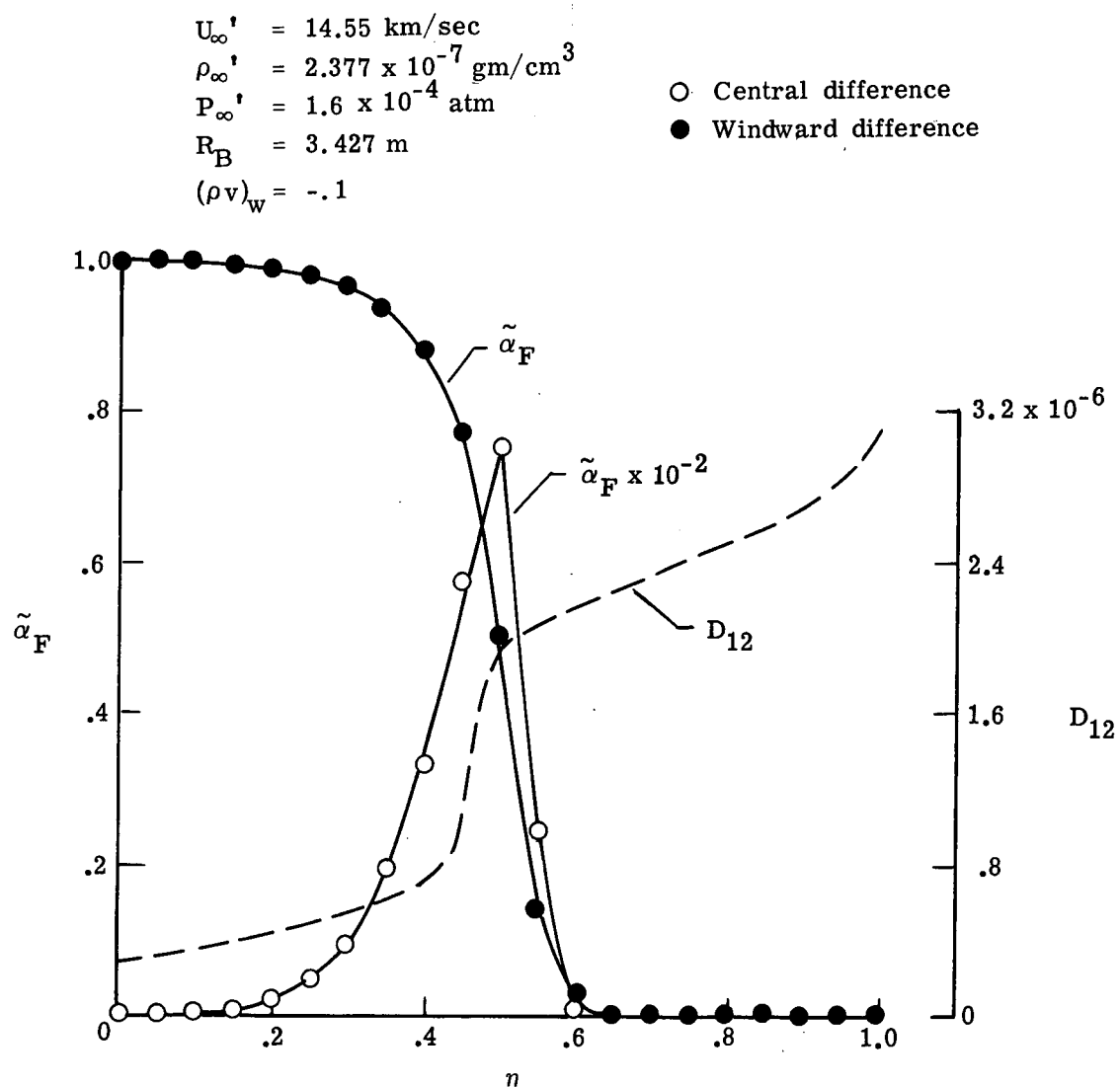


Figure 22. Stability of the elemental diffusion equation for central and windward difference approximations

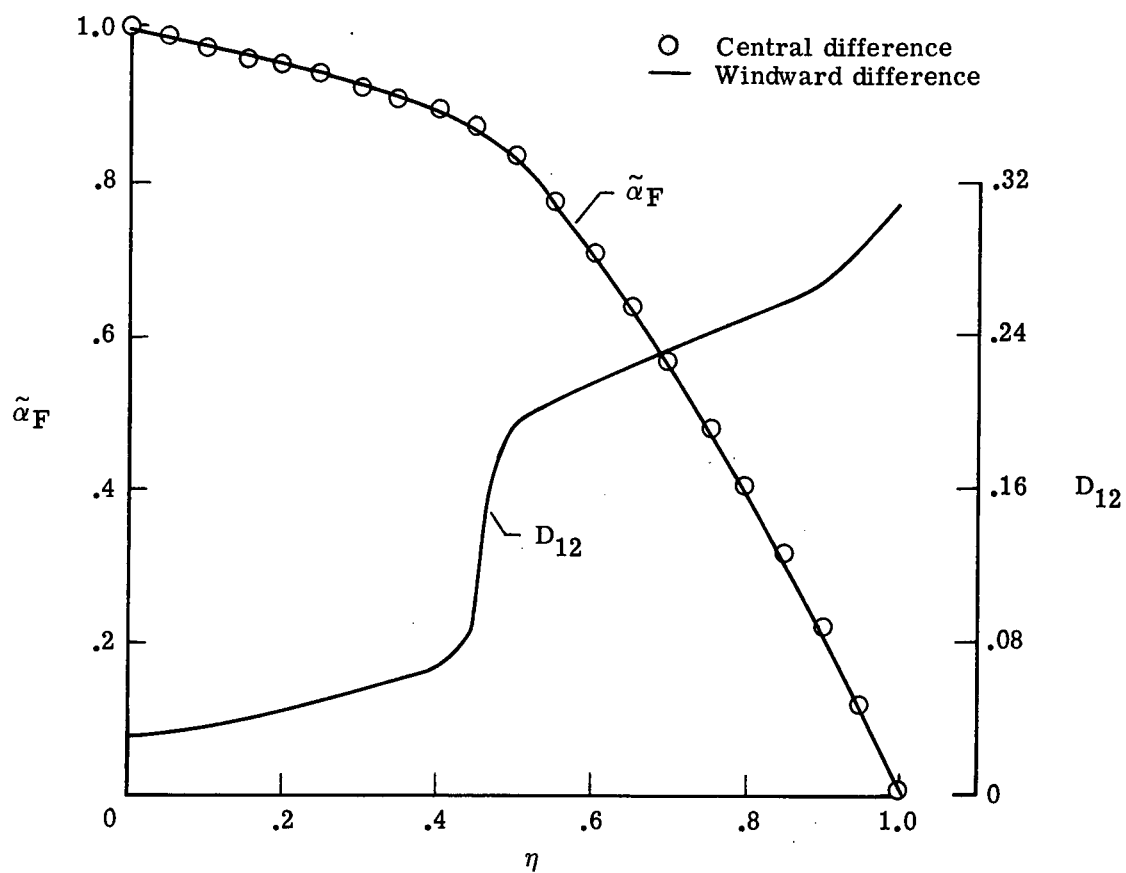
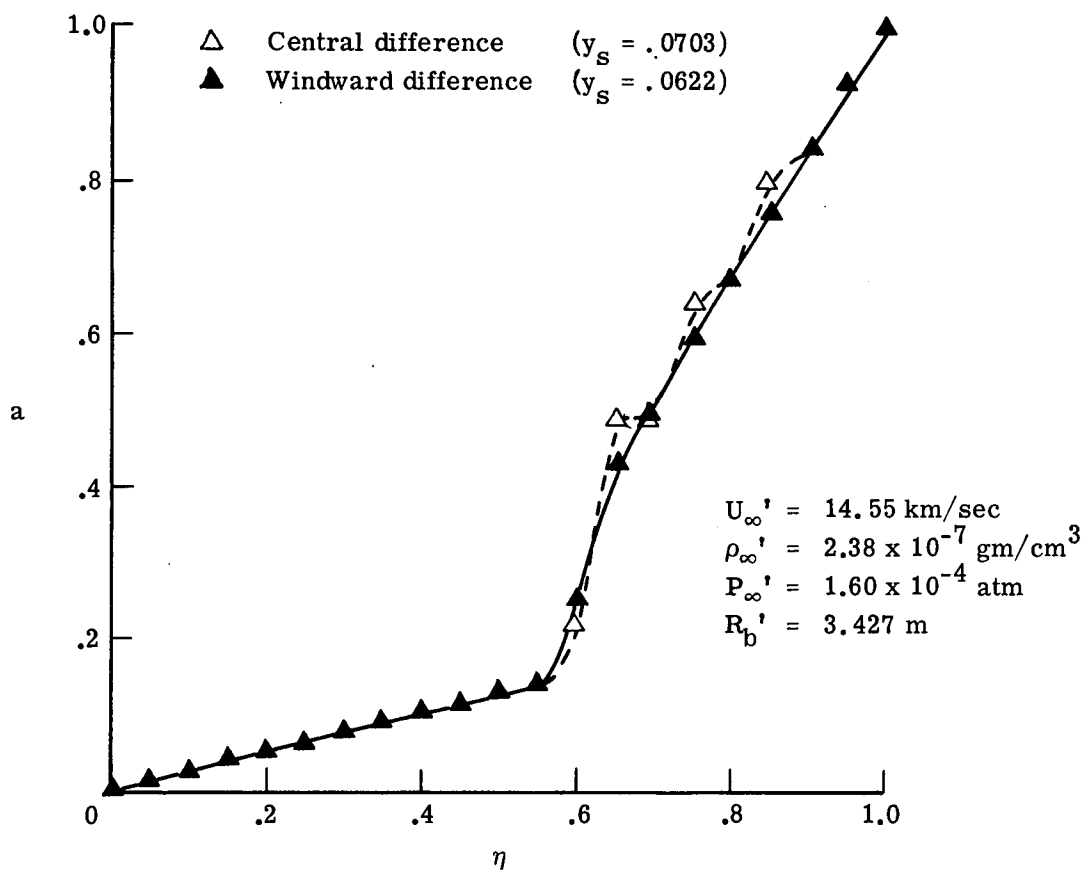
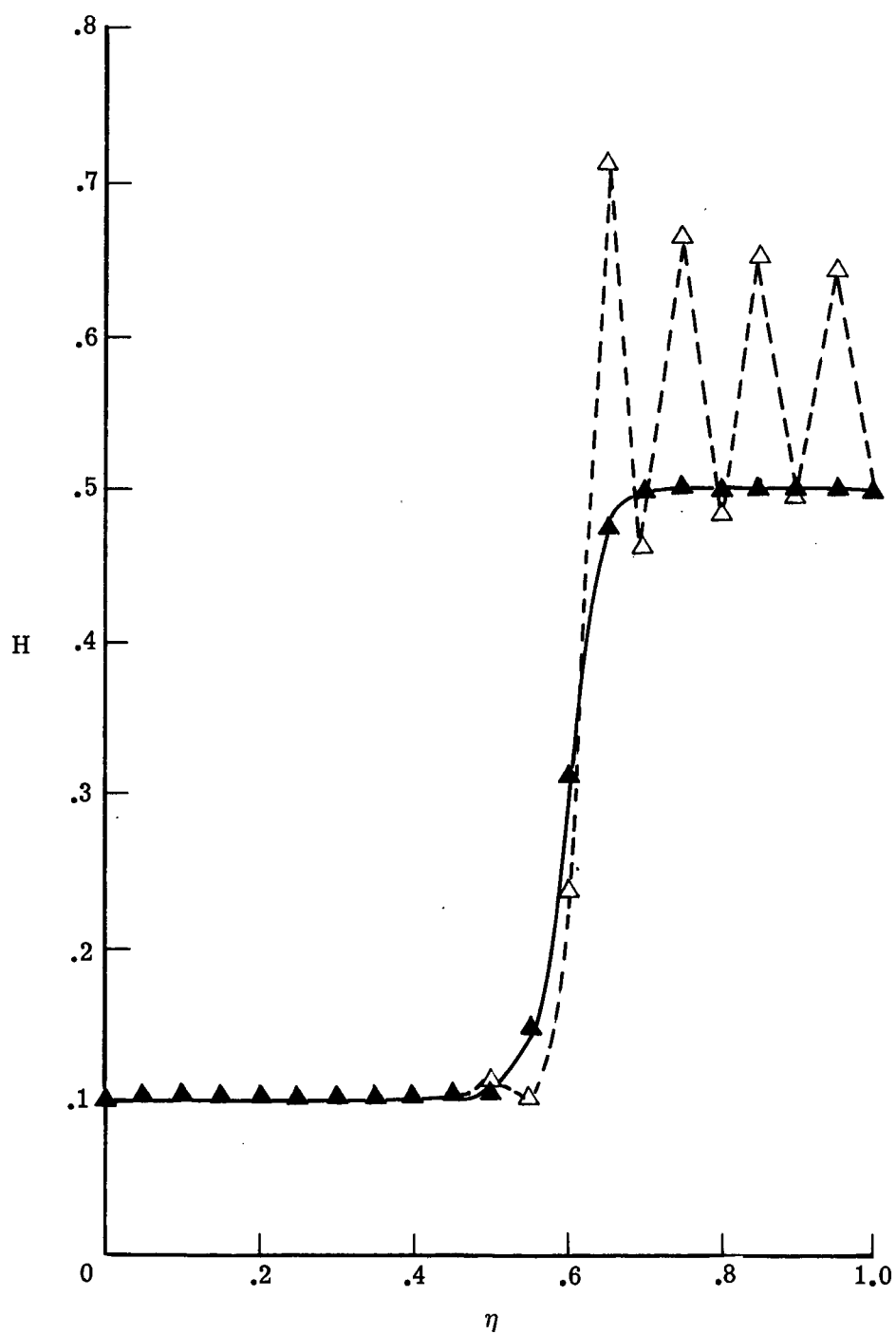


Figure 23. Comparison of solutions of the elemental diffusion equation for central and windward difference approximations in the region where the equations are stable



(a) X-momentum equation

Figure 24. Effect of windward differencing the energy equation on the non-radiating air solution with massive blowing, $(\rho v)_W = -0.2$



(b) Energy equation

Figure 24. Concluded

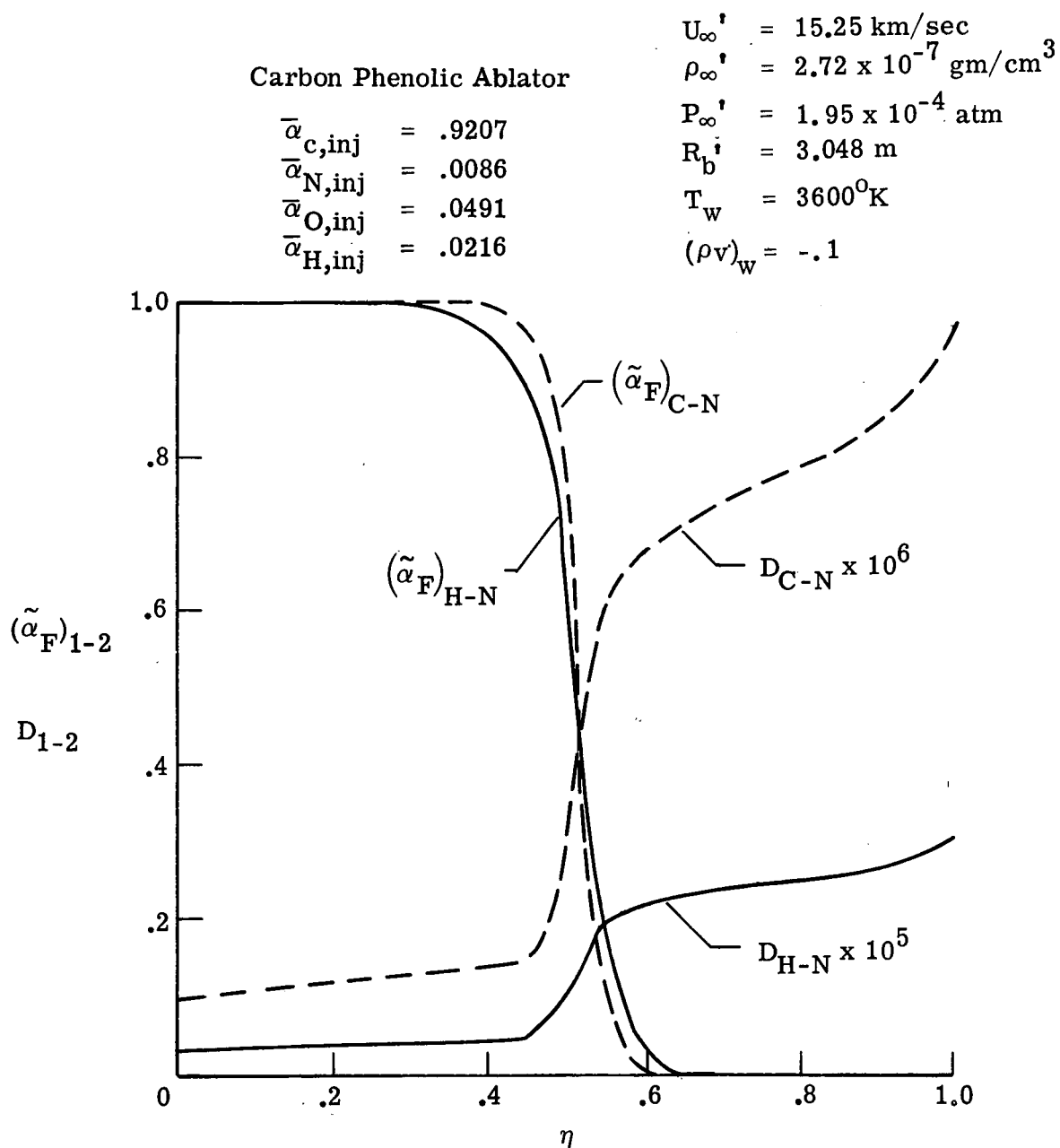


Figure 25. Comparison of ablator mass fraction profiles assuming binary carbon-nitrogen diffusion and hydrogen-nitrogen diffusion

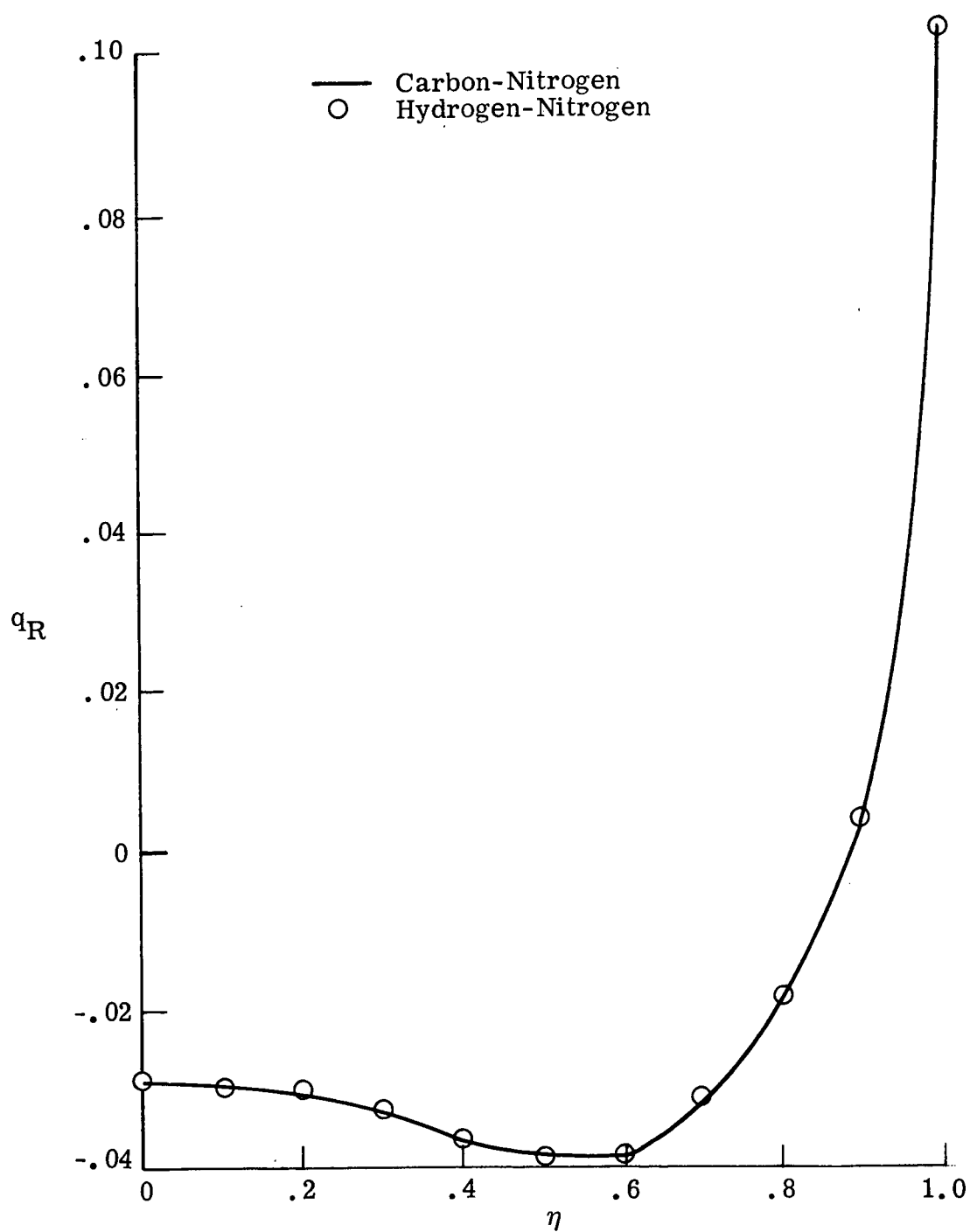
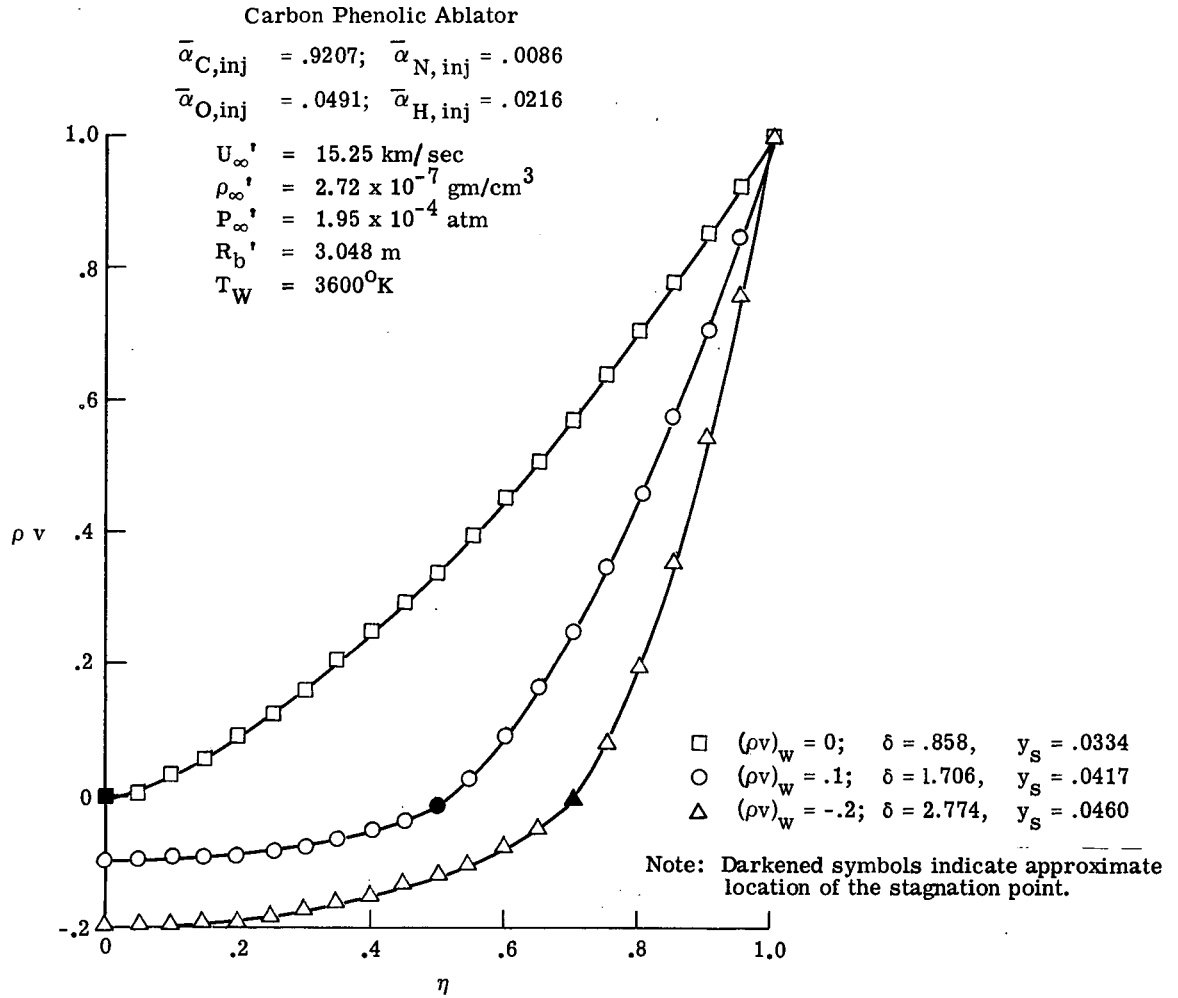
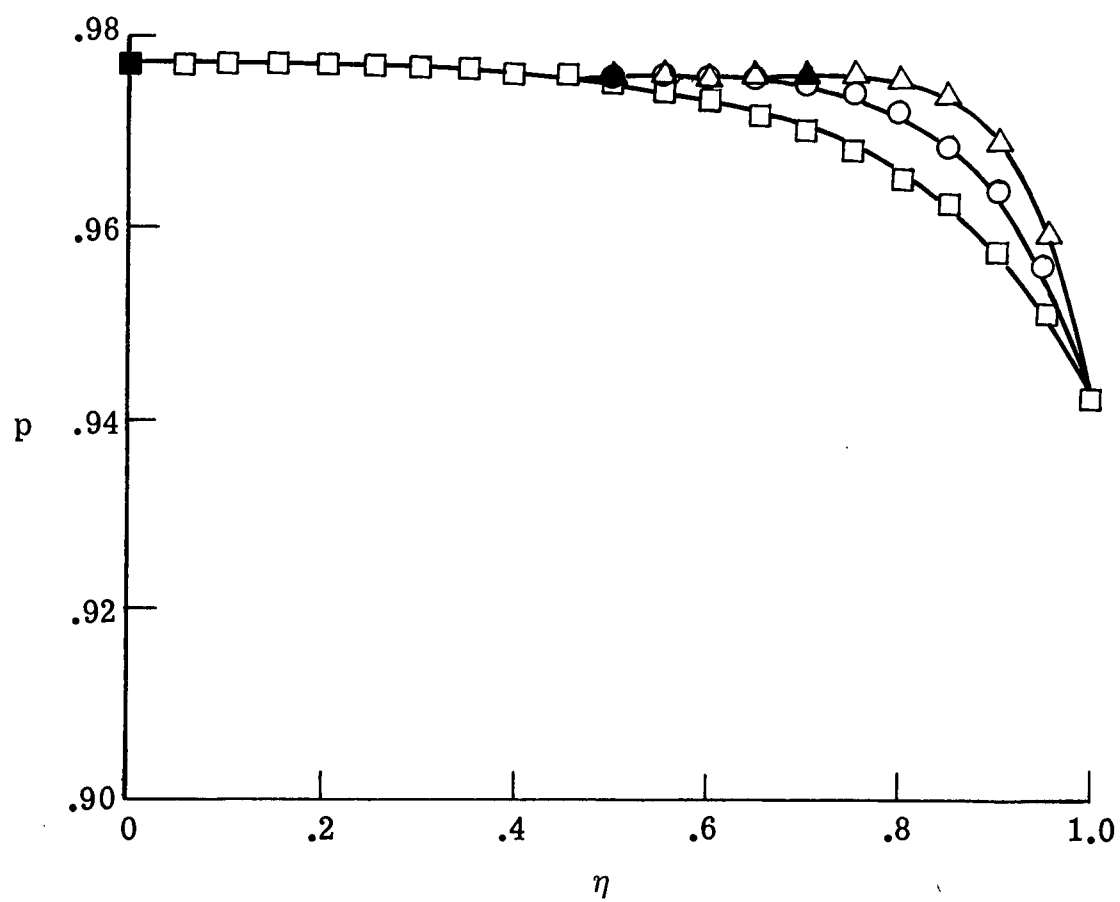


Figure 26. Effect of the binary carbon-nitrogen and binary hydrogen-nitrogen diffusion models on the radiative heat fluxes



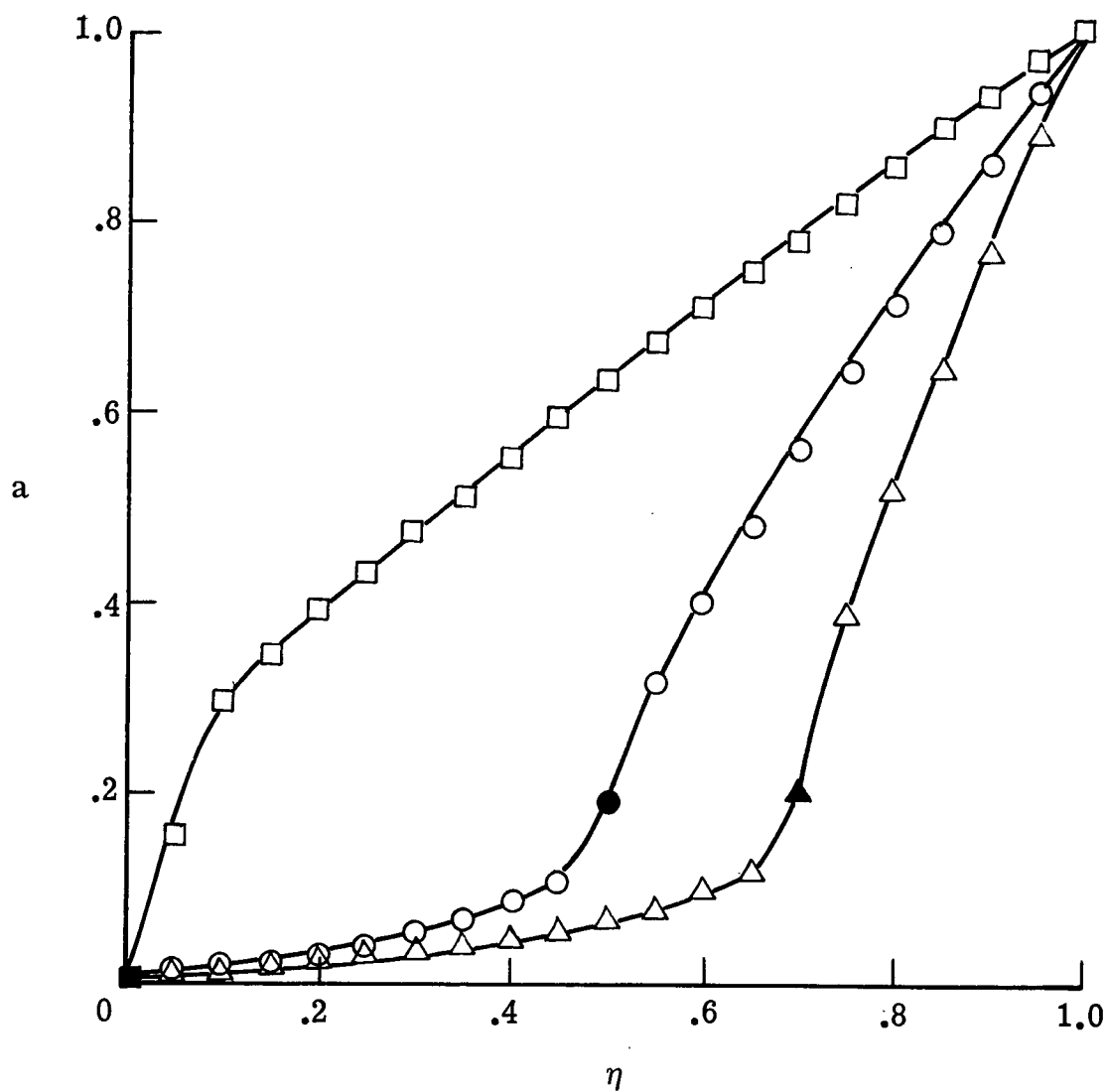
(a) Continuity equation

Figure 27. Radiating shock layer solutions with ablation products



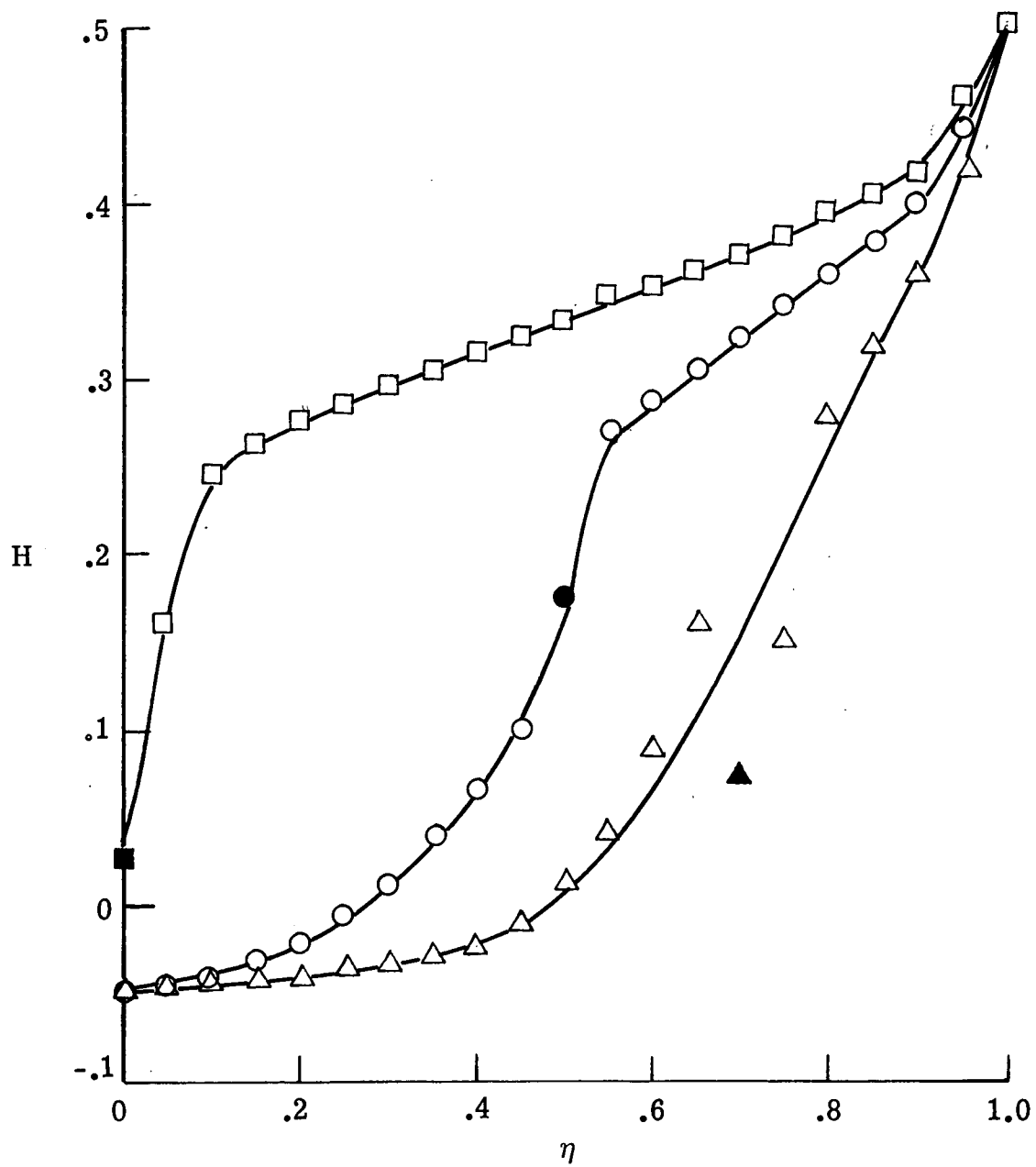
(b) Y-momentum equation

Figure 27. Continued



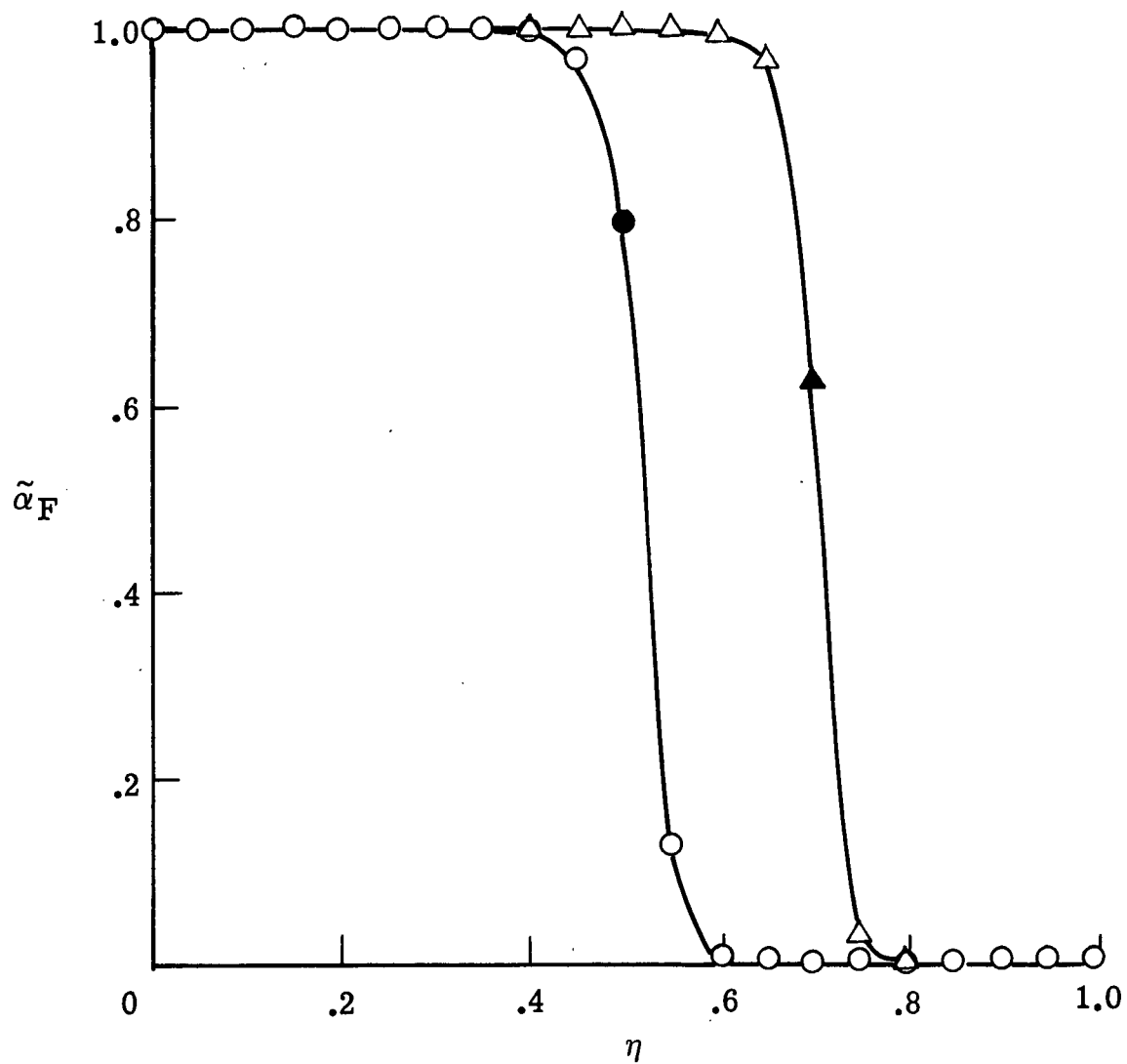
(c) X-momentum equation

Figure 27. Continued



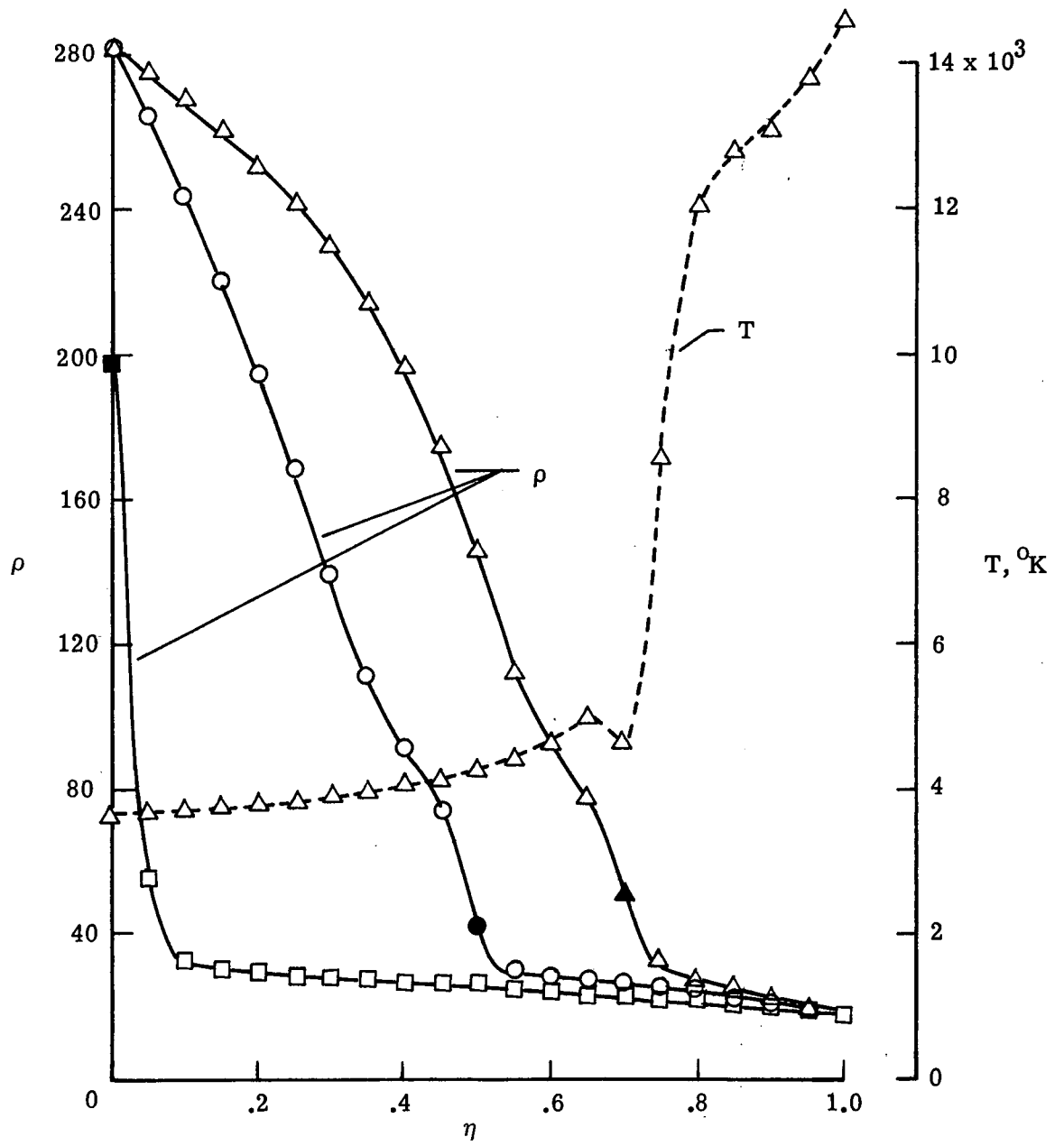
(d) Energy equation

Figure 27. Continued



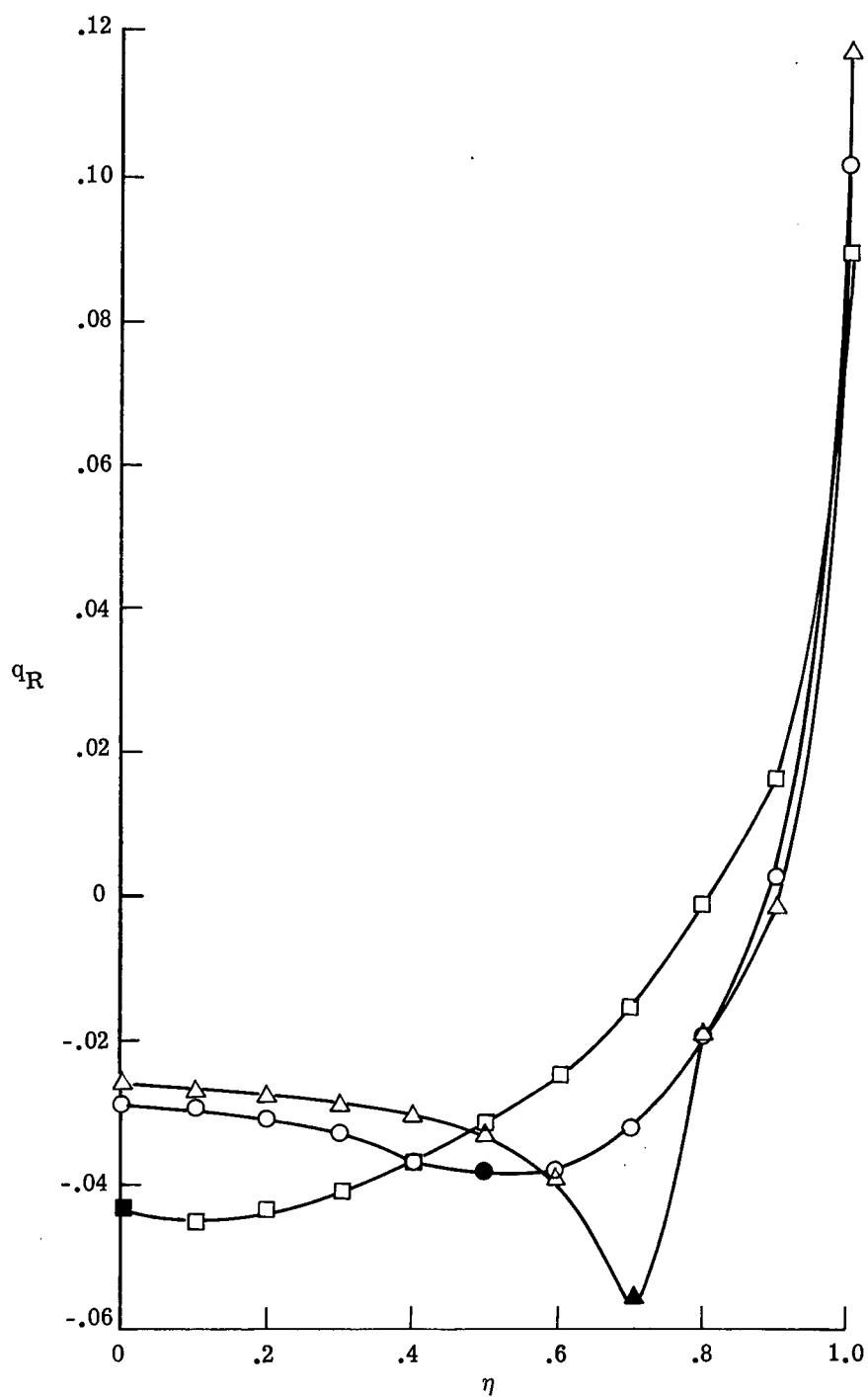
(e) Elemental diffusion equation

Figure 27. Continued



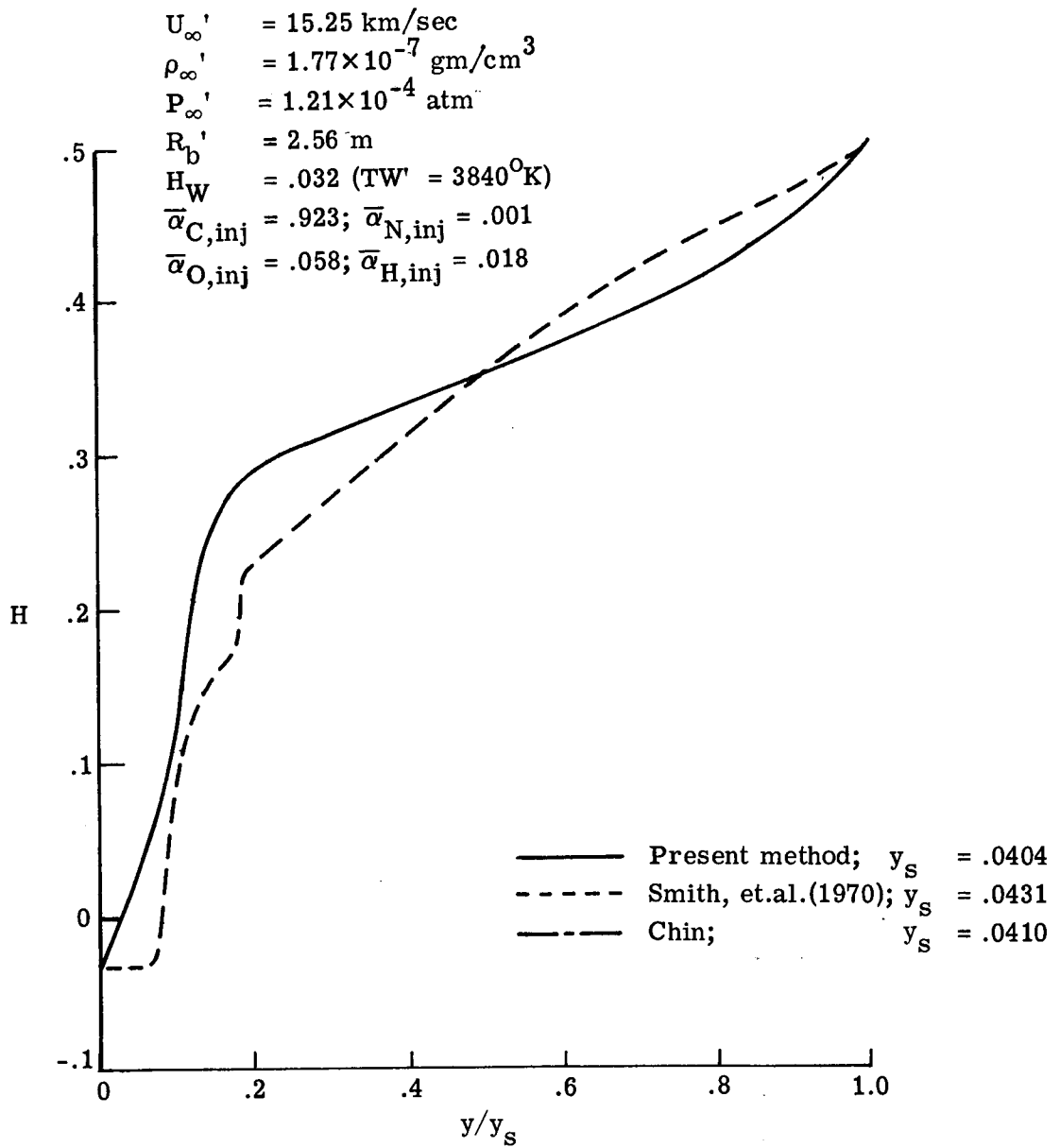
(f) Equation of state

Figure 27. Continued



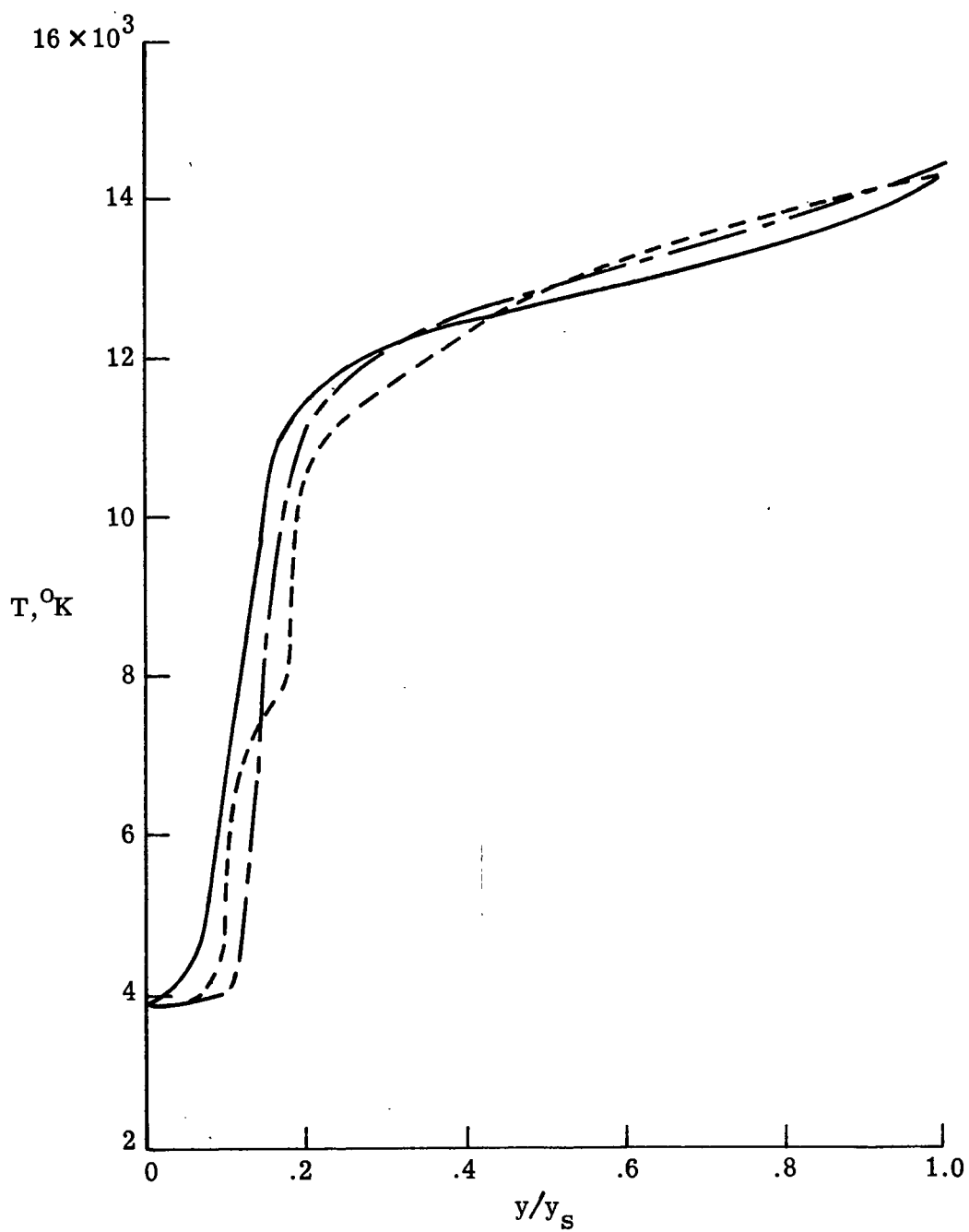
(g) Radiative heat flux

Figure 27. Concluded



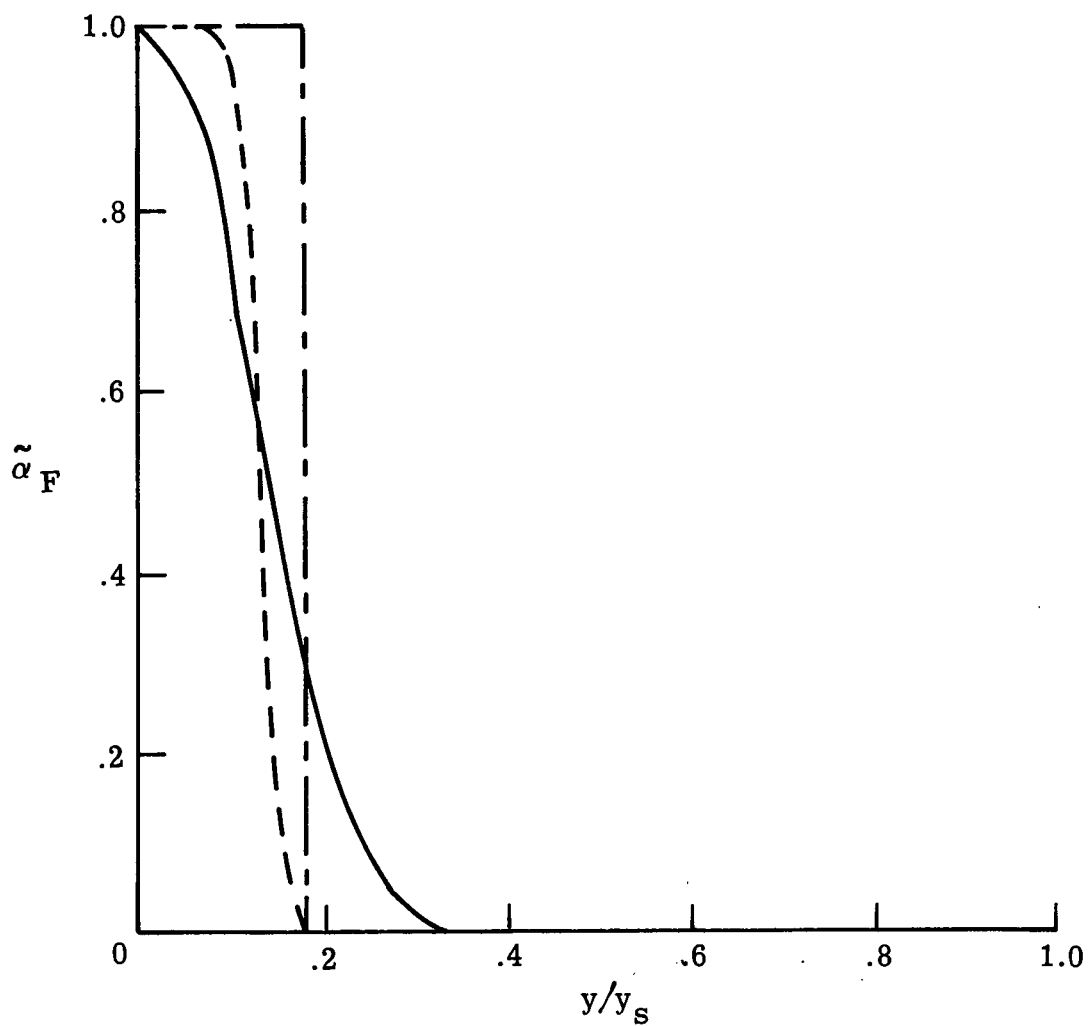
(a) Enthalpy

Figure 28. Comparison of flow field results for carbon phenolic injection at $(\rho v)_W = -0.076$



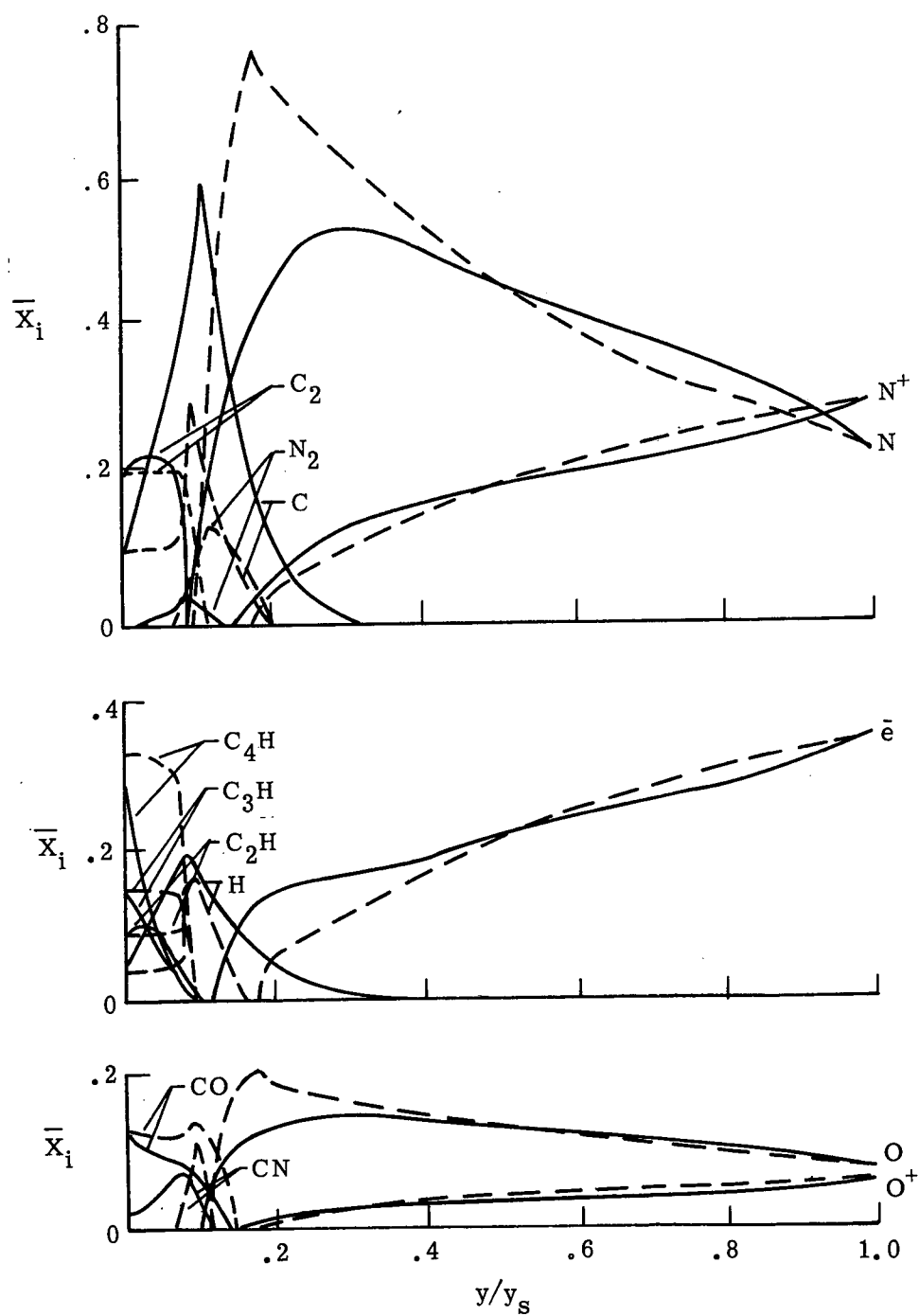
(b) Temperature

Figure 28. Continued



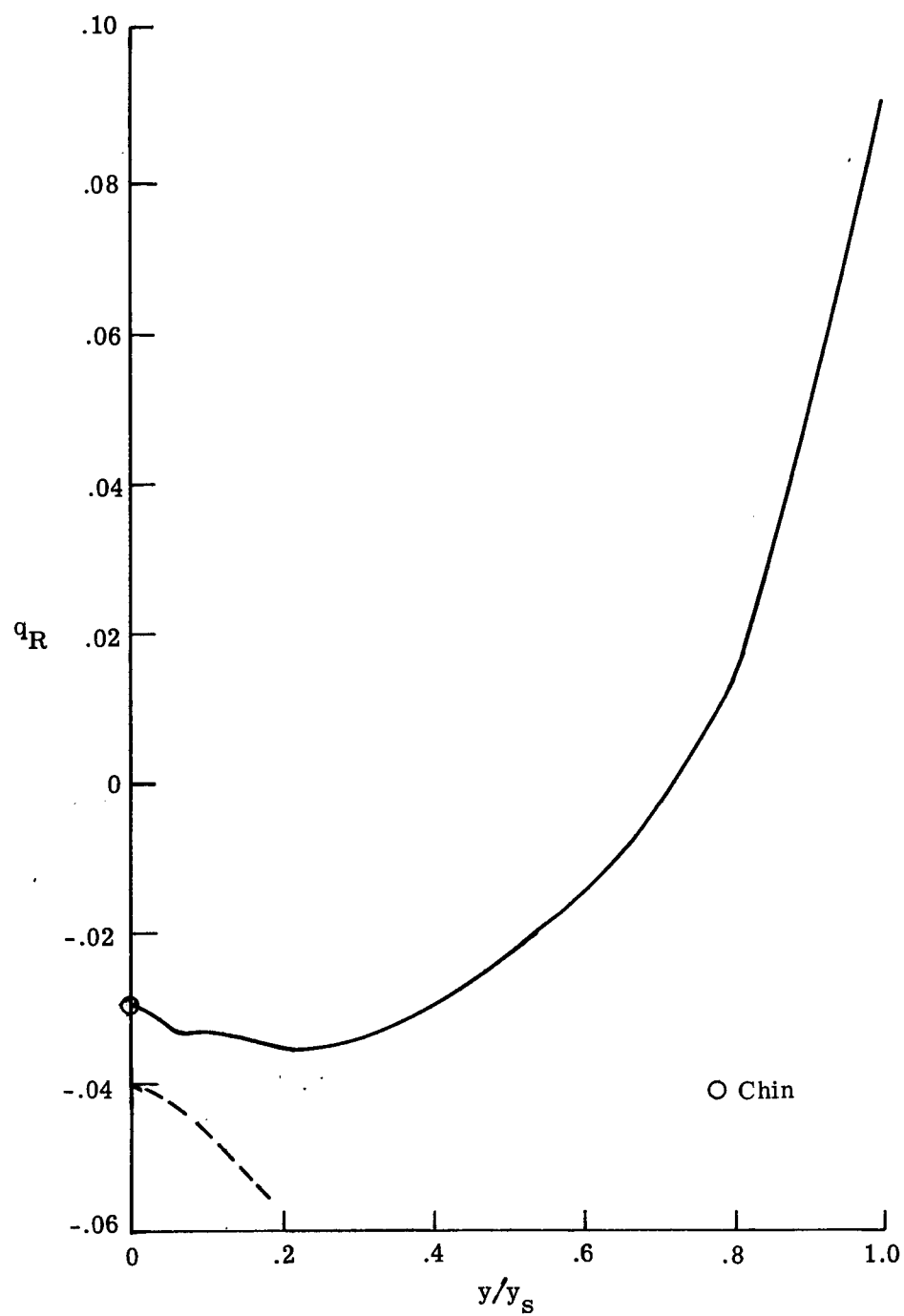
(c) Ablator mass fraction

Figure 28. Continued



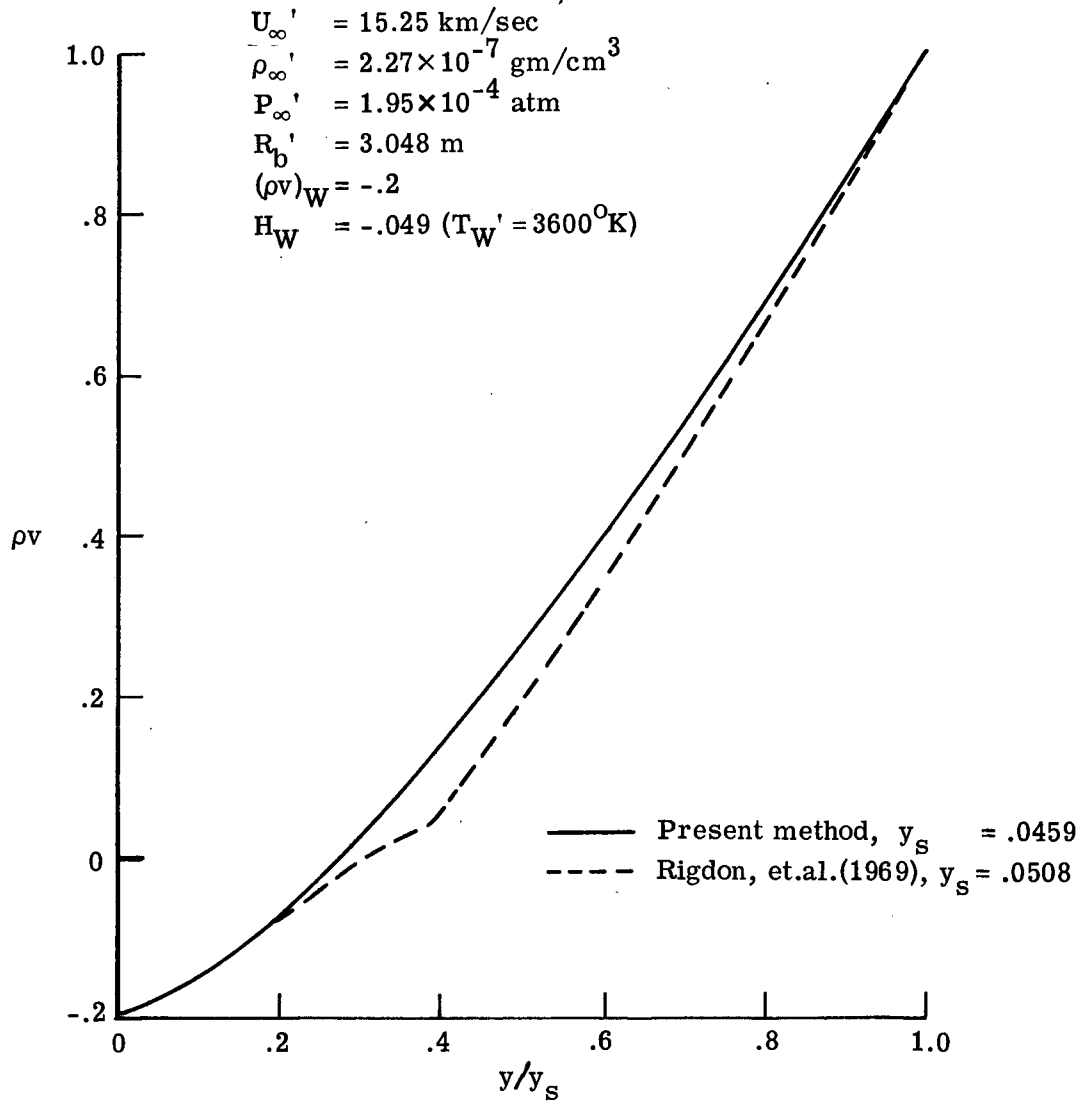
(d) Mole fractions

Figure 28. Continued



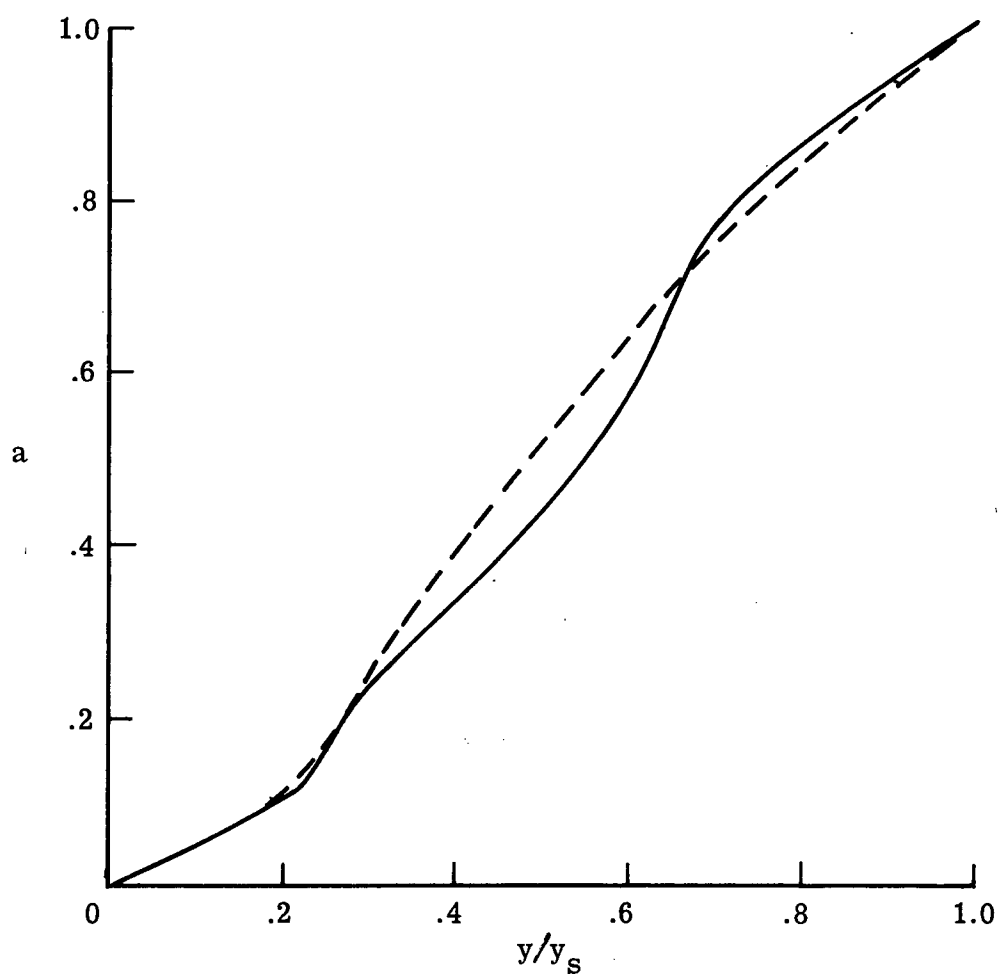
(e) Radiative heat flux

Figure 28. Concluded



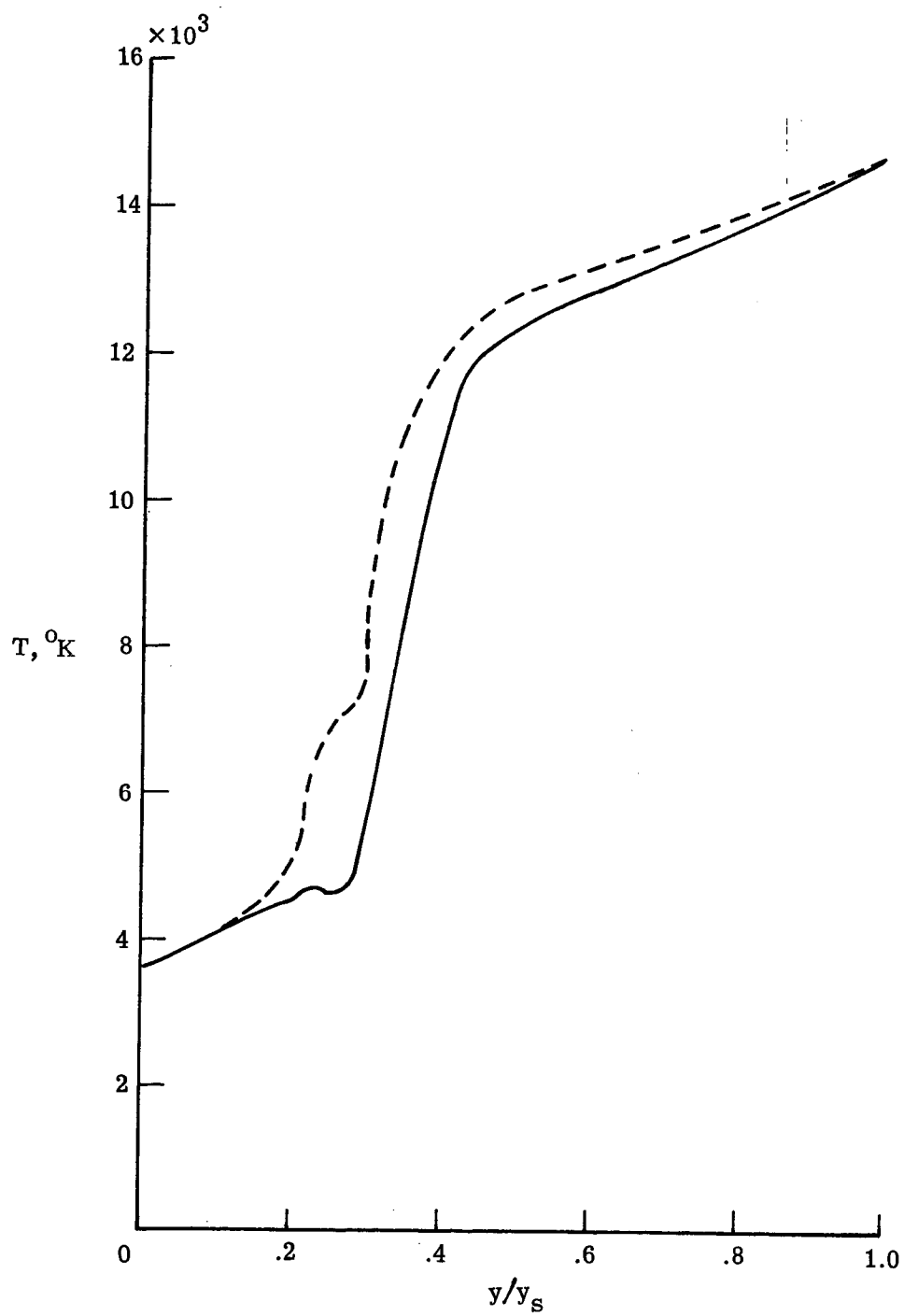
(a) Mass flux

Figure 29. Comparison of flow field results for carbon phenolic injection at $(\rho v)_W = -0.2$



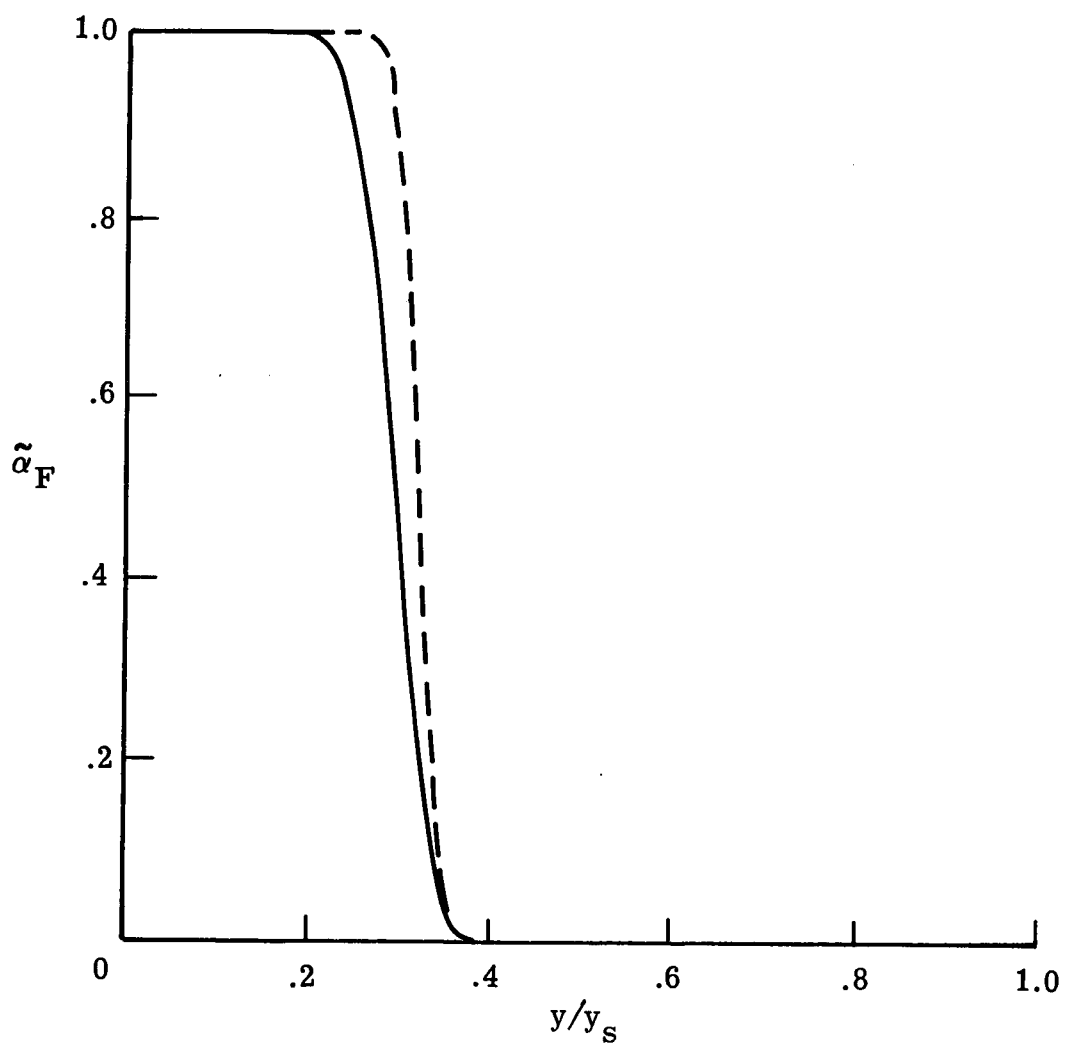
(b) Velocity gradient

Figure 29. Continued



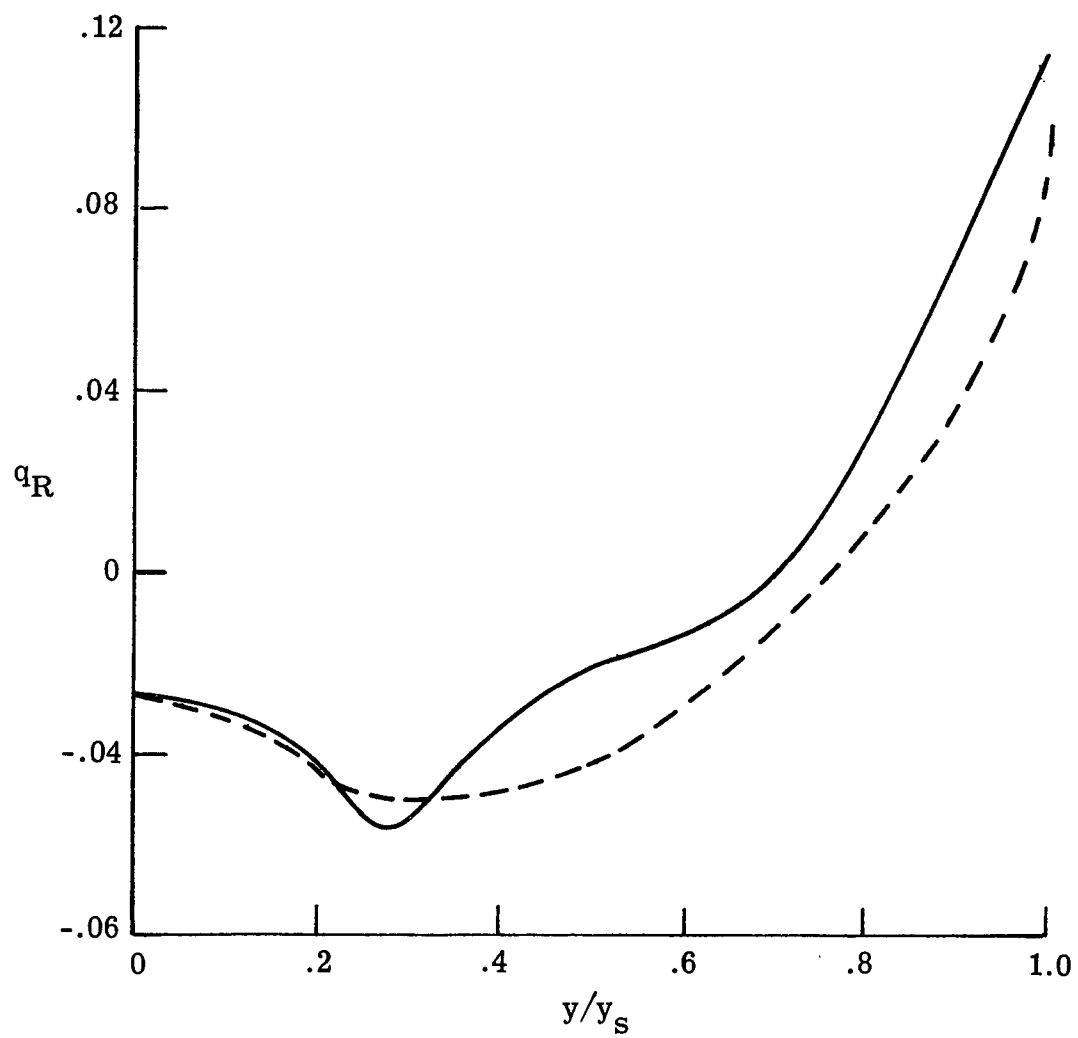
(c) Temperature

Figure 29. Continued



(d) Ablator mass fraction

Figure 29. Continued



(e) Radiative heat flux

Figure 29. Concluded

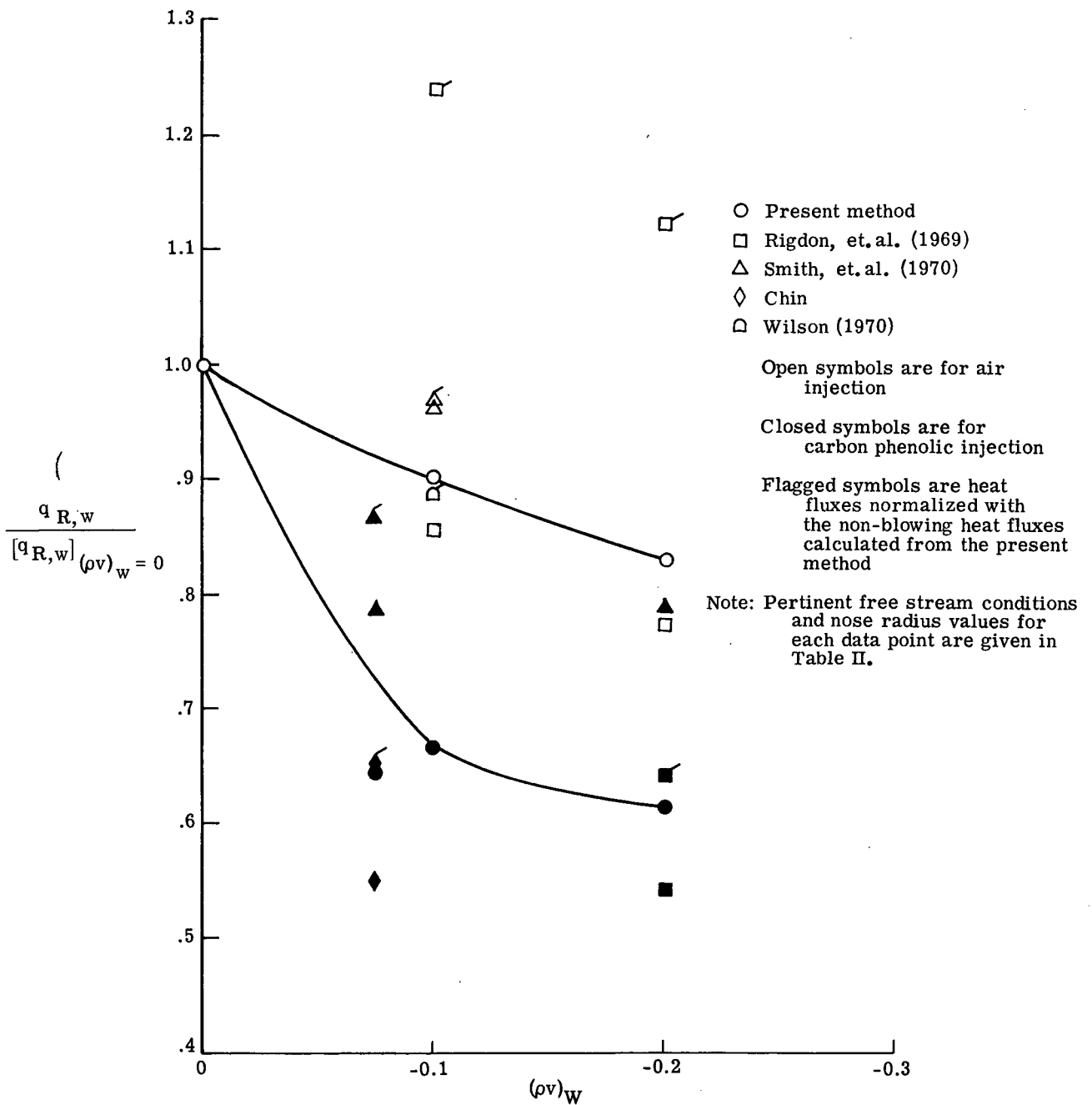


Figure 30. Summary of wall radiative heat flux predictions for air and for ablation product injection

LIST OF REFERENCES

- Anderson, John D., Jr. 1969. An Engineering Survey of Radiating Shock Layers. AIAA J., vol. 7, no. 9: 1665-1675.
- Blottner, F. G. 1969. Viscous Shock Layer at the Stagnation Point With Nonequilibrium Air Chemistry. AIAA J., vol. 7, no. 12: 2281-2288.
- Brown, H. N.; Williams, M. W.; and Cruise, D. R. 1960. The Thermodynamic Properties and Performance Characteristics of Propellant Systems. U.S. Naval Ordnance Test Station, NAVWEPS Report 7043.
- Callis, L. B. 1968. Time Asymptotic Solutions of Blunt-Body Stagnation-Region Flows With Nongray Emission and Absorption of Radiation. AIAA Paper No. 68-663.
- Chin, Jin H. 1968. Radiation Transport for Stagnation Flows Including the Effect of Lines and Ablation Layer. AIAA Paper No. 68-664. Presented at AIAA Fluid and Plasma Dynamics Conference, Los Angeles, California.
- Chou, Y. S.; and Blake, L. H. 1970. Thin Radiating Shock Layer About a Blunt Body. NASA Contractor Report, NASA CR-1547.
- Coleman, W. D.; Hearne, L. F.; Lefferdo, J. M.; and Vojvodich, N. S. 1968. A Study of the Effects of Environmental and Ablator Performance Uncertainties on Heat Shield Requirements for Blunt and Slender Hyperbolic-Entry Vehicles. AIAA Paper No. 68-154.
- Conte, S. D. 1965. Elementary Numerical Analysis. McGraw-Hill Book Co., New York.
- Crandall, Stephen H. 1956. Engineering Analysis - A Survey of Numerical Procedures. McGraw-Hill Book Co., New York.
- Falanga, Ralph A.; and Sullivan, Edward M. 1970. An Inverse-Method Solution for Radiating, Nonadiabatic, Equilibrium Inviscid Flow Over a Blunt Body. NASA Technical Note, NASA TN D-5907.
- Fox, L. 1957. The Numerical Solution of Two Point Boundary Problems in Ordinary Differential Equations. Oxford University Press, Amen House, London.
- Garrett, L. Bernard; Suttles, John T.; and Perkins, John N. 1969. A Modified Method of Integral Relations Solution to the Blunt-Body Equilibrium Air Flow Field, Including Comparisons With Inverse Solutions. NASA Technical Note, NASA TN D-5434.
- Graves, Randolph A., Jr. 1970. Diffusion Model Study in Chemically Reacting Air Couette Flow With Hydrogen Injection. NASA Technical Report, NASA TR R-349.

- Hansen, C. Frederick. 1959. Approximations for the Thermodynamic and Transport Properties of High-Temperature Air. NASA Technical Report, NASA TR R-50.
- Hayes, Wallace D.; and Probstein, Ronald F. 1959. Hypersonic Flow Theory. Academic Press, New York.
- Hildebrand, F. B. 1956. Introduction to Numerical Analysis. McGraw-Hill Book Co., New York.
- Hirschfelder, Joseph O.; Curtis, Charles F.; and Bird, Byron R. 1964. Molecular Theory of Gases and Liquids. John Wiley and Sons, Inc., New York.
- Ho, Hung-Ta; and Probstein, Ronald F. 1961. The Compressible Viscous Layer in Rarefied Hypersonic Flow, pp. 525-552. In L. Talbot (ed.) Rarefied Gas Dynamics, Academic Press, New York.
- Hoshizaki, H.; and Lasher, L. E. 1968. Convective and Radiative Heat Transfer to an Ablating Body. AIAA J., vol. 6, no. 8: 1441-1449.
- Hoshizaki, H.; and Wilson, K. H. 1965. Viscous, Radiating Shock Layer About a Blunt Body. AIAA J., vol. 3, no. 9: 1614-1622.
- Hoshizaki, H.; and Wilson, K. H. 1967. Convective and Radiative Heat Transfer During Superorbital Entry. AIAA J., vol. 5, no. 1: 25-35.
- Howe, John T.; and Viegas, John R. 1963. Solutions of the Ionized Radiating Shock Layer, Including Reabsorption and Foreign Species Effects and Stagnation Region Heat Transfer. NASA Technical Report, NASA TR R-159.
- Inouye, Mamoru. 1965. Blunt Body Solutions for Spheres and Ellipsoids in Equilibrium Gas Mixtures. NASA Technical Note, NASA TN D-2780.
- Kabota, Toshi; and Fernandez, Frank L. 1968. Boundary-Layer Flows With Large Injection and Heat Transfer. AIAA J., vol. 6, no. 1: 22-28.
- Kassoy, D. R. 1970. On Laminar Boundary Layer Blow-Off. SIAM J. Appl. Math., vol. 18, no. 1: 29-40.
- Kennet, H.; and Strack, S. L. 1961. Stagnation Point Radiative Heat Transfer. ARS J., vol. 31: 370-372.
- Khajeh-Nouri, Bejan. 1970. Computational Fluid Mechanics. Presented at NASA Manned Spacecraft Center, Houston, Texas, in October and November 1970.
- Koh, J. C. Y. 1962. Radiation From Nonisothermal Gases to the Stagnation Point of a Hypersonic Blunt Body. ARS J., vol. 32: 1374-1377.

- Kourganoff, V. 1963. Basic Methods in Transfer Problems - Radiative Equilibrium and Neutron Diffusion. Dover Publ., Inc.
- Larkin, B. K. 1967. Heat Flow to a Confined Fluid in Zero Gravity. AIAA Paper No. 67-337. Presented at AIAA Thermophysics Specialist Conference, New Orleans, La.
- Libby, Paul A. 1962. The Homogeneous Boundary Layer at an Axisymmetric Stagnation Point With Large Rates of Injection. J. Aerospace Sci., vol. 29, no. 1: 48-60.
- Libby, Paul A. 1970. Numerical Analysis of Stagnation Point Flows With Massive Blowing. AIAA J., vol. 8, no. 11: 2095-2096.
- Libby, Paul A.; and Sepri, Paavo. 1968. Stagnation Point Flow With Complex Composition. Phys. of Fluids, vol. 11, no. 8: 1621-1627.
- Meyerott, R. E. 1958. Radiation Heat Transfer to Hypersonic Vehicles, pp. 431-447. In M. W. Thring, O. Lutz, J. Fabri, and A. H. Lefebvre (eds.), Third AGARD Combustion and Propulsion Colloquium, Pergamon Press, London, England.
- Nicolet, William E. 1969. User's Manual for the Generalized Radiation Transfer Code (RAD/EQUIL) Aerotherm Report No. UM-69-9, Aerotherm Corp.
- Nicolet, William E. 1970. Advanced Methods for Calculating Radiation Transport in Ablation - Product Contaminated Boundary Layers. NASA Contractor Report, NASA CR-1656.
- Olstad, W. B. 1965. Stagnation-Point Solutions for an Inviscid Radiating Shock Layer, pp. 138-156. In Proceedings of the 1965 Heat Transfer and Fluid Mechanics Institute, Stanford University Press, Stanford, California. See also, Olstad, W. B. 1970. Stagnation-Point Solutions for Inviscid Radiating Shock Layers. NASA Technical Note, NASA TN D-5792.
- Potters, M. L. 1955. A Matrix Method for the Solution of a Linear Second Order Difference Equation in Two Variables. Mathemalich Centrum, Amsterdam, Report MR 19.
- Rigdon, W. S.; Dirling, R. B., Jr.; and Thomas, M. 1968. Radiative and Convective Heating During Atmospheric Entry. NASA Contractor Report, NASA CR-1170.
- Rigdon, W. S.; Dirling, R. B., Jr.; and Thomas, M. 1969. Stagnation Point Heat Transfer During Hypervelocity Atmospheric Entry. NASA Contractor Report, NASA CR-1462.
- Scala, S. M. 1957. The Equations of Motion in a Multicomponent Chemically Reacting Gas. Aerophysics Operations Memo. No. 5, Missile and Ordinance Systems Dept., General Electric Co., Philadelphia, Pa.

- Schlichting, Herman. 1960. Boundary Layer Theory. 4th ed., McGraw-Hill Book Co., New York.
- Smith, A. M. O.; and Clutter, D. W. 1965. Machine Calculations of Compressible Laminar Boundary Layers. AIAA J., vol. 3, no. 4: 639-647.
- Smith, G. Louis. 1968. Radiation Induced Precursor Flow Field Ahead of a Reentry Body. Presented at AIAA Fluid and Plasma Dynamics Conference, Los Angeles, California.
- Smith, G. Louis; Suttles, John T.; Sullivan, Edward M.; and Graves, Randolph A., Jr. 1970. Viscous Radiating Flow Field on an Ablating Body. AIAA Paper No. 70-218. Presented at AIAA Eighth Aerospace Sciences Meeting, New York.
- Suttles, J. T. 1968. A Method of Integral Relations Solution to the Non-Adiabatic Radiation Problem for an Inviscid Blunt Body Flow Field. M.S. Thesis, Aerospace Engineering, Virginia Polytechnic Institute, Blacksburg, Virginia.
- Suttles, John T. 1969. A Method of Integral Relations Solution for Radiating Non-Adiabatic Inviscid Flow Over a Blunt Body. NASA Technical Note, TN D-5480.
- Suttles, J. T. 1971. A Comparison of the Radiative Flux Profiles and Spectral Detail From Three Detailed Non-Grey Radiation Models. In Proceedings of Symposium on Hypervelocity Radiating Flow Fields for Earth and Planetary Entries, Hampton, Virginia.
- Svehla, Roger A. 1962. Estimated Viscosities and Thermal Conductivities of Gases at High Temperatures. NASA Technical Report, TR R-132.
- Thomas, M. 1967. The Spectral Linear Absorption Coefficient of Gases - Computer Program SPECS (H 189). Douglas Report DAC-59135, McDonnell-Douglas Astronautics Co., Western Division.
- Vincenti, Walter G.; and Kruger, Charles H., Jr. 1965. Introduction to Physical Gas Dynamics. John Wiley and Sons, Inc., New York.
- Walberg, Gerald D.; and Sullivan, Edward M. 1970. Ablative Heat Shields for Planetary Entries - A Technology Review. Presented at the ASTM/IES/AIAA Space Simulation Conference, Gaithersburg, Maryland.
- Wick, B. H. 1964. Radiative Heating of Vehicles Entering the Earth's Atmosphere, pp. 607-629. In W. C. Nelson (ed.), The High Temperature Aspects of Hypersonic Flow, Pergamon Press, New York.
- Wilson, K. H. 1967. RATRAP - A Radiation Transport. Code 6-77-67-12, Lockheed Missiles and Space Co.

- Wilson, K. H. 1970. Massive Blowing Effects on Viscous, Radiating, Stagnation-Point Flow. AIAA Paper No. 70-203. Presented at AIAA Eighth Aerospace Sciences Meeting, New York.
- Wilson, K. H.; and Hoshizaki, H. 1969. Effect of Ablation Product Absorption and Line Transitions on Shock Layer Radiative Transport. NASA Contractor Report, NASA CR-1264.

APPENDIX

RADIATION MODEL

The RATRAP radiative transport model developed by Wilson (1967) has been discussed in great detail by Wilson (1967), Suttles (1968), and Wilson and Hoshizaki (1969). A summary of Suttle's discussion on the development of the governing radiative transport equation employed by RATRAP and some details of the radiation model are given in this appendix.

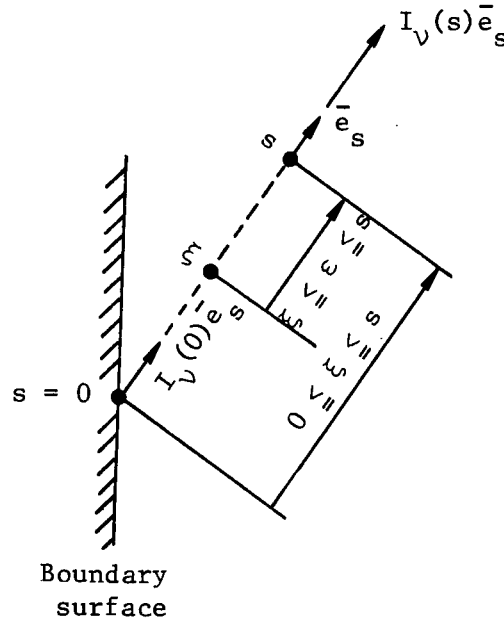
The RATRAP code, which includes the detailed line radiative calculations (sometimes referred to as RATRAP II, since it has been upgraded by its originators, see Wilson and Hoshizaki (1969)), is written for the calculation of the radiative heat flux at any point within a planar (tangent) slab in which the thermodynamic properties vary in only the direction normal to the slab. Local thermodynamic and chemical equilibrium is assumed. A distribution of two thermodynamic variables plus the elemental mass fractions for carbon, nitrogen, oxygen, and hydrogen gaseous mixtures is required for the radiation computations.

For the tangent slab approximation, there is no component of heat flux in the x-direction. Thus the magnitude of the radiative heat flux vector is the radiative heat flux in the y-direction which is expressed as

$$|q_R| = q_{R,y} = \int_0^\infty \int_0^{4\pi} I_\nu (\bar{e}_s \cdot \bar{e}_y) d\Omega d\nu \quad (A-1)$$

where I_ν is the specific intensity, \bar{e}_s is the unit vector in the arbitrary direction in which I_ν is evaluated as shown in Sketch A,

and Ω and ν are the solid angle and the frequency of radiation, respectively. (Note that the quantities are dimensional; however, the primed symbol used to denote dimensional quantities in the main body of this study is dropped in this appendix for simplicity.)



Sketch A

The differential equation governing the radiative transfer (see, e.g., Vincenti and Kruger) which is given by

$$\frac{dI_\nu}{ds} \equiv \alpha_\nu(B_\nu - I_\nu) \quad (\text{A-2})$$

has the solution

$$I_\nu(s) = \int_0^s \alpha_\nu(\xi) B_\nu(\xi) e^{-\int_\xi^s \alpha_\nu(\epsilon) d\epsilon} d\xi + I_\nu(0) e^{-\int_0^s \alpha_\nu(\xi) d\xi} \quad (\text{A-3})$$

where α_ν is the modified linear absorption coefficient, B_ν is the Planck function given by

$$B_\nu \equiv 2 \times 10^{-7} \frac{h\nu^3}{c^2} \left[e^{(h\nu/kT)} - 1 \right]^{-1} \quad (\text{A-4})$$

$I_\nu(0)$ is the radiation intensity coming from the wall and ϵ and ξ are dummy variables for the integrals such that $\xi \leq \epsilon \leq s$ and $0 \leq \xi \leq s$, as shown in Sketch A.

Equations (A-1) and (A-3) can be combined (see Suttles (1968)) to yield

$$q_{R,y} = 2\pi \int_0^\infty \left[\int_0^y \alpha_\nu B_\nu E_2 \left(\int_\xi^y \alpha_\nu d\epsilon \right) d\xi - \int_y^s \alpha_\nu B_\nu E_2 \left(\int_y^\xi \alpha_\nu d\epsilon \right) d\xi \right] d\nu \quad (\text{A-5})$$

when the heat fluxes into the slab at the boundaries are neglected. The quantity $E_2 \left(\int_y^\xi \alpha_\nu d\epsilon \right)$ is the exponential integral described by Kourganoff and is given by

$$E_2(\xi) = \int_0^1 e^{-\xi/\mu} d\xi \quad (\text{A-6})$$

In order to evaluate equation (A-5), it is necessary to calculate the spectral linear absorption coefficients α_ν which are functions of the thermodynamic properties (p and T) and the number densities of the chemical species. Twenty chemical species are considered in the thermodynamic calculations. They are C_2 , N_2 , O_2 , H_2 , C , N , O , H , CO , CN , C_2H , C_3H , C_4H , HCN , C_2H_2 , C^- , C^+ , N^+ , O^+ , and H^+ .

The total spectral absorption coefficient is separated into continuum and line contributions in the RATRAP calculations. The continuum spectral absorption processes considered are the free-free

transitions (acceleration of free electrons in the vicinity of atoms and ions) of C, C⁺, N, N⁺, O, O⁺ and the free-bound and bound-free transitions (deionization and ionization, respectively, of the H atoms and positively ionized particles. Molecular bands are also included in the continuum calculations. These molecule contributions and frequency intervals from Wilson and Hoshizaki (1969) are tabulated below.

Table A. Molecular band systems used in RATRAP

Molecule contribution	Frequency range for significant absorption photon energy, eV
H ₂ Werner	$11 \leq h\nu \leq 15.494$
Photoionization	$15.494 \leq h\nu \leq 25$
C ₂ Swan	$1.8 \leq h\nu \leq 6.0$
Fox Herzberg	$1.8 \leq h\nu \leq 5.35$
Mulliken	$5.35 \leq h\nu \leq 6.0$
Freymark	$1.8 \leq h\nu \leq 6.0$
CN Violet	$2.0 \leq h\nu \leq 6.0$
CO 4th Positive	$7 \leq h\nu \leq 10$
N ₂ Birge-Hopfield	$11 \leq h\nu \leq 14.2$
O ₂ Schuman-Runge	$7 \leq h\nu \leq 9.2$

For the calculation of the continuum contribution to the heat flux, the absorption coefficients for the individual species are weighted with their respective number densities and approximated by curve fits over frequency ranges. The heat flux equation (A-5) is subsequently evaluated by numerically integrating over y and over frequency, using 11 values of y and 31 values of frequency.

The atomic line radiation component arises as a result of the many bound electronic transitions which occur in the atomic nitrogen and oxygen species (line radiation from carbon and hydrogen species are not included in RATRAP). This component is obtained by first grouping certain line contributions within various frequency intervals. The net line radiation is then calculated by summing the contributions from these line groups. Eighteen line groups, with a total of 65 lines, are used in RATRAP.

The total radiative heat flux at each point is obtained by adding the continuum and the line radiation contributions.